NREL/TP-411-7188 • UC Category: 1280 • DE95000243

Continuous Roll-to-Roll Amorphous-Silicon Photovoltaic Manufacturing Technology

Annual Subcontract Report
8 April 1993 – 7 April 1994

M. Izu
Energy Conversion Devices, Inc.
Troy, Michigan

NREL technical monitor: R. Mitchell

National Renewable Energy Laboratory
1617 Cole Boulevard
Golden, Colorado 80401-3393
A national laboratory of the U.S. Department of Energy
Managed by Midwest Research Institute
for the U.S. Department of Energy
under contract No. DE-AC36-83CH10093

Prepared under Subcontract No. ZM-2-11040-7

November 1994

NOTICE

Available to DOE and DOE contractors from:
Office of Scientific and Technical Information (OSTI)
P.O. Box 62
Oak Ridge, TN 37831
Prices available by calling (615) 576-8401

Available to the public from:
National Technical Information Service (NTIS)
U.S. Department of Commerce
5285 Port Royal Road
Springfield, VA 22161
(703) 487-4650

Printed on paper containing at least 50% wastepaper and 10% postconsumer waste

Table of Contents

Table of Contents

Preface

This Annual Technical Progress Report covers the work performed by Energy Conversion Devices, Inc. (ECD) for the period of April 8, 1993, to April 7, 1994, under DOE/NREL Subcontract number ZM-2-11040-7 entitled "Continuous Roll-to-Roll a-Si Photovoltaic Manufacturing Technology." The total period covered under this subcontract is April 8, 1992 to July 7, 1995. The following personnel participated in the research program:

T. Barnard
H. Bianchi
R. Ceragioli
J. Chema
B. Clark
R. Crucet
X. Deng
J. Evans
C. Harrison
M. Izu
R. Kopf
A. Krisko
A. Kumar
T. Laarman
A. Myatt
K. Narasimhan
S.R. Ovshinsky
H.C. Ovshinsky
R. Souleyrette
S. Sullivan
D. Tsu
K. Whelan
R. Woz
R. Young

We would like to thank Drs. H. Fritzsche, S. Guha, and J. Yang for helpful discussions.

LIST OF FIGURES

LIST OF TABLES

Executive Technical Progress Summary

Objectives and Goals

The overall objective of this three-year program is to advance ECD's roll-to-roll, triple-junction photovoltaic manufacturing technologies, to reduce the module production costs, to increase the stabilized module performance, and to expand the commercial capacity utilizing ECD technology.

The specific three-year goal is to develop advanced large-scale manufacturing technology incorporating ECD's earlier research advances with the capability of producing modules with stable 10.2% efficiency at a cost of approximately $1.00 per peak watt.

Major efforts in the second year, Phase II, are the optimization of the high-performance back-reflector system, Task 6; the optimization of a-SiGe narrow band-gap solar cells, Task 7; and the optimization of the stable efficiency of the module, Task 8. Our Phase II goal is to achieve a stable 9.5% efficient 1 ft x 4 ft. module. Efforts also include work on serpentine web continuous roll-to-roll deposition technology, Task 9; and on the investigation of material cost reduction, Task 10.

Progress Summary

In Phase I, which ended on March 31, 1993, we performed manufacturing technology development work utilizing our advanced continuous roll-to-roll triple-junction a-Si alloy solar cell production line, engineered and manufactured by ECD. The production line consists of:

1. A continuous roll-to-roll substrate washing machine.
2. A continuous roll-to-roll back-reflector machine.
3. A continuous roll-to-roll amorphous silicon alloy deposition machine.
4. A continuous roll-to-roll transparent conductor deposition machine.

The production line produces triple-junction two band-gap a-Si alloy solar cells consisting of an a-Si/a-Si/a-SiGe structure on a 5 mil. thick, 14 in. wide, 2500 ft. stainless steel roll at a speed of 1 ft./min. This production line represents the world's first commercial production of high-efficiency a-Si alloy solar cells utilizing a multi-junction spectrum-splitting cell design and high performance back-reflector.

In Phase I we achieved the following:

- Successfully incorporated a high-performance Ag/metal oxide back-reflector system into our continuous roll-to-roll commercial production operation
- Incorporated high quality profiled a-SiGe narrow band-gap solar cells into a commercial continuous roll-to-roll manufacturing process
- Demonstrated that the continuous roll-to-roll production of high-efficiency triple-junction two band-gap solar cells is consistent and uniform throughout a 2500 ft. run with high yield; the average initial subcell efficiency and yield were 10.21% and 99.7%, respectively.
- Achieved 11.1% initial subcell efficiency of triple-junction two band-gap a-Si alloy solar cells in continuous roll-to-roll production.

- Produced the world's first 4 ft^2 PV modules utilizing triple-cell spectrum-splitting solar cells manufactured in a commercial, continuous roll-to-roll production line, these 4 ft^2 modules had 9.5% initial efficiency and 8% stable module efficiency

- As the result of process optimization to reduce the layer thickness and to improve gas utilization, 77% material cost reduction for germane and 58% reduction for disilane have been achieved. Additionally, we developed a new low-cost module saving approximately 30% in assembly material costs.

During this program period, we have designed and constructed, at ECD's expense, a new improved continuous roll-to-roll multi-purpose deposition machine that has 200 kW annual capacity and incorporates improvements necessary to further advance the performance of PV modules. Figure 1 is a picture of this machine. Figure 2 is the schematic drawing of this machine.

As seen in Figure 2, the machine has a left-hand drive assembly, an n-deposition chamber, a serpentine deposition chamber, an i-deposition chamber, a p-deposition chamber, a sputtering chamber, and a right-hand drive assembly. Steering and web tensions are controlled in both forward and reverse directions of web travel. This provides bi-directional deposition of material.

The machine is capable of producing n-i-p solar cells in a single pass and triple-junction cells in three passes. The i-chamber has a specially designed proprietary gas distribution manifold and multiple cathodes, and is capable of continuously depositing profiled a-SiGe alloy material in roll-to-roll operation.

This design combines, in one machine, sputtering for the back-reflector and top conductor with RF plasma CVD for the a-Si solar cell.

We will utilize this machine to further improve the performance of PV modules on a 14-inch wide web of stainless steel produced in a continuous roll-to-roll process.

In Phase II, which ended April 7, 1994, our main efforts were:

1. Improving the performance of the back-reflector system.

2. The design, construction, at ECD's expense, and initial optimization of a new improved continuous roll-to-roll multi-purpose deposition machine which incorporated the improvements necessary to further advance the performance of PV modules

3. The design, construction, at ECD's expense, and initial optimization of a serpentine web continuous roll-to-roll deposition chamber.

4. Cost reduction program.

Major Accomplishments in Phase II

1. We have designed, constructed, at ECD's expense, and completed initial optimization of a 200 kW multi-purpose continuous roll-to-roll a-Si alloy solar cell deposition machine having upgraded machine and construction specifications. Initial results confirm that solar cells produced in this machine have a higher fill factor that results from the improved quality of intrinsic layers.

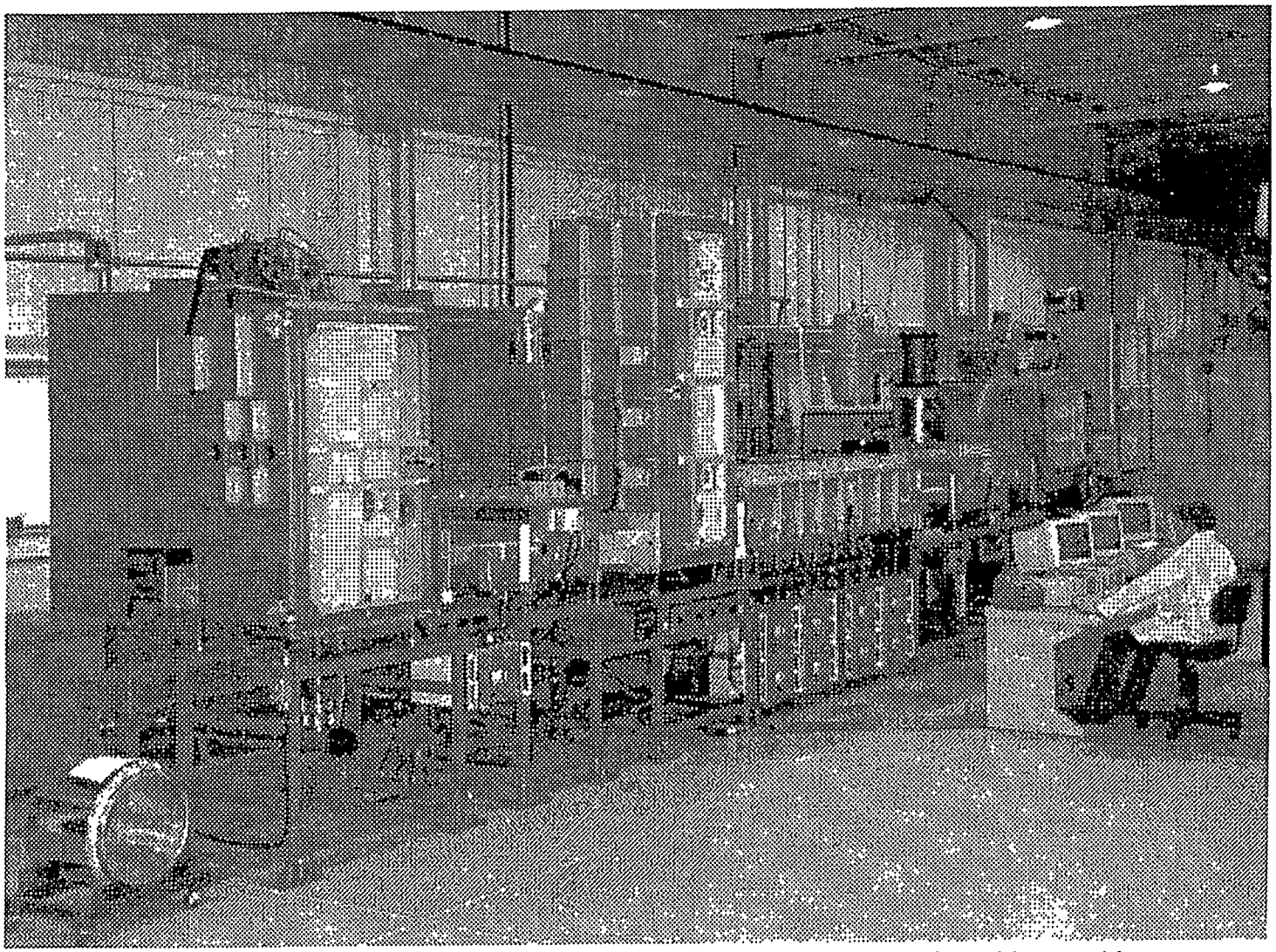

Figure 1: ECD's multipurpose continuous roll-to-roll a-Si alloy solar cell deposition machine.

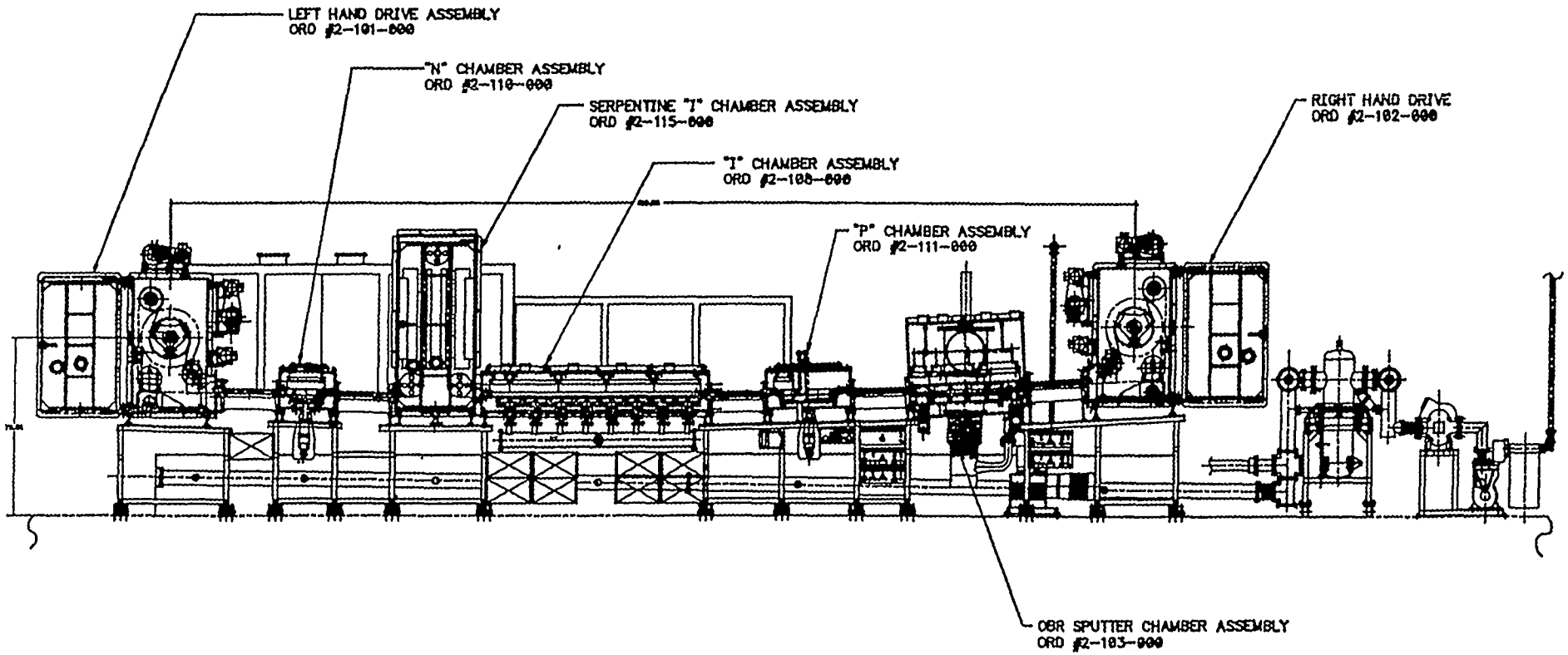

Figure 2: Schematic drawing of ECD's multipurpose continuous roll-to-roll solar cell deposition machine.

2. We have designed and constructed, at ECD's expense, a serpentine deposition chamber which will be used to demonstrate a compact, low cost deposition machine design with improved throughput and gas utilization factor.

3. We have demonstrated $\geq$ 8.3% initial small-area efficiency a-Si alloy devices with an intrinsic a-Si layer deposited using serpentine technology in the initial start-up experiments.

4. We have developed a new back-reflector evaluation technique using Photothermal Deflection Spectroscopy (PDS) to effectively analyze the optical losses of textured back-reflector.

5. We have developed an improved textured Ag/ZnO back-reflector system demonstrating 26% gain in J_{sc} over previous textured Al back-reflector systems.

6. We have demonstrated the long-term stability of ECD's 1 ft. x 4 ft. production module. The stable module efficiency after 2380 hours of sun light soaking at approximately 50°C is 7.9%. Light soaking testing of ECD modules performed at NREL under one sun at 50°C showed 15% degradation after 600 hours. ECD's 4 ft^2 modules have passed heat and humidity/freeze cycles of NREL recommended module reliability testing procedure.

7. We have developed a new grid/bus-bar design utilizing thin wire grids to improve the efficiency by approximately 3% ~ 4% and reduce the grid/bus-bar cost by approximately 50%.

8. We have achieved a cumulative material cost reduction of 56%.

Introduction

During the past fifteen years, ECD has made important progress in the development of materials, device designs, and manufacturing processes required for the continued advancement of practical photovoltaic technology[1-19]. Among these accomplishments, ECD has pioneered and continues further development of two key proprietary technologies, with significant potential for achieving the cost goals necessary for widespread growth of the photovoltaic market: (1) a low cost, roll-to-roll continuous substrate thin-film solar cell manufacturing process; (2) a high efficiency, monolithic, multiple-junction, spectrum-splitting thin-film amorphous silicon alloy device structure.

Commercial production of multiple-junction a-Si alloy modules has been underway at ECD and its joint venture company for a number of years using ECD's proprietary roll-to-roll process and numerous advantages of this technology have been demonstrated. These include relatively low semiconductor material cost, relatively low process cost, a lightweight, rugged and flexible substrate that results in lowered installed costs of PV systems, and environmentally safe materials. Nevertheless, the manufacturing cost per watt of PV modules from our current plant remains high.

Under this Phase 2A Photovoltaic Manufacturing Technology (PVMaT) Program, ECD will advance its continuous roll-to-roll manufacturing technology and develop the capability of producing triple-junction multiple band-gap a-Si alloy photovoltaic modules with stable 10.2% efficiency at a cost of approximately $1.00 per watt in a high volume production plant. Major efforts will be focused on improving the stable efficiency of modules, increasing production throughput and reducing material and labor cost.

In order to achieve high stable efficiency and low manufacturing cost, ECD will develop and demonstrate large-volume manufacturing technology that can incorporate earlier ECD research advances in device efficiency through the use of multi-junction spectrum-splitting and high performance back-reflector cell design. In this program period, Task 6: Optimization of the back-reflector system, Task 7: Optimization of the Si-Ge narrow band-gap solar cells, Task 8: Optimization of the stable efficiency of photovoltaic modules, Task 9: Demonstration of serpentine web continuous roll-to-roll deposition technology, and Task 10: Material cost reductions were directed towards achieving this goal.

ECD's Continuous Roll-to-Roll Amorphous Silicon Photovoltaic Manufacturing Technology

Features and Advantages of ECD's PV Manufacturing

Spectrum Splitting, Triple-Junction Cell Design

The key feature of our continuous roll-to-roll production is the use of triple-junction two band-gap solar cells with high quality, band-gap profiled a-Si alloy as the bottom intrinsic layer. The cell structure is shown in Figure 3.

ECD has demonstrated 13.7% initial small-area photo conversion efficiency in a-Si alloy solar cell devices with a-Si/a-Si/a-SiGe triple-junction design. The manufacturing line has been designed and engineered to produce solar cells incorporating this most advanced cell design for obtaining high stable efficiency modules.

Low cost, large scale continuous roll-to-roll operation

In the roll-to-roll deposition of a-Si alloy solar cells, nine layers of a-Si alloys are produced in a single pass onto a 2500 ft. substrate. This stable steady-state process has proven reliable, and provides uniform cells. The operating cost, which includes maintenance and labor, is low.

Flexible thin stainless steel substrate

The substrate is a 5 mil. thick, 14 in. wide, 2500 ft. long stainless steel roll. It offers many advantages compared to glass substrates. Stainless steel does not shatter during operation and handling. This thin stainless steel substrate can be heated and cooled quickly during deposition, i.e., no waiting time is needed for temperature stabilization. During deposition, the substrate transport mechanism is simple and reliable, and component wear is low. This keeps maintenance costs low. Also, the substrate is lightweight and flexible.

Lightweight polymer encapsulated PV module

EVA/Tefzel is used for module encapsulation. Modules thus made are lightweight and shatter-proof. With some designs, the modules can be made flexible.

ECD's Continuous Roll-to-Roll Manufacturing Line

In the 2 MW PV manufacturing line, we deposit triple-junction two band-gap a-Si alloy solar cells in a continuous roll-to-roll process on a 5 mil. thick, 14 in. wide and 2500 ft. long web of stainless steel at a speed of 1 ft./min.

	Grid	Screen Print
	TCO	Reactive Evaporation
p3	microcrystalline Si alloy	PECVD
i3	a-Si alloy	PECVD
n3	a-Si alloy	PECVD
p2	microcrystalline Si alloy	PECVD
i2	a-Si alloy	PECVD
n2	a-Si alloy	PECVD
p1	microcrystalline Si alloy	PECVD
i1	a-SiGe alloy	PECVD
n1	a-Si alloy	PECVD
	Textured Back-reflector Ag/ZnO	Sputtering
	Stainless Steel Substrate	

Figure 3: Structure of a triple-junction spectrum-splitting solar cell produced in ECD's continuous roll-to-roll manufacturing process.

The front end of the manufacturing line consists of four continuous roll-to-roll machines:

Substrate Washing Machine

Prior to the film deposition, the stainless steel is loaded into a roll-to-roll substrate washing machine that transports the stainless steel web through a detergent cleaning station, multiple deionized water rinsing baths, and an infrared oven drying stage, to produce a clean, dry, particle-free substrate suitable for amorphous silicon deposition.

Back-Reflector Machine

After washing and drying, the roll is loaded into a roll-to-roll back-reflector machine that deposits a reflective metal layer and a metal oxide layer on the cleaned, stainless steel web. Both the metal and the metal oxide layer are vacuum deposited by DC magnetron sputtering onto the heated substrate.

The metal adheres to the stainless steel and texturizes the surface to provide a diffuse, reflective layer with high reflectivity. This enhances absorption of the infrared portion of the solar spectrum by providing an increased optical path length for reflected light in the thin film solar cell structure and by increasing reflectivity over that of the stainless steel. The metal and oxide layers provide ohmic contact to the solar cell as well as improved infrared response.

Amorphous Silicon Alloy Deposition Machine

After the back-reflector deposition, the roll is loaded into the amorphous silicon alloy roll-to-roll deposition machine that produces, in a single pass, sequentially deposited thin films of doped and undoped amorphous silicon alloy material. Mixtures of feedstock gases are decomposed at a pressure of approximately 1 Torr in a series of RF CVD plasma chambers to continuously deposit layers of amorphous silicon alloy material onto the coated stainless steel substrate heated to approximately 250°C to 300°C. The multi-section amorphous silicon alloy deposition machine consists of a pay-off chamber section, nine process chamber sections for the triple device structure and a take-up section. The process gas mixtures in each section are dynamically isolated from adjacent sections by proprietary "gas gates." The "gas gates" utilize laminar gas flow through constant geometrical cross section conduits in a direction opposite to the diffusion gradient of the dopant gas concentrations. In this way, migration of dopants between chambers is essentially eliminated and gas mixtures in adjacent chambers are effectively isolated even though no actual physical impediment is present. Substrate transport is accomplished with controlled tension and magnetic rollers for accurate positioning of the substrate in the various process chambers. The web is steered in the take-up chamber to insure that the substrate is properly wound. Substrate passage through the process chambers is such that deposition takes place on the underside, which minimizes film defects due to particulate accumulation. The production equipment has nine RF-plasma deposition chambers to produce a-Si/a-Si/a-SiGe triple-junction two band-gap solar cells.

Transparent Conductor Deposition Machine

The solar cell roll is then transferred to the transparent conducting oxide (TCO) roll-to-roll deposition machine that vacuum-deposits a transparent, electrically conductive layer on top of the solar cell structure. Metal is reactively evaporated in an oxygen atmosphere. The substrate is heated to approximately 200°C during this deposition process. The TCO layer has two functions. First, it provides an electrical top contact between the current generating photovoltaic layers and the current collection grid. Second, its thickness is selected so that it acts as an anti-reflective coating to pass more incident light.

These four continuous roll-to-roll machines are highly automated. Sophisticated records are obtained during the deposition.

The PV module assembly process consists of the following procedures:

1. Slabbing
2. Quality Assurance and Quality Control (QA/QC)
3. Scribing
4. Short Passivation
5. Screen Print Grid Pattern
6. Final Assembly

ECD's New Continuous Roll-to-Roll Multi-purpose a-Si Deposition Machine

We have designed and constructed, at ECD's expense, a new, improved 200 kW continuous roll-to-roll multi-purpose deposition machine that incorporates improvements necessary to further advance the performance of PV modules. A picture of the machine is shown in Figure 1. The schematic drawing of the machine is shown in Figure 2.

As seen in Figure 2, the machine has a left-hand drive assembly, an n-deposition chamber, an i-deposition chamber, a p-deposition chamber, a sputtering chamber, and a right-hand drive assembly. Steering and web tensions are controlled in both forward and reverse directions of web travel. This provides bi-directional deposition of material.

The machine is capable of producing n-i-p solar cells in a single pass and triple-junction cells in three passes. The i chamber has a specially designed proprietary gas distribution manifold and multiple cathodes, and is capable of continuously depositing profiled a-SiGe alloy material in roll-to-roll operation.

This design combines, in one machine, sputtering for the back-reflector and top conductor with RF plasma CVD for the a-Si solar cell.

We will utilize this machine to further improve the performance of PV modules produced in a continuous roll-to-roll process.

Continuous Roll-to-Roll Serpentine Deposition Technology

To further advance ECD's PV manufacturing technology toward achieving higher production throughput, higher stable module efficiency and lower manufacturing cost, we have designed and constructed a deposition chamber using continuous roll-to-roll serpentine web configuration. In this serpentine deposition chamber, the web travels vertically while deposition takes place on both sides of a vertically mounted, perforated RF power cathode. As a consequence, we can achieve maximized throughput for a high volume production plant, reduced machine cost, improved gas utilization, reduced power consumption, and improved material stability.

Task 6: Optimization of the Back-Reflector System

Introduction

In ECD's continuous roll-to-roll PV manufacturing line we use continuous roll-to-roll DC Magnetron sputtering to deposit metal/metal oxide back-reflectors. During the first year of this program we, for the first time, successfully incorporated Ag/ZnO back-reflectors into continuous roll-to-roll production. We have achieved 16.4 mA/cm^2 - 16.7 mA/cm^2 short-circuit current for approximately 4000 Å a-Si n-i-p solar cell on this back-reflector and 99.7% subcell yield for a 600 m long production run with this Ag/ZnO back-reflector.

Although the Ag/ZnO back-reflector from ECD's production machine has demonstrated high current in solar cells, there is scope for further improvement. We identified some optical loss in the current back-reflector and that the degree of texture, which is necessary for light trapping, can be further optimized. There are still interference fringes in the QE curve of the cell, which indicates the degree of texture is not optimum.

To further improve solar cell current, we developed evaluation techniques to accurately measure the performance of back-reflector systems and we conducted a research program to develop high performance back-reflectors using R&D batch deposition machines.

Development of Evaluation Techniques

In order to evaluate the performance of the back-reflector, we developed a PDS technique to measure the optical losses of reflective layers on stainless steel substrate. We also use angular dependence of reflection, and SEM to study the texture. The QE response for standard solar cells deposited on the back-reflector is used as the final criterion for back-reflector performance evaluation.

The PDS Technique for Evaluating Optical Losses of Back-Reflectors

We modified Photothermal Deflection Spectroscopy (PDS) for use as an important measurement technique for back-reflector performance evaluation[20]. PDS has demonstrated advantages in the measurement of optical loss, especially for highly reflective and textured surfaces, because, unlike conventional reflectance measurements, PDS measures the fraction of the light that is converted to heat.

In the PDS system, monochromatic light is focused on the sample which is immersed in CCl_4 in a cuvette cell. The portion of light that is absorbed by the sample and substrate is converted to heat, the remainder of the light, either transmitted through or reflected back, does not contribute to heat generation. The absorbed light heats up the local region of CCl_4 around the illuminated spot and forms a semisphere of CCl_4 with different local temperatures and hence different refractive indexes, so it acts like a lens. A HeNe probe beam passes through the CCl_4 in front of the sample surface and is deviated by the CCl_4 lens. A position sensor detects the shift of the HeNe light spot. The deviation of the light spot on the position sensor is proportional to the amount of heat absorbed by the sample surface. We measure the light intensity of different wavelengths using a thermopile at the position of the sample. Absorption as low as 0.01% can be easily measured.

In current back-reflector research, we use PDS to detect the low absorption signal of highly reflective surfaces such as Ag. The majority of light is specularly reflected, or in the case of textured surfaces, scattered, and does not contribute to the signal that PDS measures. Therefore, with appropriate calibration, PDS is a powerful tool in measuring the light absorption loss in highly reflective and highly textured surfaces.

The output signal we measure includes magnitude and phase. With every new sample, we adjust the distance between the HeNe laser beam and the sample front surface to maximize the magnitude of the signal. When the PDS signal is maximized, the phase of the signal is always the same for the same type of substrate. The PDS phase is used as an independent check for the signal maximization.

The PDS signal for different wavelengths is calibrated with a Perkin-Elmer 330 Spectrophotometer using plain specular stainless steel. Table 1 lists the PDS signal and reflectance measured with a Perkin-Elmer Spectrophotometer, as well as the method we use to obtain the calibration factor (C), which is the ratio of PDS absorption (A_{pds}) to PDS signal (V_{pds}). When we measure other samples with PDS, we obtain the absorption loss by multiplying V_{pds} with the calibration factor A_{pds}/V_{pds}, which should be the same for all back-reflector samples on stainless steel substrate. Table 2 lists the absorption measurement of specular Ag sample (BR13) and the reference sample (OBR83) using PDS and using the calibration factor we obtained above. We have identified that the optical loss at 827 nm in the existing back-reflector (OBR83) is 7.0%.

The PDS signal also depends on the substrate. The V_{pds} of the sample on glass is roughly a factor of 2.0 higher than the V_{pds} for the same sample on stainless steel.

We routinely check the system reproducibility of the PDS setup by measuring the reference sample OBR83. The measurement on this sample has always been reproducible. The reproducibility of the PDS measurement is within a few percent. The absolute PDS signal calibration depends, to some extent, on the surface conditions of the sample to be measured. We are in the process of gaining further understanding and obtaining more reliable and accurate calibration.

PDS can be used to measure the light loss of different solar cell layers without complete cell structure. In Table 3, we list the PDS measurement of SS, SS/Ag, SS/Ag/ZnO, SS/Ag/ZnO/n^+. The PDS spectra of SS/Ag/ZnO and SS/Ag/ZnO/n+ have interference fringes.

Angular Dependence of Reflectance

In order to quantitatively measure surface texture, we built a setup for measuring the angular dependence of reflectance. In this setup, samples are held by a fixed magnetic base. A HeNe laser beam illuminates the reflection surface at an incident angle of around 6°. A Si detector of 1 cm^2 active area is used to measure the light intensity at 22 cm from the light spot, and at an angle θ from the direction in which the beam emanates when the surface is specular. The Si detector output is measured by an electrometer. As a routine check, we measure the light intensity at three positions corresponding to $\theta = 0$, 30° and 60°. The I (0°) intensity after being normalized to the incident light intensity, gives the specular reflection coefficient of the sample. The I (30) and I (60) measure the amount of scattered light. I (60) / I (30) reveals the dispersion of the distribution. Table 4 lists the intensity at different reflected angles for two back-reflectors, a specular back-reflector (BR39) and a textured back-reflector (BR61). Figure 4 is reflectance of a textured sample BR48 as a function of θ. The relation is close to $I(\theta) \propto \cos\theta$.

Table 1: Calibration of PDS signal Perkin-Elmer 330 spectrophotometer.

$h\nu$(eV)	Photon energy	2.1	1.9	1.7	1.5	1.3	1.1
λ(nm)	Wavelength	590	653	729	827	954	1127
V_{pds}(mV)	Lock-in output	1.32	2.8	4.04	4.69	8.3	9.3
V_{tp}(mV)	Thermopile output	0.0271	0.0578	0.0832	0.101	0.192	0.266
V_{pds}/V_{tp}	Relative absorption	48.7	48.4	48.6	46.4	43.2	35.0
R_{pe}	Reflection from Perkin-Elmer	64.5%	65.5%	67.0%	69%	-----	-----
A_{pe}	$=1-R_{pe}$	35.5%	34.5%	33%	31%		
F	$A_{pe}/(V_{pds}/V_{tp})$	7.29×10^{-3}	7.13×10^{-3}	6.79×10^{-3}	6.68×10^{-3}		
F_{av}	average of F			7.0×10^{-3}			
c	calibration factor $A_{pds}/V_{pds}=F_{av}/V_{tp}$	0.259	0.121	0.084	0.069	0.0365	0.0263

Table 2: PDS measurement of optical loss of specular Ag (BR13) and reference back-reflector (OBR83).

Sample	Type		Wavelength (nm)					
			590	653	729	827	954	1127
BR13	Specular Ag on SS	V_{pds}(mV)	0.09	0.18	0.23	0.23	0.39	0.41
		Phase (degree)	55	61	61	59	61	59
		Reflection loss	2.3%	2.2%	1.9%	1.6%	1.4%	1.1%
OBR83	Textured Ag/ZnO	V_{pds}(mV)	0.57	1.00	1.03	1.02	1.57	1.5
	on SS	Phase (degree)	55	58	58	56	56	54
		Reflection loss	14.8%	12.1%	8.7%	7.0%	5.7%	3.9%

Table 3: Reflection loss of various layers measured by PDS.

Sample		Wavelength (nm)					
		590	653	727	827	954	1127
SS	V_{pds} Reflection loss	1.32 34.1%	2.8 33.9%	4.04 33.9%	4.67 32.3%	8.3 30.3%	9.3 24.4%
SS/Ag(specular) BR13	V_{pds} Reflection loss	0.09 2.3%	0.18 2.2%	0.23 1.9%	0.23 1.6%	0.39 1.4%	0.41 1.1%
SS/Ag(textured) BR66	V_{pds} Reflection loss	0.33 8.5%	0.607 7.3%	0.76 6.4%	0.83 5.7%	1.63 5.9%	2.00 5.3%
SS/Ag(specular)/ZnO SS/BR23/ZnO38	V_{pds} Reflection loss	0.17 8.5%	0.40 4.8%	0.517 4.3%	0.371 2.6%	0.67 2.4%	0.91 2.4%
SS/Ag(specular)/ZnO/thin n^+ SS/BR42/ZnO54/LL563	V_{pds} Reflection loss	1.25 32%	1.82 22%	1.84 15.4%	1.92 13.2%	3.22 11.8%	3.05 8.0%

Table 4: Intensity of specular and scattered light at different reflection angles for a specular back-reflector (BR39) and a textured back-reflector (BR61). Light intensity of the incident HeNe light is 6.62mW, which gives 2.5 mA in the detector readout.

Sample BR39, specular Ag

Detector output:	
Incident beam:	2.5 mA
Reflected beam:	2.3 mA at $\theta = 0^o$
	5.2×10^{-5} mA at $\theta = 30^o$
	2.7×10^{-5} mA at $\theta = 60^o$
Percentage of specular reflected light:	92%
Percentage of scattered reflected light:	3.5%*

Sample BR61, textured Ag

Detector output:	
Incident beam:	2.5 mA
Reflected beam:	0.538 mA at $\theta = 0^o$
	1.05×10^{-3} mA at $\theta = 30^o$
	2.7×10^{-5} mA at $\theta = 60^o$
Percentage of specular reflected light:	22%
Percentage of scattered reflected light:	74%*

*Calulated from equation (1) assuming $I(\theta) \propto \cos\theta$ relation.

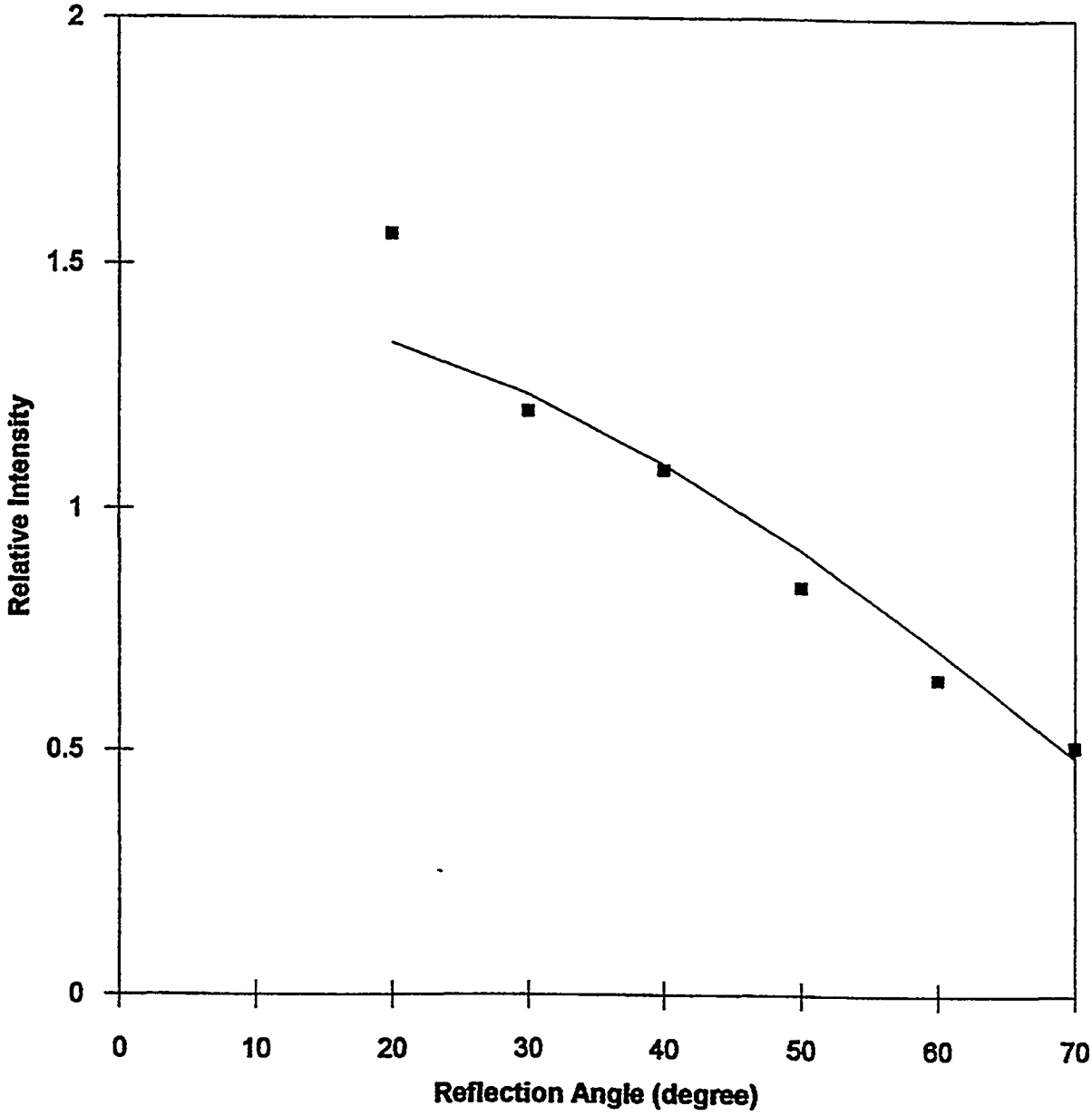

Figure 4: Intensity of reflected light at different angle θ for a textured sample (BR48). The line is the curve with ∝ cos θ relation.

We also calculated the integrated intensity based on I (30) and I (60) if we assume the lambertian distribution (cos) relation.

$$I(\theta) \propto \cos\theta$$

$$I(\theta) = \frac{1}{2}\left(\frac{I(30)}{\cos 30} + \frac{I(60)}{\cos 60}\right)\cos\theta$$

$$= \left(\frac{I(30)}{\sqrt{3}} + I(60)\right)\cos\theta$$

$$I_{scatter} = \int_0^{90} I(\theta) \bullet 2\pi r \bullet \sin\theta \bullet r d\theta$$

$$= \pi r^2\left(\frac{I(30)}{\sqrt{3}} + I(60)\right)$$

where r = 22 cm

So the percentage of scattered light is

$$\frac{I_{scattered}}{I_{incident}} = \frac{\pi r^2}{I_{incident} \bullet Ad}\left(\frac{I(30)}{\sqrt{3}} + I(60)\right)$$

where $Ad = 1(cm^2)$

Together with PDS, the angular dependence of reflectance can provide important information about the reflectance and texture of a reflection surface.

Scanning Electron Microscopy

SEM is used to study the size and shape of the textured grains. An incident angle of 60 degrees is used to reveal the depth of the texture. Magnification of 40,000 is used to study the morphology of the surface in the scale of 0.3 μm - 0.4 μm, which is the wavelength of red light in ZnO.

Absolute Quantum Efficiency of Solar Cell

a-Si n-i-p solar cells are made on these back-reflectors in two different systems: 1) multiple chamber load-lock PECVD system (LL) and 2) multiple cup load-lock PECVD system (ORD1). The cell structure is: ss/back-reflector/n-i-p/ITO. The current density (J_{ph}) integrated from absolute quantum efficiency of the solar cell, is used as the final and the most important criteria for determining back-reflector performance. Special attention was paid to the red response between 600 nm to 800 nm. In each solar cell run, a reference back-reflector sample OBR83 was used as the control. The back-reflector under study and OBR83 were simultaneously put through the process including ITO evaporation and QE measurement to minimize possible run-to-run variations. The variation in current of reference OBR83 from run to run was typically 0.1 mA/cm^2.

Development of New Back-Reflector

After identifying the optical losses and the lack of ideal texture in our existing back-reflector, we directed our effort to developing a new back-reflector. The research was focused on obtaining: 1) higher reflectance for low light loss, and 2) better texture for more enhanced light trapping.

We modified our batch evaporation system so that three metal layers can be evaporated in situ at elevated temperature under high vacuum. The ZnO layer was grown with RF sputtering from ZnO target at low Ar pressure (10 m Torr) in a RD Mathis sputtering system.

Different back-reflector systems have been systematically explored. We developed a new back-reflector Ag (hot)/Ag (cold)/ ZnO system that demonstrated 0.2 mA/cm^2 - 0.4 mA/cm^2 improvement in short circuit current (J_{ph}) of solar cells grown on these back-reflectors over those on previous back-reflectors (OBR83). The improvement in J_{ph} is mainly due to improved texture.

Ag Evaporated at Different Temperatures

We explored the reflection of light from Ag layers evaporated at different deposition temperatures. The deposition conditions and PDS results are listed in Table 5 for samples BR11, BR12, BR13, BR24, BR27 which were prepared at 300°C, 350°C, 25°C (Room Temperature), 25°C and 250°C respectively. From this table, the absorption loss at 1.5 eV (827 nm) is 1.6% for Ag evaporated at room temperature and approximately 9% for Ag evaporated at 300°C - 350°C. Although the RT deposited Ag has low reflection loss, it is not textured and does not significantly enhance solar cell current. Figure 5 illustrates SEM pictures of sample BR24, BR27, BR11 and BR12, prepared at deposition temperatures of RT, 250°C, 300°C, and 350°C. These pictures were taken at 40,000 x magnification and at a 60° incident angle. The defect in BR24 is purposely viewed for SEM focusing. Comparing these pictures, we find that the sample prepared at the highest temperature, BR12, shows the best texture among the group. Nevertheless, BR12 is not an ideal back-reflector because of its high absorption loss.

Aluminum-Chromium-Silver Layers

Besides Ag, we have also explored aluminum (Al) deposited at different temperatures. In general, Al has poorer reflectance compared to Ag. Al alone does not work as a good back-reflector. However, Al is readily textured. Therefore, our approach is to make back-reflectors with the texture of Al and the reflectance of Ag.

To utilize the texture of Al and the reflectance of Ag, layers of Al/buffer/Ag were extensively studied. The buffer layer between Al and Ag is necessary to prevent the alloying of Ag with Al during the Ag growth and subsequent cell making processes so that the high reflectance of Ag can be preserved. Among the Al/buffer/Ag group, an Al/Cr/Ag structure was extensively studied.

In Table 6, we show the deposition conditions and PDS results of some Al/Cr/Ag back-reflectors. These samples are grouped as hhh, hhc, and hcc according to the deposition temperatures of each of the three layers (h=hot, and c=cold).

Among the hhh group (BR7, BR9 and BR10), the light loss was higher when the deposition temperature was higher.

Table 5: Deposition conditions and reflection losses measured by PDS for Ag back-reflector layers deposited at different temperatures.

Sample #	Type	Ts	Thickness	Dep. Rate	Wavelength (nm)		
		(°C)	(Å)	Å/sec		λ=590nm	λ-827nm
						hν=2.1eV	hν=1.5eV
BR11	Ag	300	1500	2.0	V_{pds}(mV) Loss (%)	0.36 9.3	1.26 8.7
BR12	Ag	350	1500	2.0	V_{pds}(mV) Loss (%)	0.36 9.3	1.28 8.8
BR13	Ag	RT *	1500	2.0	V_{pds}(mV) Loss (%)	0.09 2.3	0.23 1.6
BR24	Ag	RT	1500	2.0	V_{pds}(mV) Loss (%)	0.10 2.6	0.26 1.8
BR27	Ag	250	1500	2.0	V_{pds}(mV) Loss (%)		

* RT indicates room temperature.

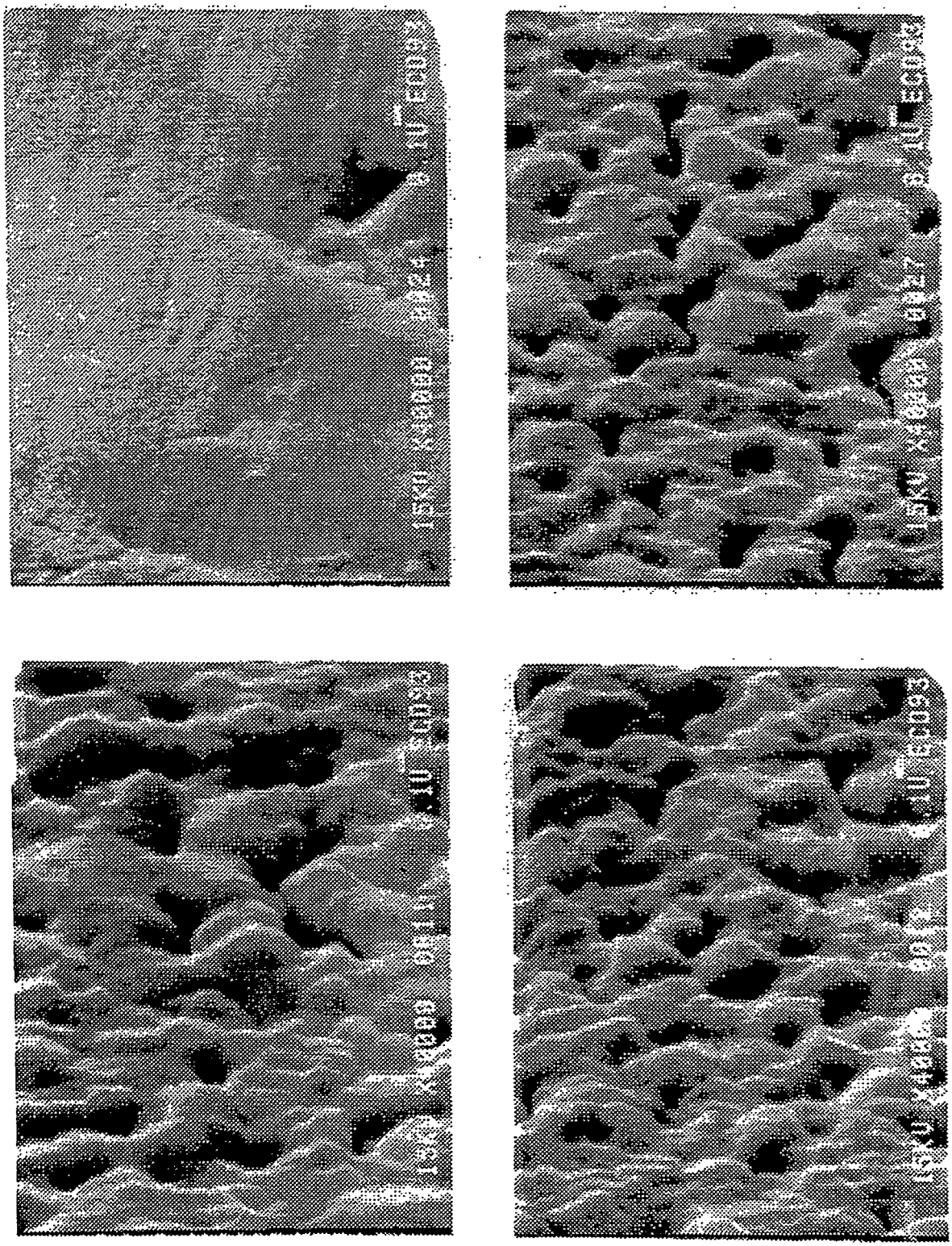

Figure 5: SEM photographs of Samples BR24 (upper left), BR27 (upper right), BR11 (lower left), and BR12 (lower right), evaporated at RT, 250°C, 300°C, and 350°C.

Table 6: Deposition conditions and reflection losses measured by PDS for Al/Cr/Ag back-reflectors.

Sample	Type	Al (bottom)			Cr (buffer)			Ag (top)				Wavelength (nm)	
Number		Ts	d	Rate	Ts	d	Rate	Ts	d	Rate			
		(°C)	(Å)	(Å/sec)	(°C)	(Å)	(Å/sec)	(°C)	(Å)	(Å/sec)		λ=590nm	λ=827nm
BR7	Ag/Cr/Ag	350	1100	2.0	350	1000	2.0	350	1000	2.0	V_{pds}(mV)	1.09	5.1
	h h h										Loss (%)	29.4	37.2
BR9	Ag/Cr/Ag	275	1000	2.0	275	100	2.0	275	1500	2.0	V_{pds}(mV)	0.66	2.66
	h h h										Loss (%)	17.8	19.4
BR10	Ag/Cr/Ag	275	1000	2.0	275	1000	2.0	200	1500	2.0	V_{pds}(mV)	0.62	2.3
	h h h										Loss (%)	16.7	16.8
BR15	Ag/Cr/Ag	275	1000	2.0	275	1000	2.0	RT	1500	2.0	V_{pds}(mV)	0.235	0.59
	h h c										Loss (%)	6.3	4.3
BR17	Ag/Cr/Ag	275	1000	2.0	RT	1000	2.0	RT	1500	2.0	V_{pds}(mV)	0.19†	0.49
	h c c										Loss (%)	5.1	3.6
BR18	Ag/Cr/Ag	275	1000	2.0	RT	1000	2.0	RT	1000	2.0	V_{pds}(mV)	0.20	0.59
	h c c										Loss (%)	5.4	4.3
BR31	Ag/Cr/Ag	225	1000	2.0	RT	1000	1.0	RT	1500	2.0	V_{pds}(mV)	0.74*	1.38
	h c c										Loss (%)	10.0	5.0
BR32	Ag/Cr/Ag	325	1000	2.0	RT	1000	1.0	RT	1500	2.0	V_{pds}(mV)	0.65	1.34
	h c c										Loss (%)	8.8	4.9

Notes: † The PDS measurement for BR17 & BR18 are after annealing at 325°C.
* PDS measurement for BR31 & BR32 are for samples on 7059 substrate.

To reduce the reflection loss, Al/Cr/Ag with hhc and hcc structures were investigated. hcc samples show the lowest light loss because; 1) The Ag evaporated at room temperature is more reflective, and 2) The Cr buffer layer is effective when Ag is deposited at low temperature and alloying of Ag to Al or Cr is minimized. To determine whether the Cr buffer layer still works when the Al/Cr/Ag is heated to high temperature in the subsequent cell making process, we annealed these samples to high temperature and found that the Cr buffer layer remains effective during post annealing. The details of the annealing experiments will be discussed later.

Figure 6 (a) through Figure 6 (c) are the SEM photographs of hcc samples BR31, BR 17 and BR32. The sample made with lowest Al deposition temperature, BR31 (225°C), shows the best texture among the three. To evaluate BR31 with a solar cell deposited thereupon, we first deposited 4000 Å of ZnO (ZnO 44) in the ZnO sputtering machine. An n-i-p solar cell (LL546) with a-Si i layer thickness of about 3000 Å was then deposited on this back-reflector in the LL system together with a piece of OBR83 in the same run. Quantum efficiencies of LL546 on BR31/ZnO44 and on OBR83 were measured and summarized in Table 7. The total integrated short circuit current J_{ph} for AM1.5 global spectrum is 14.1 mA/cm^2 for BR31/ZnO44 back-reflector and 15.8 mA/cm^2 for OBR83. The major loss in QE of BR31/ZnO44 is in the red. The relatively low J_{ph} is due to: 1) poor texture; and 2) interfaces loss at the Ag-ZnO interface and at the ZnO-n^+ interface.

Post Annealing

Since the back-reflectors will go through high temperature treatment in the subsequent cell making processes, we studied the back-reflector performance after post annealing. This study is especially important when the top Ag layer is evaporated at room temperature. Table 8 shows the PDS measurement before and after annealing at 300°C and 350°C for back-reflector BR7A, which is BR7 coated with another layer of cold evaporated Ag. We found that the reflectance was actually further improved with post annealing at 300°C, which is the temperature for the subsequent ZnO deposition and n-i-p cell deposition. The light loss at 1.5 eV decreases from 4.3% to 2.3% after annealing. This result indicates that the textured layer covered with cold Ag is effective since the cold Ag can provide good reflectance on any textured surfaces.

Textured Stainless Steel Substrate

One of the approaches is to texture the SS substrate. As long as we can engineer ideal texture on SS, an overlayer of RT evaporated Ag will provide high reflectance. We have so far studied two approaches to texture the SS substrate: bead blasting and fine powder grinding.

Bead blasting was carried out with two bead sizes, 5 μm and 1 μm in diameter. After bead blasting we coated the textured SS by a layer of 1500 Å. Ag evaporated at RT. Figure 7 (a) shows the SEM photograph of 1 μm bead blasted SS surface. Figure 7 (b) and Figure 7 (c) show the SEM photographs (4,000 magnification) of 5 μm bead blasted SS before and after being coated with cold Ag. The 1 μm bead blasted SS does not show acceptable texture for effective light scattering, while the 5 μm bead blasted SS provides structure in the scale of 15 μm. PDS measurement shows that the 5 μm bead blasted SS covered with cold Ag has low reflection loss of 2.2% at 826 nm. A solar cell was prepared on this back-reflector (LL542/ZnO43/BR30/5 μm SS) and provided 15.1 mA/cm^2 J_{ph} while the same cell on OBR83 gives 15.5 mA/cm^2 J_{ph}. The relatively low J_{ph} for the 5 μm SS is once again due to the lack of ideal texture. This may be due to; 1) low ratio of depth to size for the texture, and 2) structure on the scale of 15 μm size, which is too large as compared to the wavelength of red light in ZnO (0.35 μm).

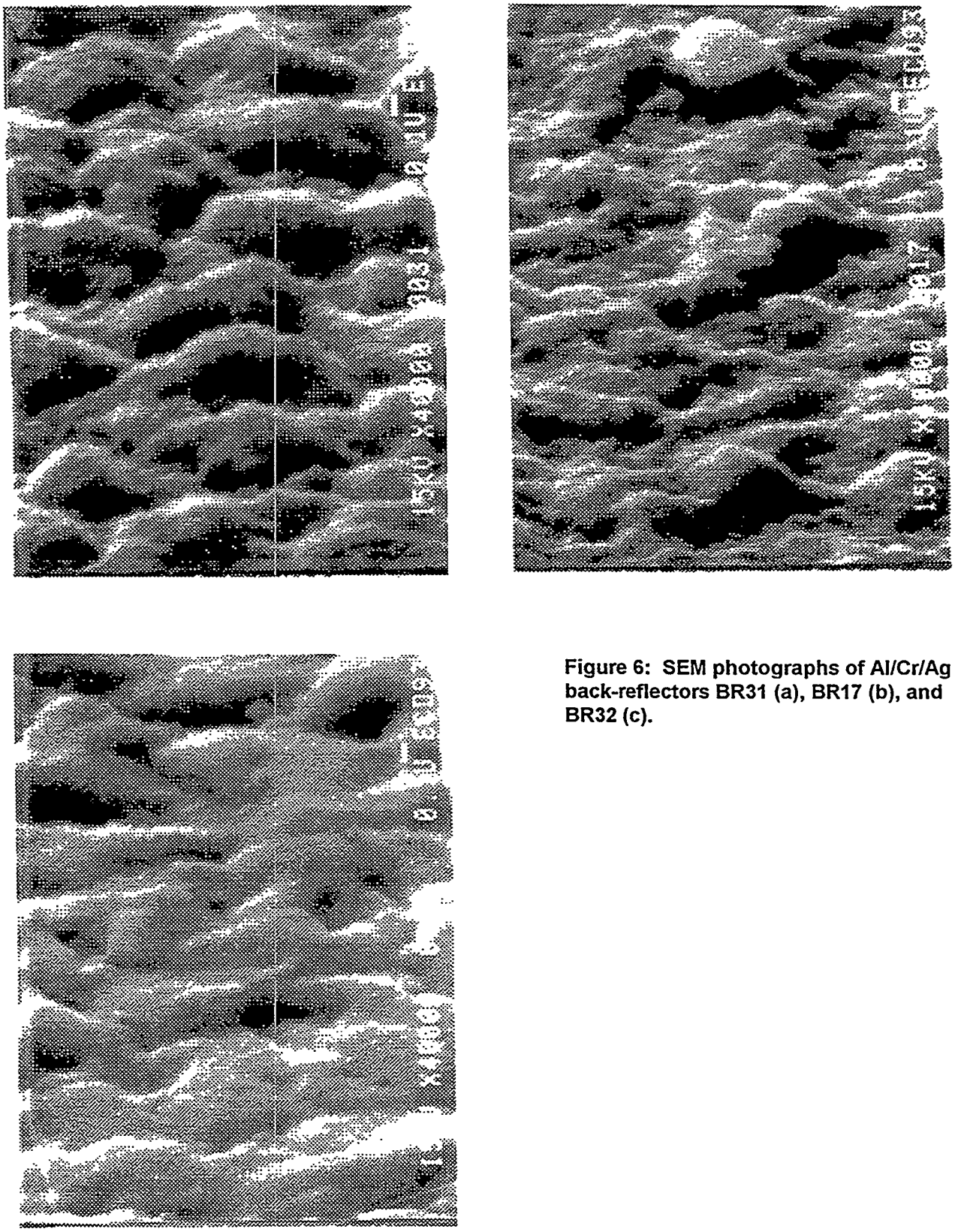

Figure 6: SEM photographs of Al/Cr/Ag back-reflectors BR31 (a), BR17 (b), and BR32 (c).

Table 7: Quantum Efficiency data for nip solar cells (LL546) on Al/Cr/Ag/ZnO and on reference OBR 83.

Sample	Jph (mA/cm^2)	QE @400nm	QE @590nm	QE @700nm
BR31/ZnO44/LL546	14.11	0.61	0.74	0.24
OBR83/LL546	15.75	0.53	0.84	0.38

Table 8: Reflection loss of sample BR7A (Al/Cr/Ag/Ag) after different post annealing step, measured with PDS.

Annealing Step		Wavelength (nm)					
		590	653	727	827	954	1127
Initial	V_{pds} (mV)	0.32	0.53	0.64	0.62	0.95	0.90
	Loss (%)	8.3	6.4	5.4	4.3	3.5	2.4
After 300°C	V_{pds} (mV)	0.16	0.255	0.33	0.33	0.52	0.52
30 min.	Loss (%)	4.1	3.1	2.8	2.3	1.9	1.4
After 350°C	V_{pds} (mV)	0.21	0.35	0.41	0.40	0.60	0.60
30 min.	Loss (%)	5.4	4.2	3.4	2.8	2.2	1.6

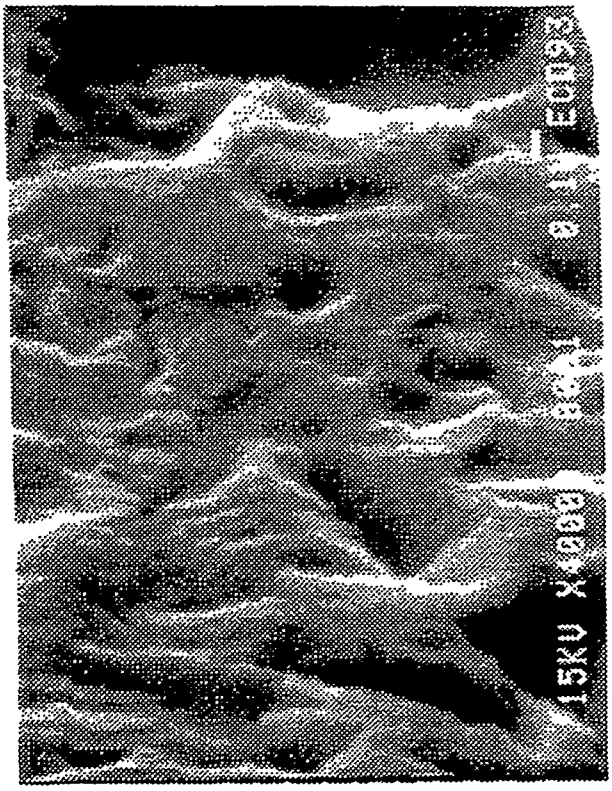

Figure 7: SEM photographs of 1 μm bead blasted s.s. surface (a), and 5 μm bead blasted s.s. surface before (b), and after (c) being coated with cold Ag.

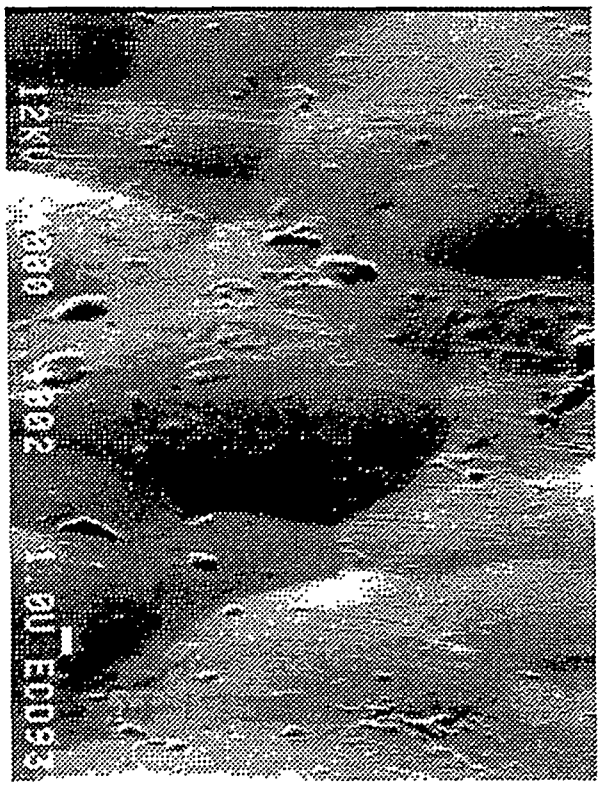

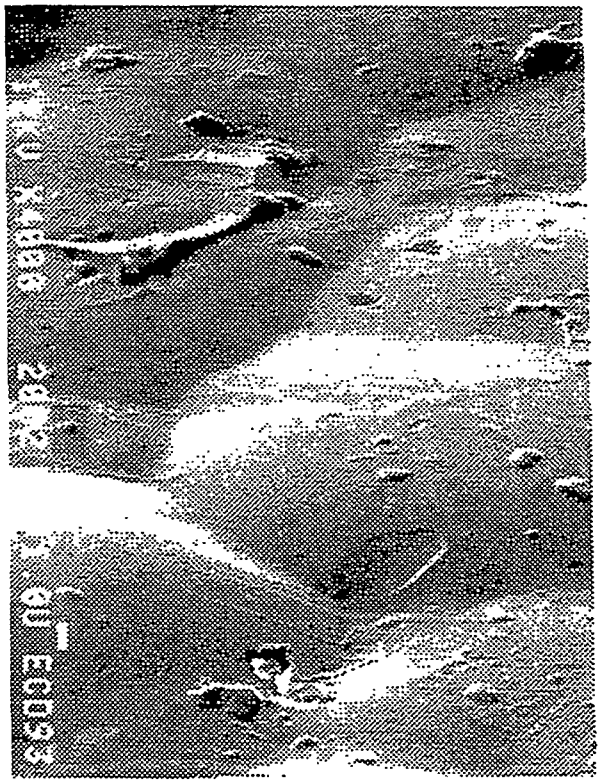

In order to obtain texture with appropriate size and depth, we textured SS surface by grinding the surface with 0.3 μm Al_2O_3 powder. This work is continuing.

Ag/Ag Back-Reflector

As we see from the SEM photographs in Figure 5 and Figure 6, the texture from Al is in the scale of 0.4 μm - 0.6 μm and the texture of Ag is in the scale of 0.2 μm - 0.4 μm, depending on other deposition conditions. If the optimum texture size is 0.3 μm - 0.4 μm, which is the wavelength of red light in ZnO, the texture size from Ag is a better candidate. Since the reflection loss increases when texture increases for high temperature evaporated Ag (hot Ag), cold Ag was deposited to cover the hot Ag to enhance the reflectance and to preserve the texture. In the Ag (hot)/Ag (cold) structure, a buffer layer is unnecessary since the alloying of cold Ag with hot Ag is not expected to reduce the reflectance. This Ag (hot)/Ag (cold) structure can be easily incorporated in our existing continuous roll-to-roll manufacturing line.

Table 9 (a), Table 9 (b) and Table 9 (c) show the deposition conditions, PDS spectrum, and Angular dependence of reflectance, respectively, for a standard Ag/Ag back-reflector. The light loss measured from PDS is much smaller than that of just the hot Ag layer. The light loss at 1.5 eV photons is 5.7%, which is still higher than the cold Ag layer alone. It is likely that this 5.7% loss is due to the texture, since for a textured surface, the normal incident light is no longer normal to the surface microscopically, so the reflectance decreases.

Figure 8 shows the SEM photographs of two Ag/Ag samples (BR48 and BR49). The top two graphs were taken with normal electron beam incidence and at a relative lower magnification of 10,000. The lower graphs were taken at 60° angle at 40,000 magnification. In both samples, the size of the grains are around 0.4 μm, which is believed to be appropriate for the red light scattering.

We prepared a series of solar cells on the Ag/Ag back-reflectors together with reference OBR83. In Table 10, we list the deposition conditions of four Ag/Ag samples (BR34, BR48, BR49 and BR50) and the QE data of the solar cell on these back-reflectors. The QE curves of these samples are shown in Figure 9. Comparing the QE curve of Ag/Ag back-reflector with those on OBR83, we see, on the average, 0.2 mA/cm^2 higher current density. The increase in the current is in two wavelength regions: in the red and in the blue. The increase in the red is mainly due to the improvement in the enhanced texture, as evidenced by the lack of interference fringes in the cells on Ag/Ag back-reflectors. The increase in the blue is probably due to the decrease in the reflection loss of the ITO coating when the surface is textured, since; 1) normal incident light enters the ITO at a non-normal incident angle microscopically; and 2) the ITO is effectively thinner. This results in a lower reflection loss at the front surface, thus enhancing the QE at the blue. Figure 10 shows a QE curve with QE=73% at 400 nm for an a-Si n-i-p solar cell. This high blue QE is mainly due to the enhancement from texture.

We post-annealed one Ag/Ag back-reflector sample (BR61) at 300°C for 60 min. before the ZnO deposition. The texture is shown to have been significantly improved, as we see from the angular dependence of reflection measurement in Table 11. We then deposited ZnO and an n-i-p solar cell thereupon. Figure 11 shows the QE of an n-i-p cell with the same i layer thickness as other n-i-p samples. The J_{ph} of this sample is 17.2 mA/cm^2. The lack of interference fringes and the enhancement in the red response indicate good light trapping from this texture. Since every Ag/Ag sample is "post annealed" in the ZnO deposition system, the added improvement in current from the annealed BR61 suggests that extra annealing time at high temperature improves the back-reflector.

Table 9: Deposition conditions, PDS results and angular dependence of reflectance for standard Ag/Ag back-reflector (BR66).

(a) deposition parameter (BR66)

Ag (bottom layer):	Ts	=	400°C
	Thickness	=	1000 Å
	Dep. Rate	=	1.3 Å/sec.
Ag (top layer)	Ts	=	RT
	Thickness	=	1500 Å
	Dep. Rate	=	15 Å/sec.

(b) PDS results (BR66)

	Wavelength (nm)					
	590	653	727	827	954	1127
V_{pds} (mV)	0.33	0.607	0.76	0.83	1.63	2.00
Loss (%)	8.5	7.3	6.4	5.7	5.9	5.3

(c) Angular dependence

Detector output:	
Incident beam:	2.5 mA
Reflector beam:	0.366mA at $\theta = 0^o$
	1.17×10^{-3} mA at $\theta = 30^o$
	0.645×10^{-3} mA at $\theta = 60^o$
Percentage of specular reflected light:	14..6%
Percentage of scattered reflected light:	80%

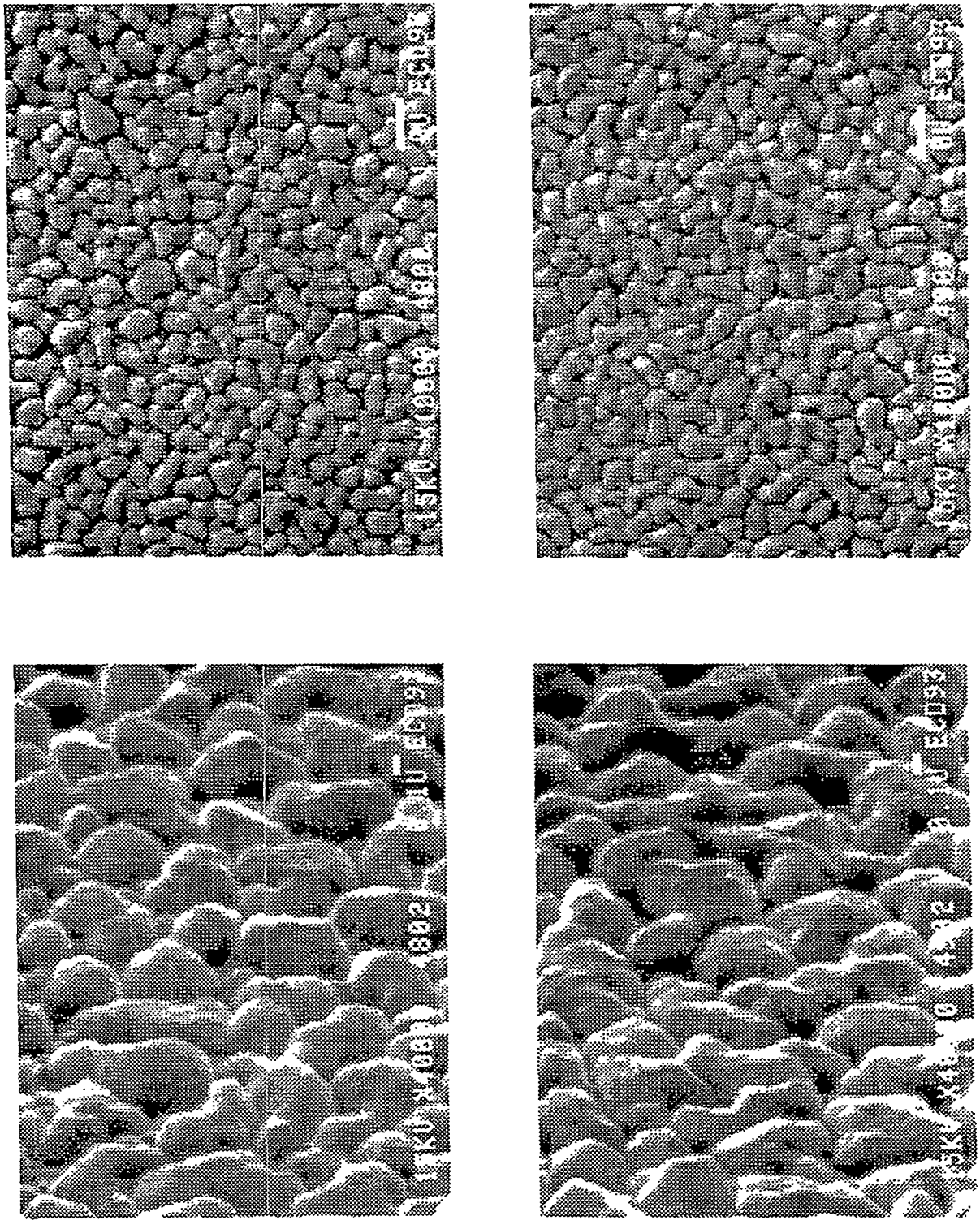

Figure 8: SEM photographs of two Ag/Ag back-reflectors (BR48 and BR49).

Table 10: Deposition conditions of Ag/Ag back-reflector and the QE data of solar cells on these back-reflectors and on reference back-reflector.

Sample #	Ag (bottom)			Ag (top)				QE of cells on Ag/Ag back-reflector				QE of cells on OBR 83			
	Ts (°C)	d (Å)	Rate Å/sec	Ts (°C)	d (Å)	Rate Å/sec	Solar cellrun#	Jph	Q400	Q590	Q700	Jph	Q400	Q590	Q700
BR34	350	1000	1.3	RT	1500	2.0	LL562	16.87	0.60	0.86	0.47	16.67	0.57	0.87	0.455
BR48	400	1000	0.5	RT	1500	15	LL565	16.69	0.65	0.85	0.42	16.49	0.64	0.86	0.34
BR49	350	1500	1.3	RT	1700	15	LL566	16.95	0.64	0.856	0.47	16.64	0.59	0.87	0.39
BR50	450	1000	0.5	RT	1500	15	LL567	17.00	0.63	0.87	0.47	16.77	0.60	0.88	0.41

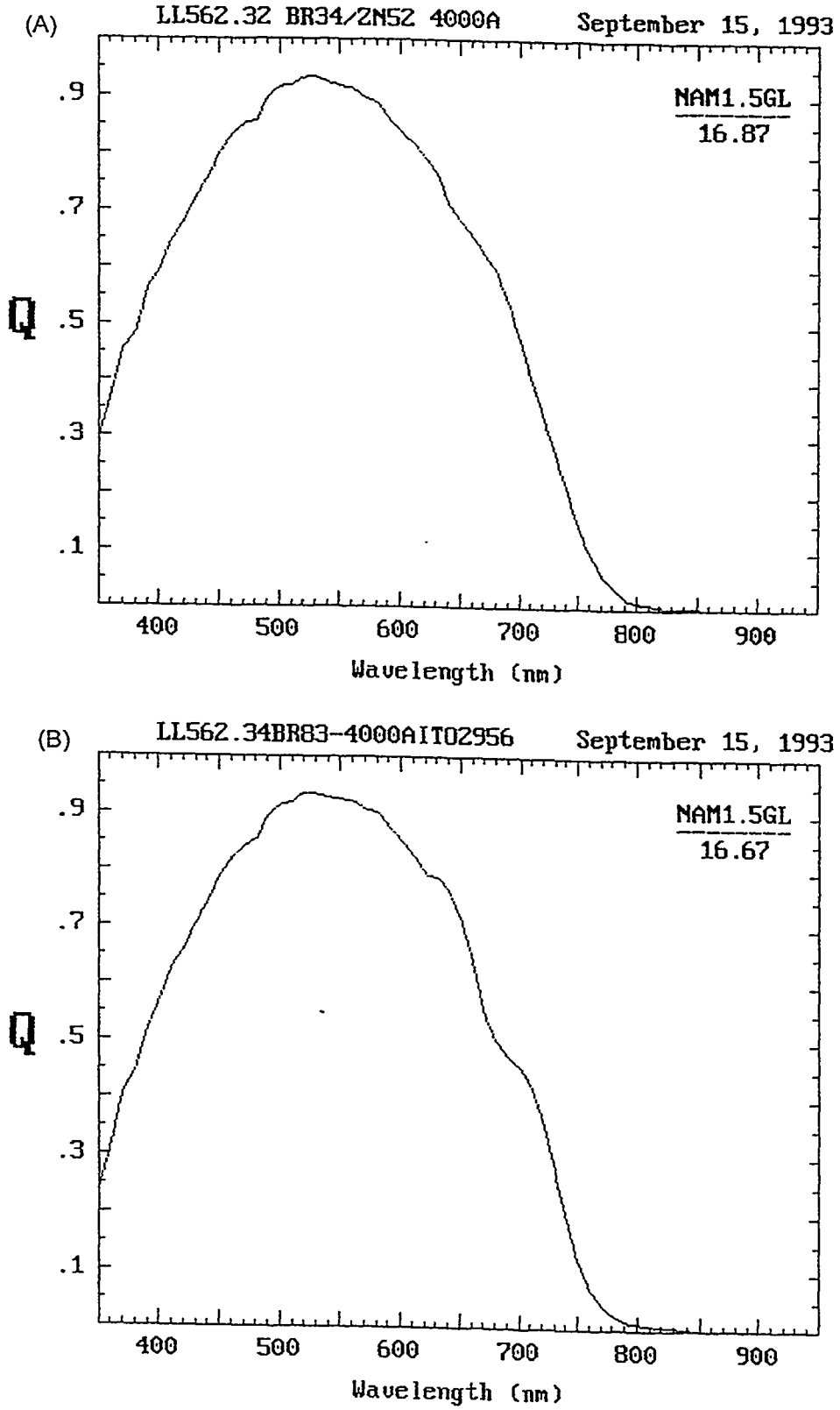

Figure 9: QE curves of solar cells on Ag/Ag back-reflectors and on OBR83. LL562 on BR34 (a), LL562 on OBR83 (b).

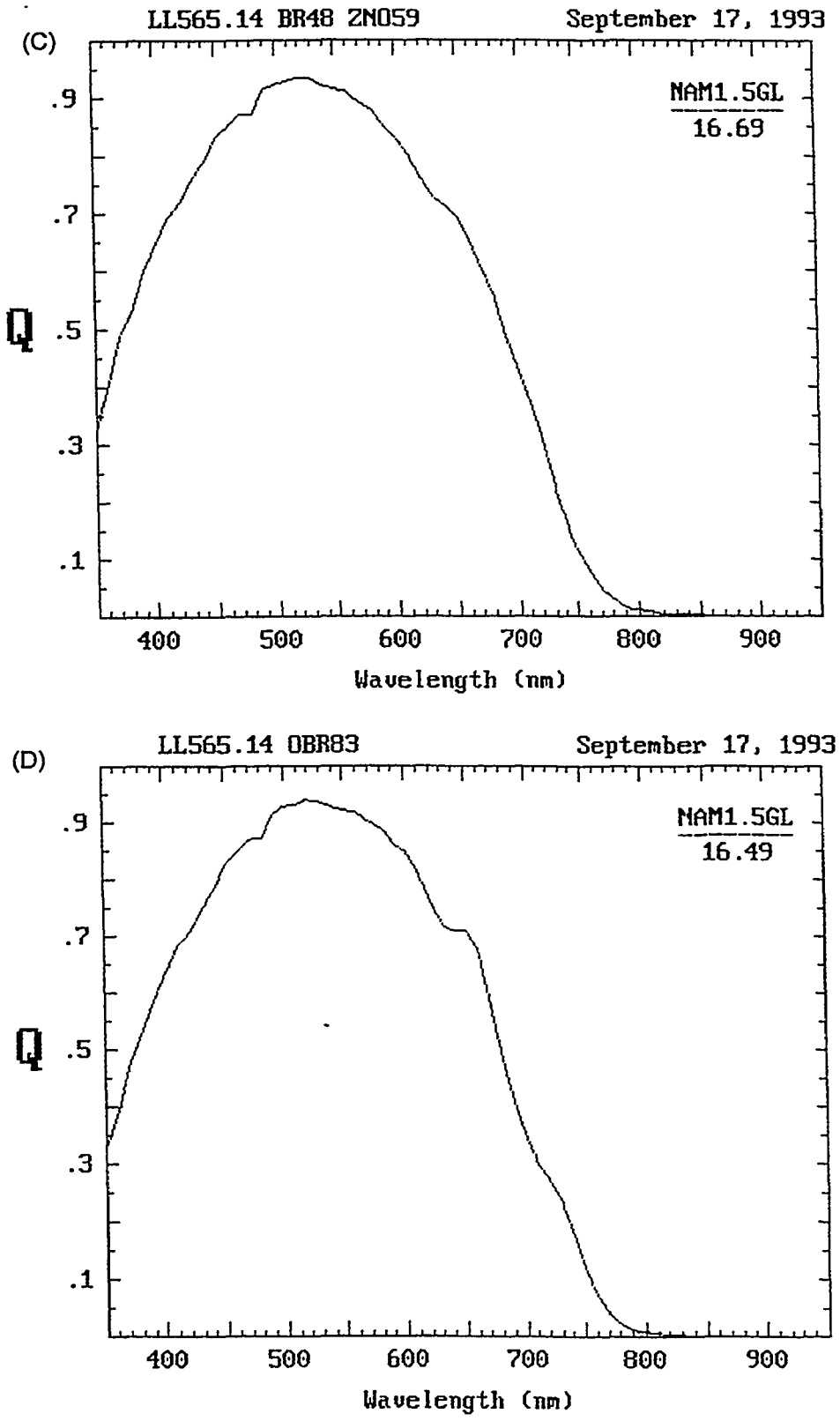

Figure 9: QE curves of solar cells on Ag/Ag back-reflectors and on OBR83. LL565 on BR48 (c), LL565 on OBR83 (d).

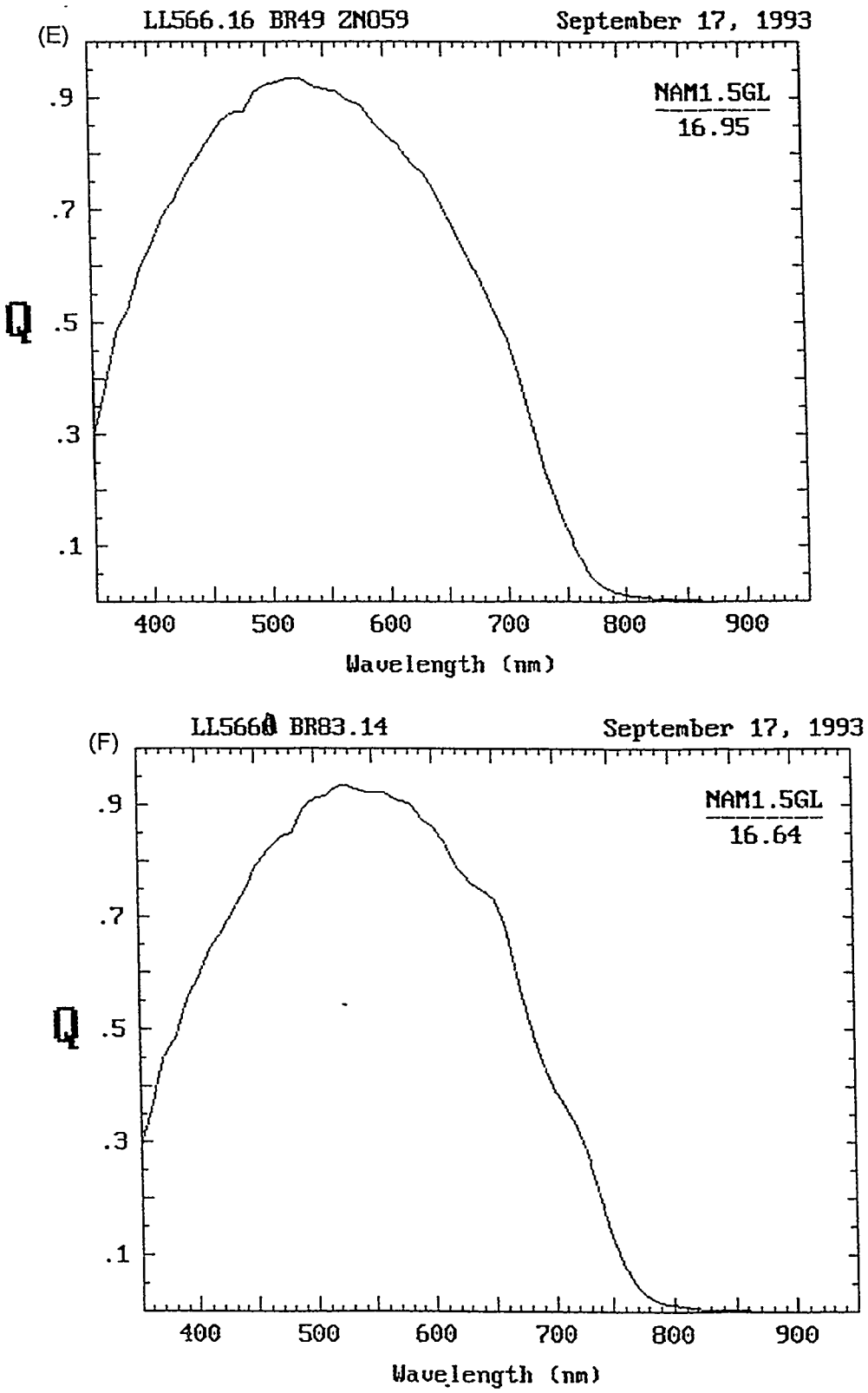

Figure 9: QE curves of solar cells on Ag/Ag back-reflectors and on OBR83. LL566 on BR49 (e), LL566 on OBR83 (f).

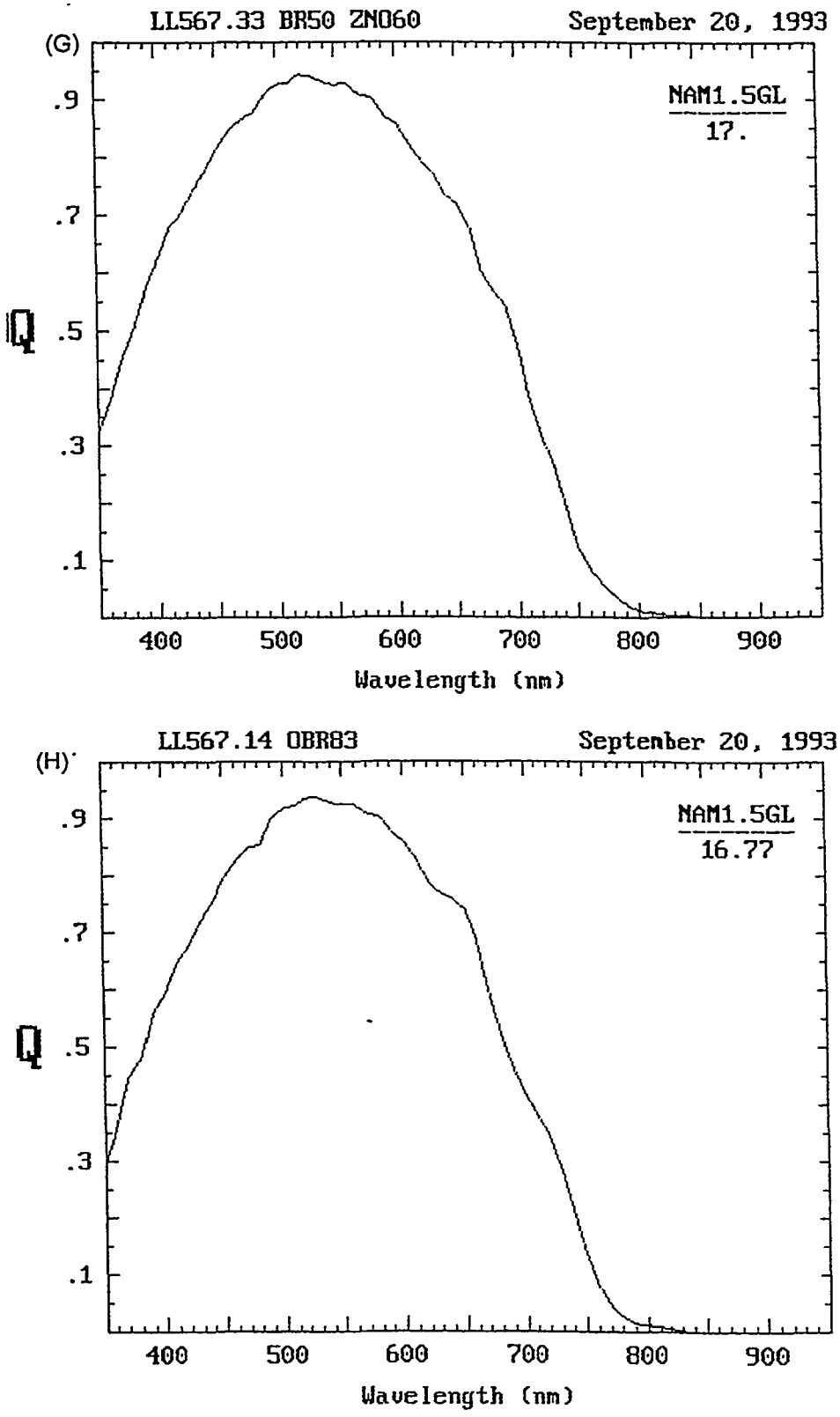

Figure 9: QE curves of solar cells on Ag/Ag back-reflectors and on OBR83. LL567 on BR50 (g), LL567 on OBR83 (h).

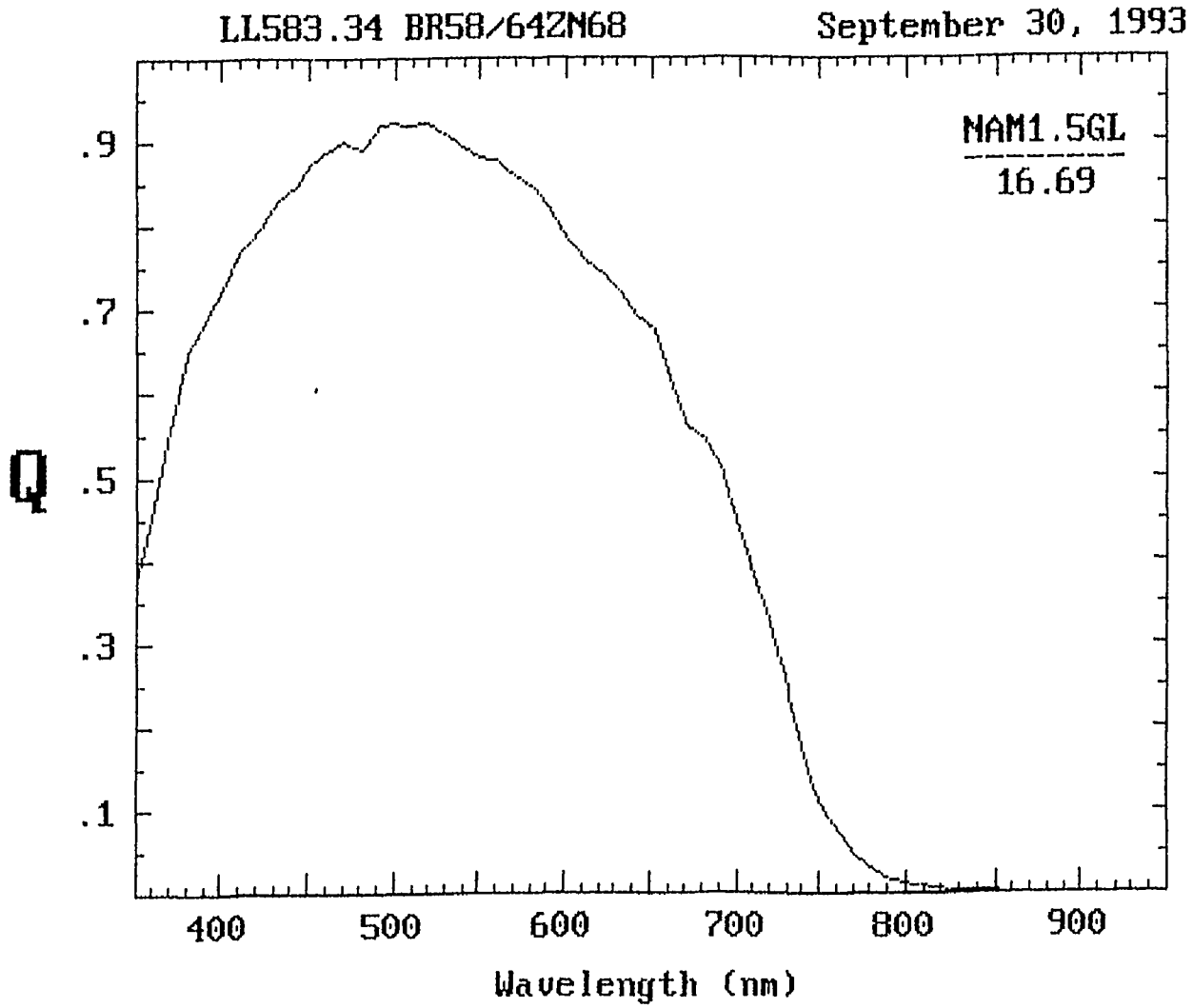

Figure 10: QE curve of a solar cell on textured Ag/Ag back-reflector showing QE=73% at 400nm.

Table 11: Angular Dependence of Reflection of Ag/Ag back-reflector before and after annealing at 300°C for 60 min.

Before Annealing

Detector output:

Incident beam:	2.5 mA
Reflected beam:	0.538 mA at $\theta = 0^o$
	1.05×10^{-3} mA at $\theta = 30^o$
	0.608×10^{-3} mA at $\theta = 60^o$
Percentage specular reflected light:	21.5%
Percentage of scattered reflected light:	73.8%*

After Annealing:

Detector output:

Incident beam:	2.5mA
Reflected beam:	0.153 mA at $\theta = 0^o$
	1.41×10^{-3} mA at $\theta = 30^o$
	0.854×10^{-3} mA at $\theta = 60^o$
Percentage of specular reflected light:	6.1%
Percentage of scattered reflected light:	101%*

* Calculated from equation (1) assuming $I(\theta) \propto \cos\theta$ relation

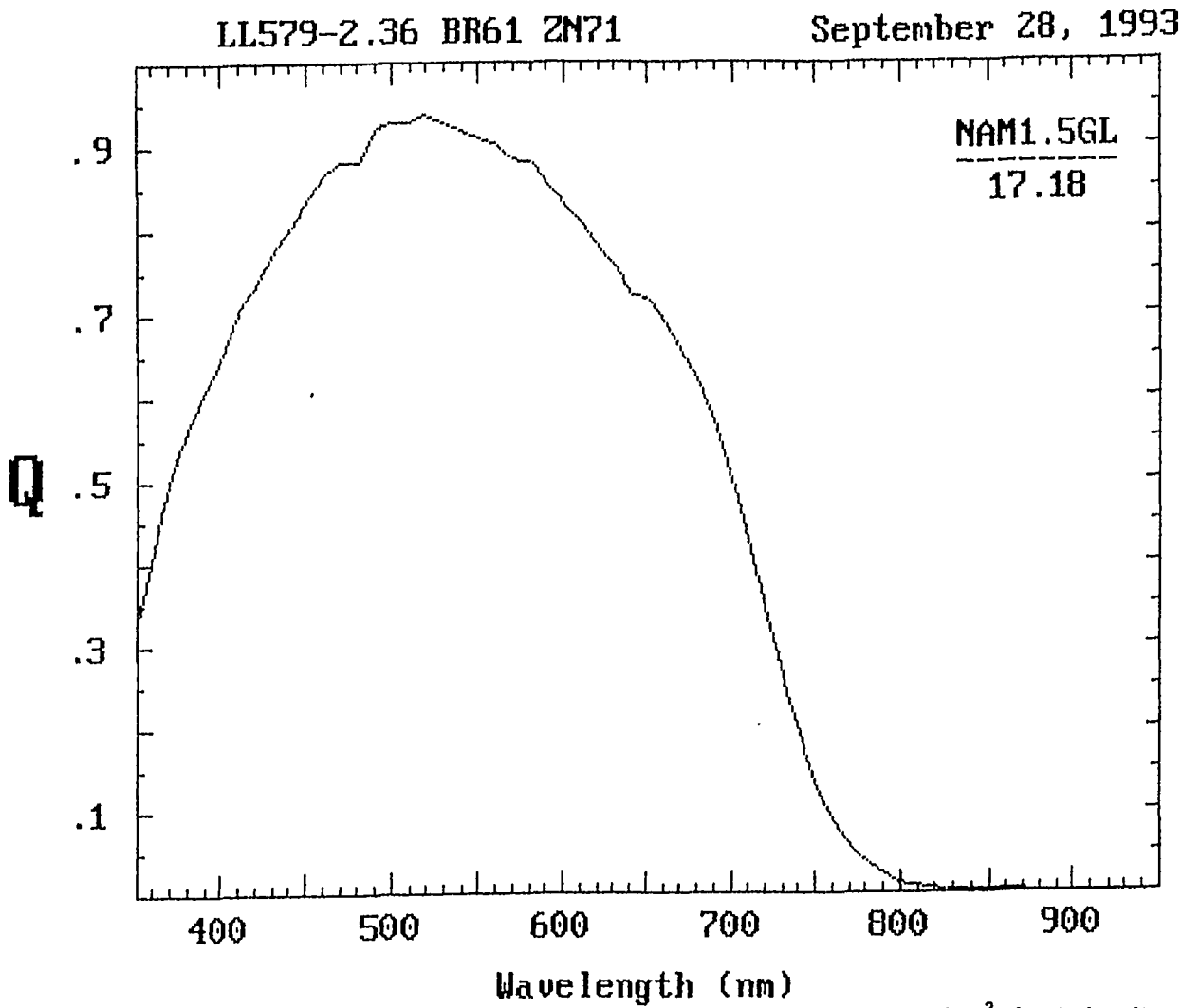

Figure 11: QE curve of an n-i-p solar cell on Ag/Ag back-reflector showing 17.2 mA/cm^2 short circuit current.

Optimization of Back-Reflector Deposition in Continuous Roll-to-Roll Deposition Machine

During this program period, we have also constructed a continuous roll-to-roll sputtering chamber for the deposition of Ag-ZnO back-reflectors. The machine is equipped with four DC magnetron sputtering targets. An upward sputtering configuration is used so that particulates do not accumulate on the web surface. Typically, we install one Ag target, two ZnO targets for the Ag/ZnO back-reflector deposition and one ITO target for the deposition of top conductive layer. We can also install two metal targets for the deposition of multiple metal layer back-reflectors and install a ITO target only when the machine is needed for ITO deposition.

A diffusion pump is installed in the sputter chamber to maintain an Ar background pressure of around 2 mTorr during sputtering.

The gas gates on both sides of the sputter chamber are designed such that the sputter chamber is well isolated from the contaminants from other chambers, pressure gradation is properly maintained and the low deposition pressure can be maintained with the existing pumping system.

We have first optimized the uniformity of Ag/ZnO deposition through an improved gas flow pattern. The co-sputtering of neighboring Ag and ZnO targets is eliminated. The deposition conditions including substrate temperatures, sputtering power, deposition pressure, feedstock gas mixture, web traveling speed, the thickness of each layer, were investigated and optimized.

Standard a-Si n-i-p solar cells were deposited onto these back-reflectors to evaluate its performance. Figure 12 is the J-V curve of a n-i-p solar cell deposited on Ag/ZnO back-reflector produced in the continuous roll-to-roll sputtering machine. The short circuit current is 16.8 mA/cm^2. The same solar cell deposited on the reference back-reflector (OBR83) shows a J_{sc} of 16.4 mA/cm^2.

In summary, under Task 6,

1. A PDS technique was developed for use as an important tool to measure the performance of the back-reflector.

2. Ag (high T)/Ag (low T)/ZnO system has been developed. It offers high reflectance and high texture. Short circuit current of 17.2 mA/cm^2 was obtained for an approximately 4000 A a-Si n-i-p cell on this back-reflector.

3. We have optimized the deposition of Ag/ZnO back-reflectors in the newly constructed, at ECD's expense, multi-purpose continuous roll-to-roll deposition machine.

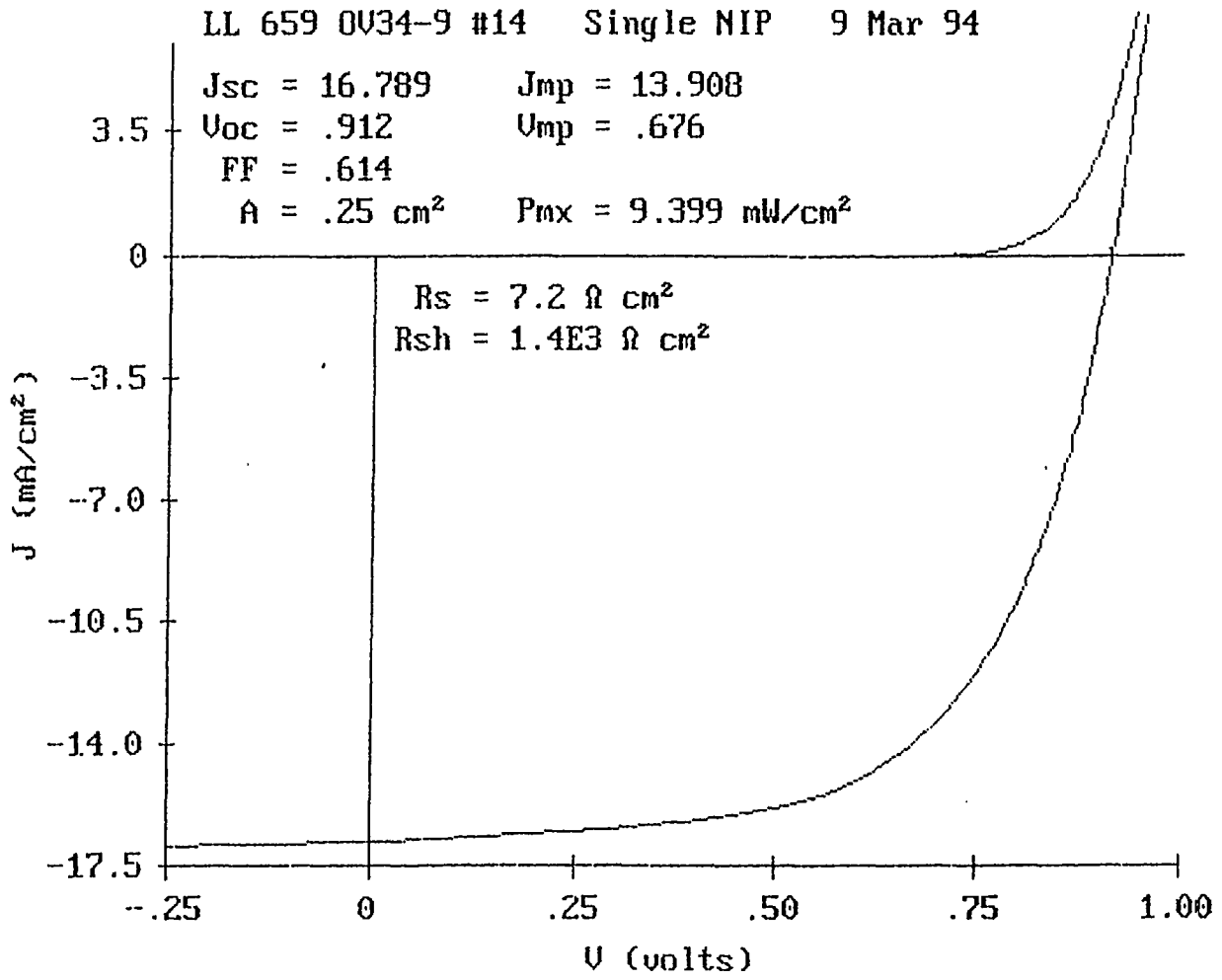

Figure 12: J-V curve of an a-Si n-i-p solar cell deposited on Ag/ZnO back-reflector produced in the sputter chamber of the continuous roll-to-roll deposition machine.

Task 7: Optimization of the Si-Ge Narrow Band-Gap Solar Cell

We designed and constructed, at ECD's expense, the multi-purpose continuous roll-to-roll deposition machine which is capable of producing triple-junction multiple band-gap solar cells with high stable efficiency. Machine design efforts have focused on improvements that will result in further increases in stable module efficiency.

The intrinsic layer deposition chamber is capable of producing high quality band-gap profiled narrow band-gap a-SiGe alloy using our proprietary gas diffusion tube and segmented cathode configuration. In this chamber, gas mixtures with different $GeH_4/(GeH_4 + Si_2H_6)$ are delivered to different parts of the cathode simultaneously for the continuous deposition of a-SiGe with profiled band-gap. Relatively more GeH_4 is delivered to the side of the chamber closer to the p chamber, so that a narrower band-gap is obtained for the sublayers near p layer in the n-i-p device.

Strict chamber and internal component cleaning methods were used. Internal effective surface area of the chambers has been minimized. Purged, double o-rings were used to reduce contamination from gas permeation through the o-rings. Additionally, ultra-clean assembly methods were implemented.

We have produced a-SiGe narrow band-gap solar cells in this newly constructed machine. Figure 13(a) is the J-V curve of an a-SiGe solar cell produced in this machine. The relatively high fill factor (FF) (FF=0.676) indicates the improved material quality. The FF under weak red illumination, as shown in Figure 13(b), also shows this point. The improved a-SiGe material quality is believed to be mainly due to the improved machine cleanliness described above.

The i deposition chamber is designed to deposit a-SiGe with a profiled band-gap. We have deposited a-SiGe solar cells with band-gap profiling, as shown in Figure 14(a) and Figure 14(b), and without band-gap profiling, as shown in Figure 15(a) and Figure 15(b). Except for the profiling in band-gap, these two samples were deposited under similar conditions. The V_{oc} is increased from 0.46 V to 0.62 V, J_{sc} increased from 11.0 mA/cm^2 to 12.3 mA/cm^2 and FF increased from 0.54 to 0.62 after the band-gap profiling is implemented.

A 10.2% stable efficiency has been recently achieved[21,22] for a 1 ft^2 a-Si alloy solar panel by United Solar Systems Corp., a joint venture company between ECD and Canon. This high efficiency module was produced using a-Si/a-SiGe/a-SiGe triple-junction, triple band-gap structure in a batch deposition process. The middle cell was made with mid-range band-gap (~1.6 eV) a-SiGe alloy to improve the solar cell stability.

To incorporate this triple-junction, triple band-gap solar cell design into ECD's continuous roll-to-roll deposition line, we have deposited and studied the a-SiGe alloy solar cells to be used as the bottom and middle cell of the triple band-gap a-Si alloy solar cells.

Figure 16(a) is the J-V curve of a narrow band-gap a-SiGe alloy solar cell, deposited on bare stainless steel, and is to be used as the bottom cell. Figure 16(b) is the J-V curves of this solar cell with weak blue and red illumination. The V_{oc} is 0.6 V and the red FF is 0.64. When a similar cell is deposited on a high performance back-reflector, J_{sc} of around 21 mA/cm^2 is expected.

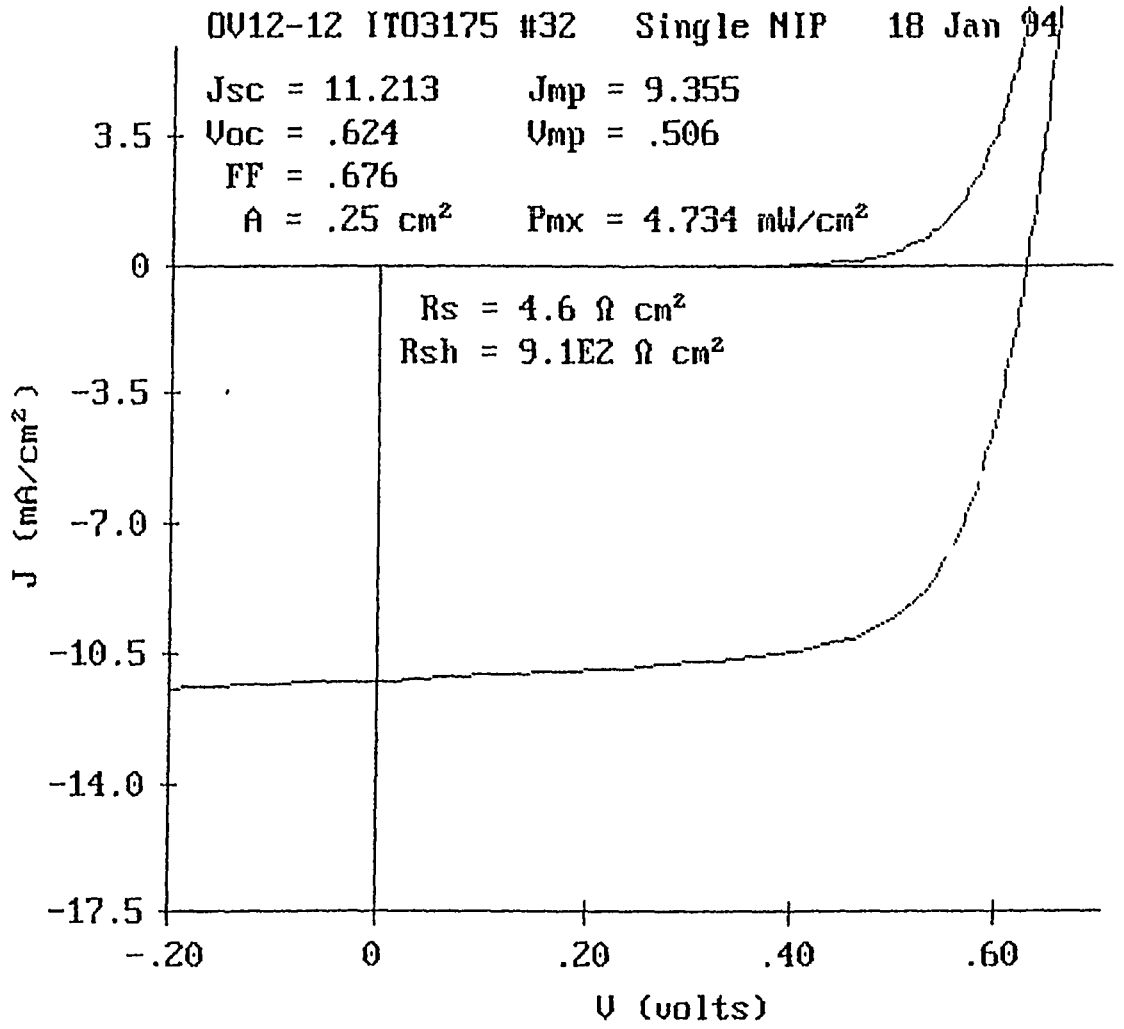

Figure 13(a): J-V curve of an a-SiGe solar cell produced in ECD's new continuous roll-to-roll deposition machine.

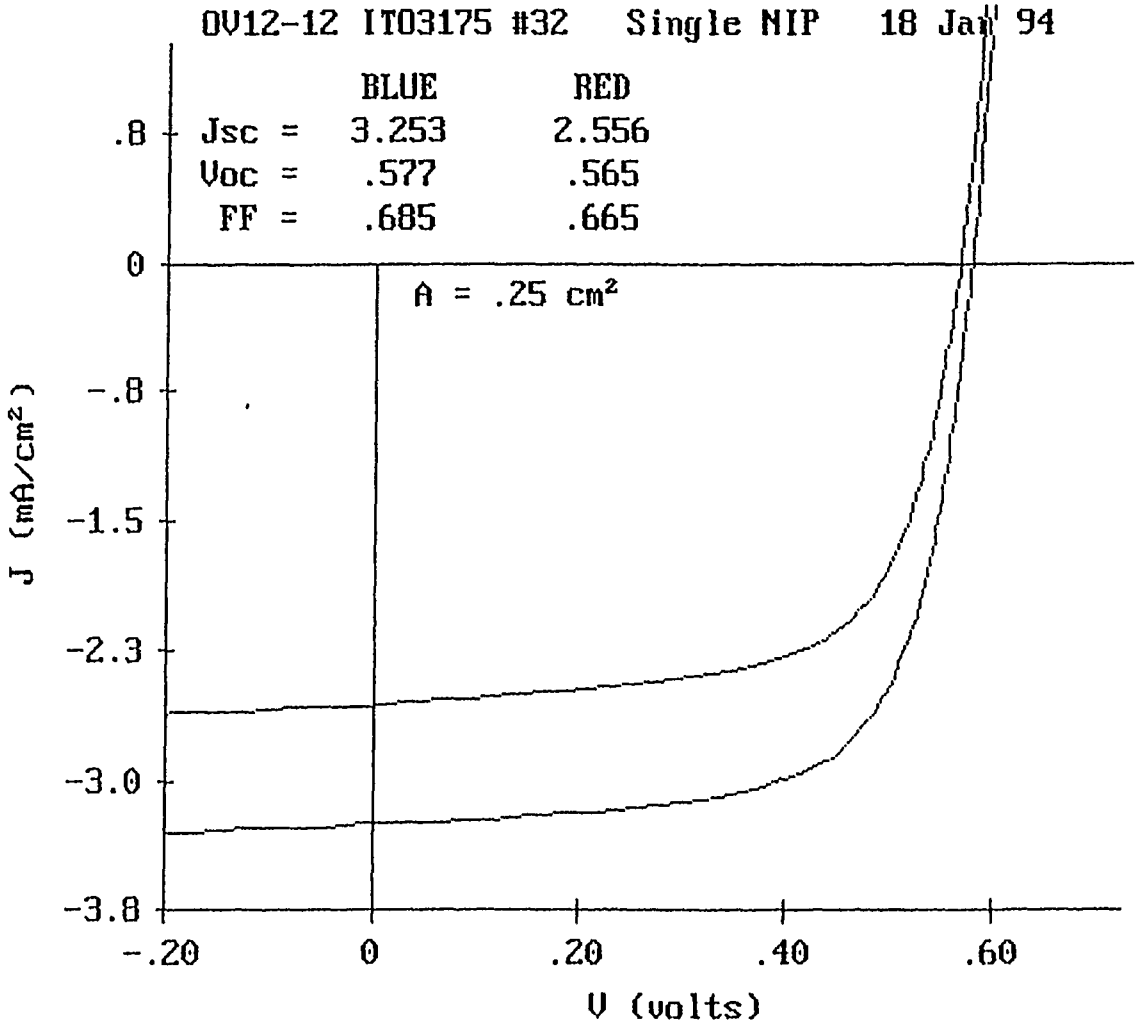

Figure 13(b): J-V curves of the a-SiGe solar cell under blue and red light.

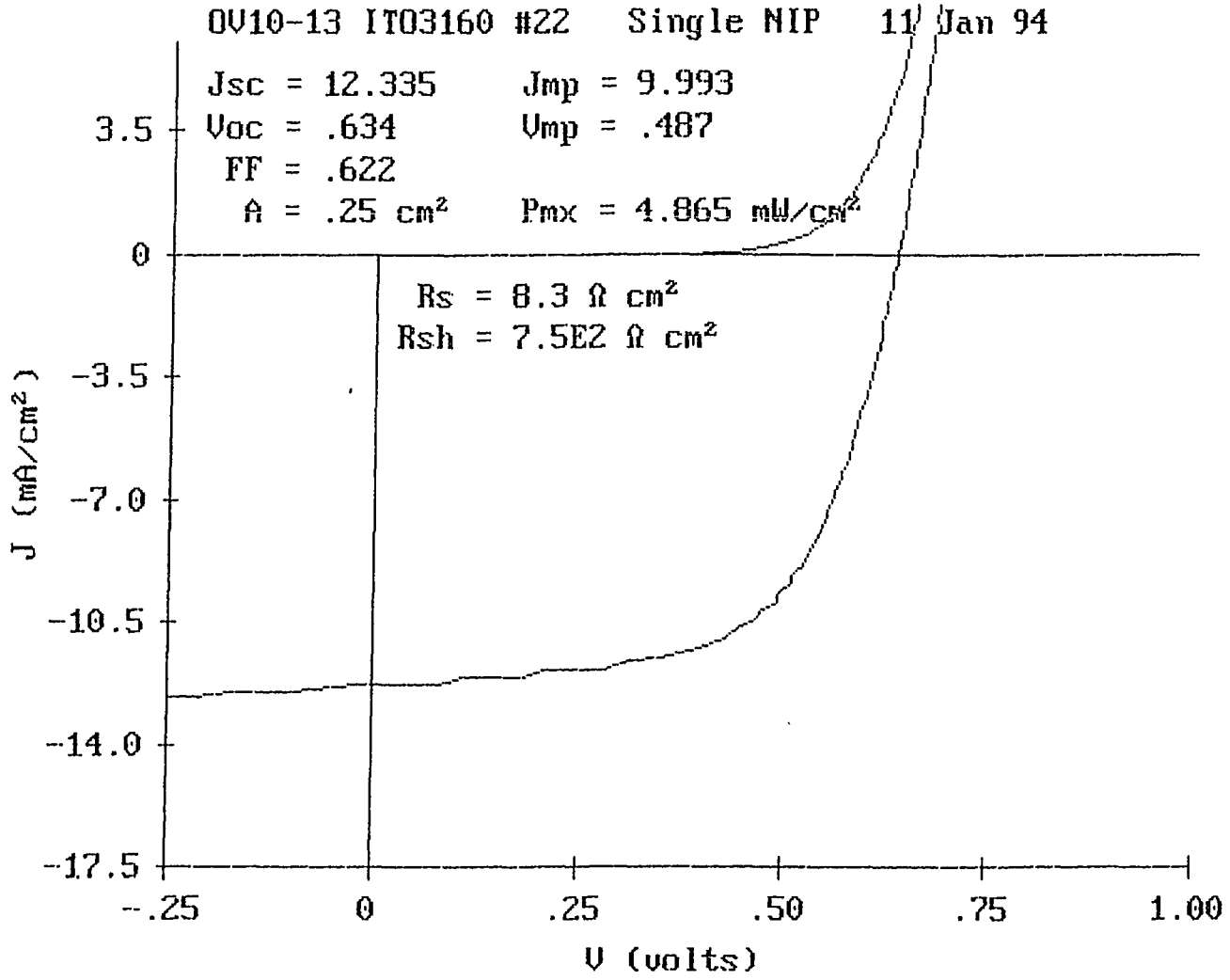

Figure 14(a): J-V curve of a band-gap profiled a-SiGe solar cell deposited on bare stainless steel.

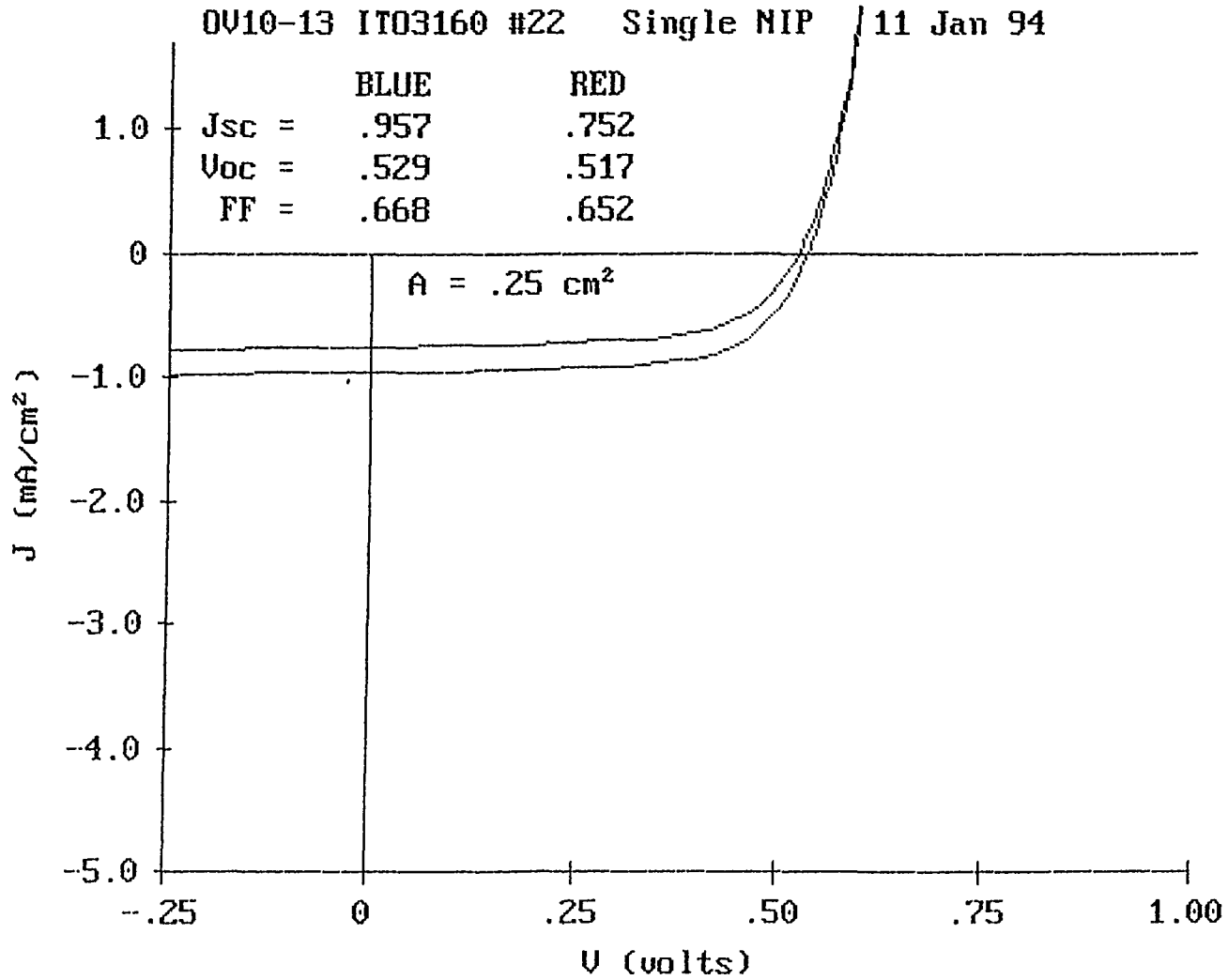

Figure 14(b): J-V curves of the a-SiGe solar cell under blue and red illumination.

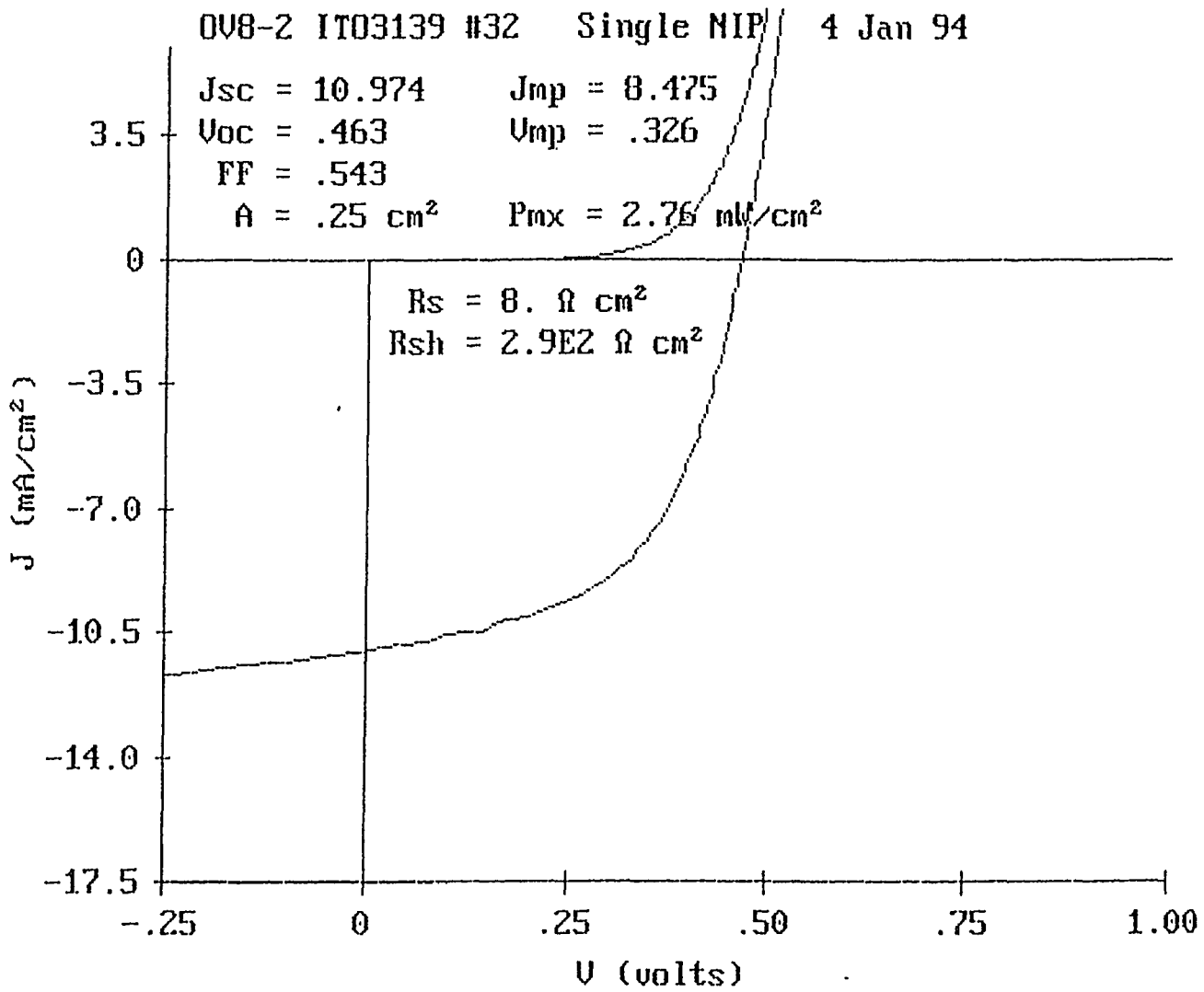

Figure 15(a): J-V curve of an a-SiGe solar cell without bandgap profiling.

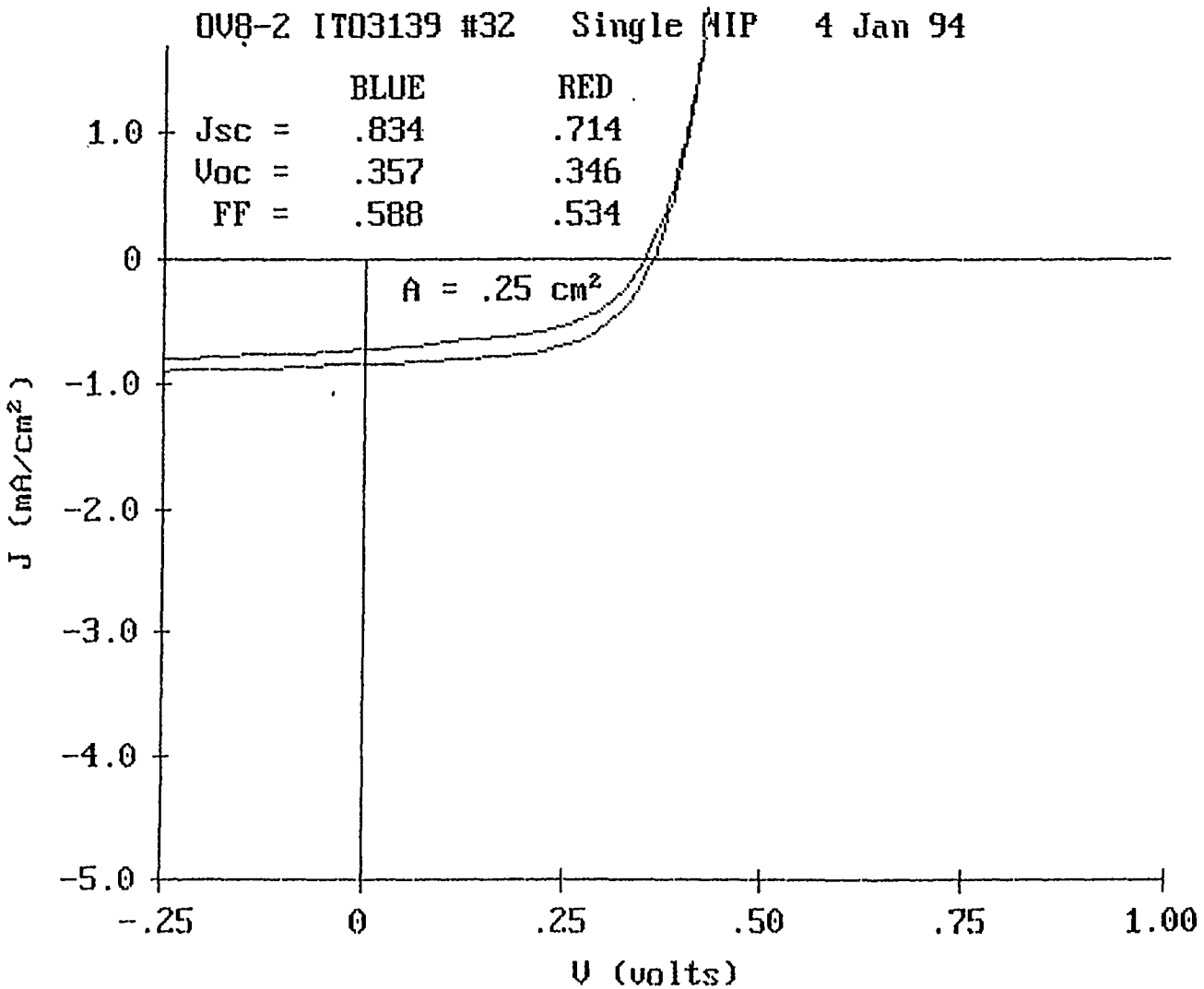

Figure 15(b): J-V curves of the a-SiGe solar cell without bandgap profiling under blue and red illumination.

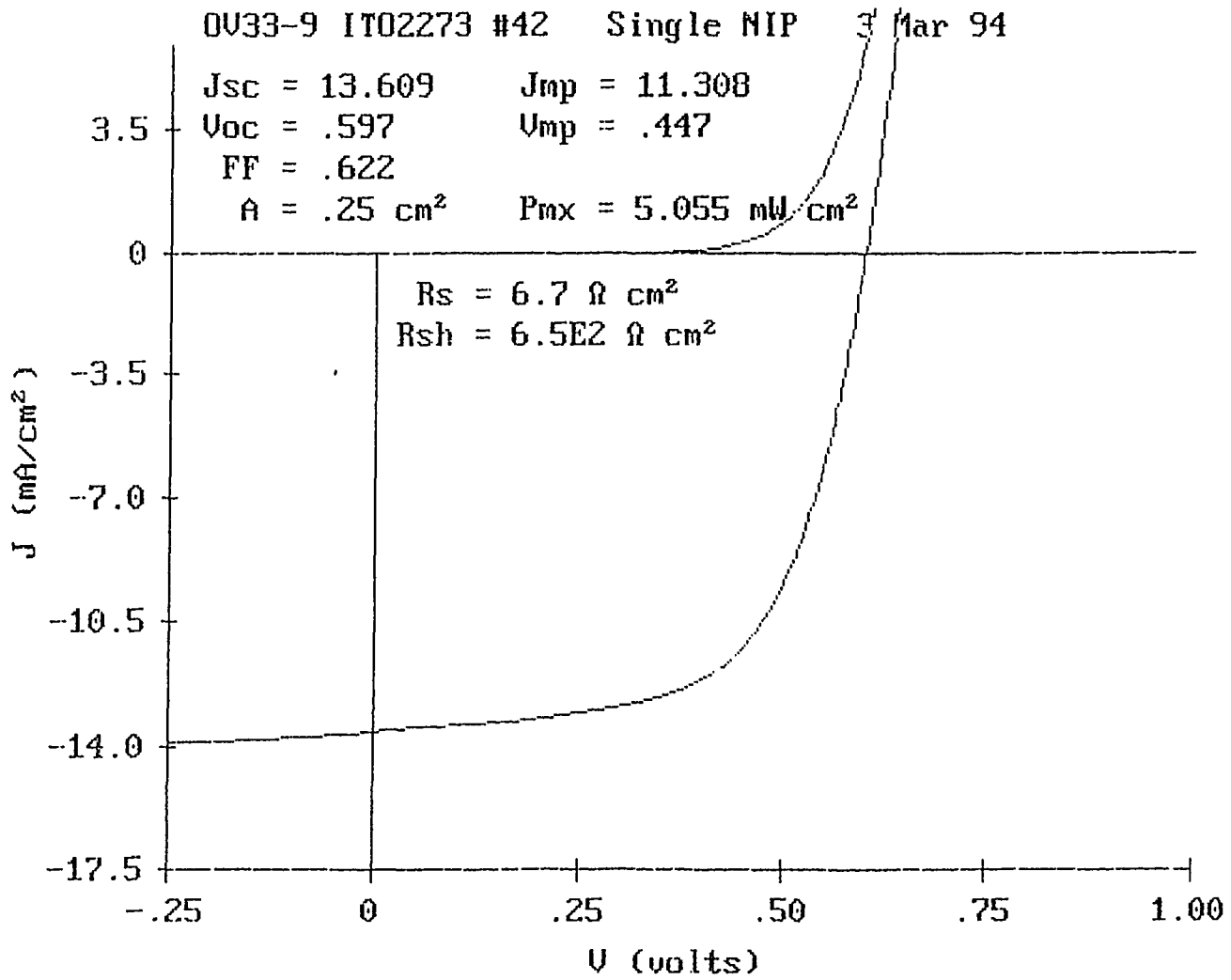

Figure 16(a): J-V curve of a narrow band-gap profiled a-Si-Ge solar cell to be used as the bottom cell of triple-junction, triple band-gap solar cell.

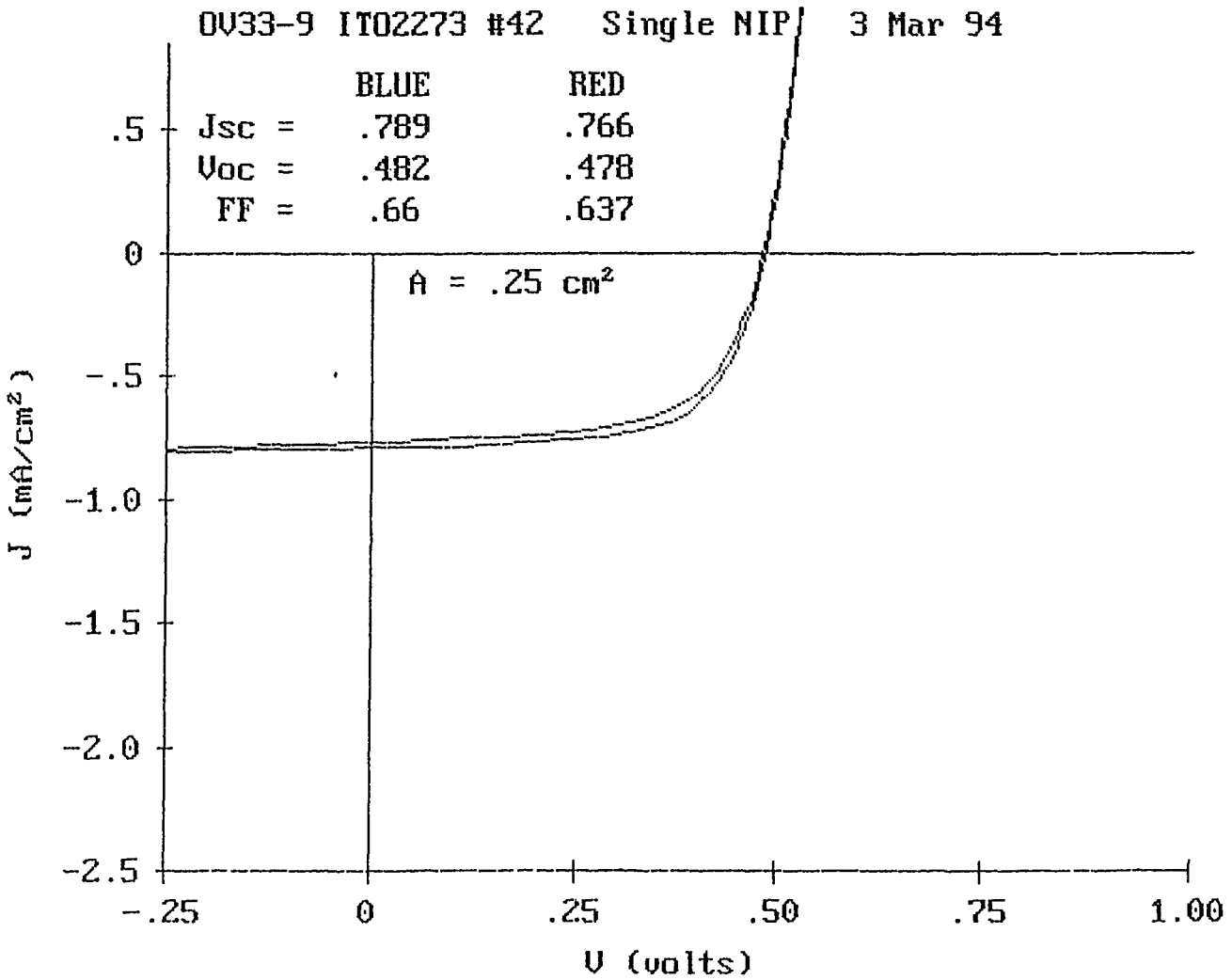

Figure 16(b): J-V curve of the narrow band-gap a-Si-Ge solar cell under blue and red illumination.

Figure 17(a) is the J-V curve of a middle band-gap a-SiGe alloy solar cell, deposited on bare stainless steel, and is to be used as the middle cell. Since the band-gap is smaller than that of a-Si, the middle cell i layer can be made much thinner, yet maintain the proper current matching. Consequently, the triple-junction cell will have higher stable efficiency. Figure 17(b) is the J-V curves of this middle band-gap a-SiGe solar cell under blue and red illumination. The FF under white and colored lights are high.

We have also studied the narrower band-gap a-SiGe alloy solar cell with the aim of improving the red response. Figure 18 is the quantum efficiency (QE) curve of such a solar cell showing QE=45% at 800 nm.

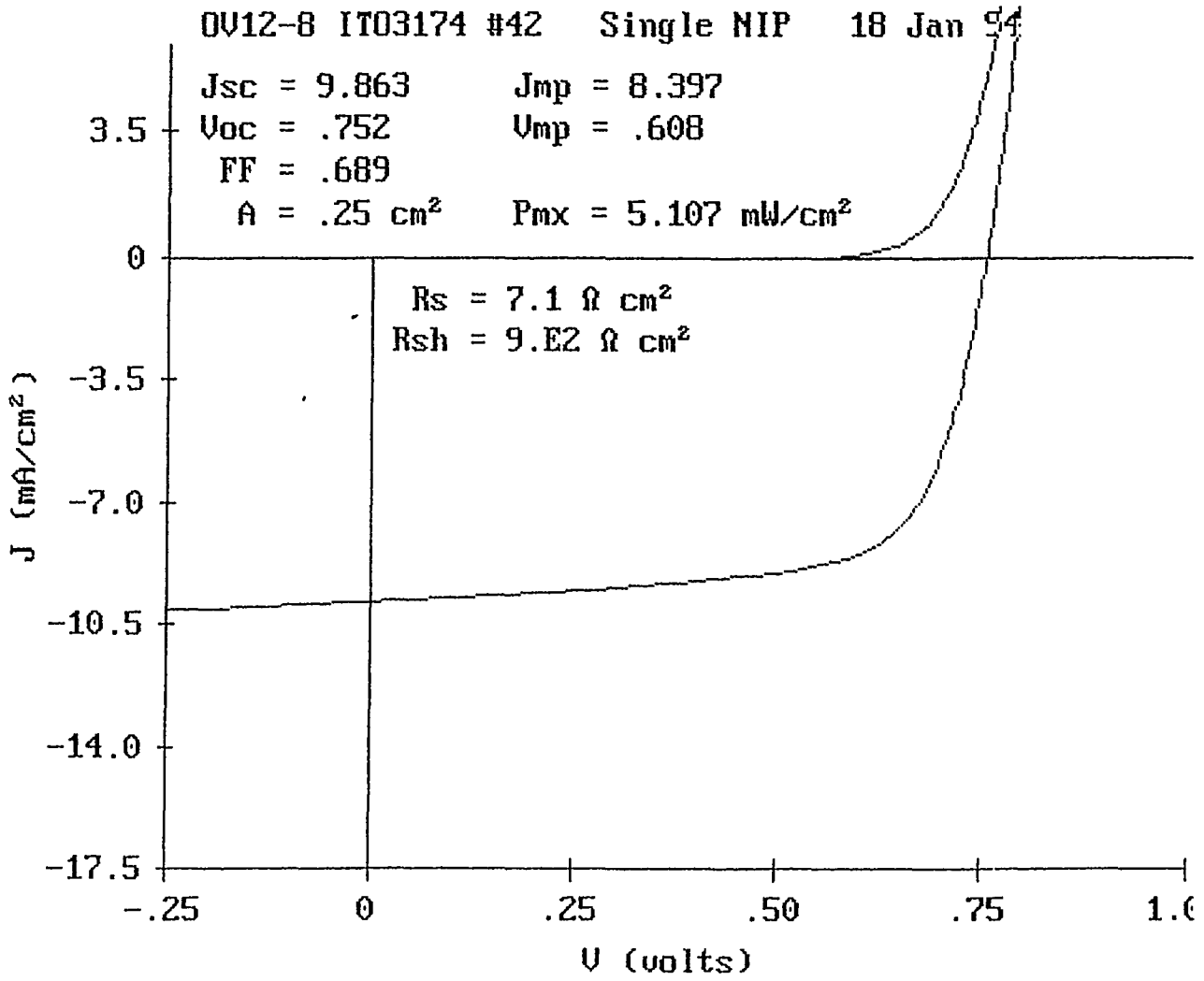

Figure 17(a): J-V curve of an a-SiGe solar cell to be used as the middle cell.

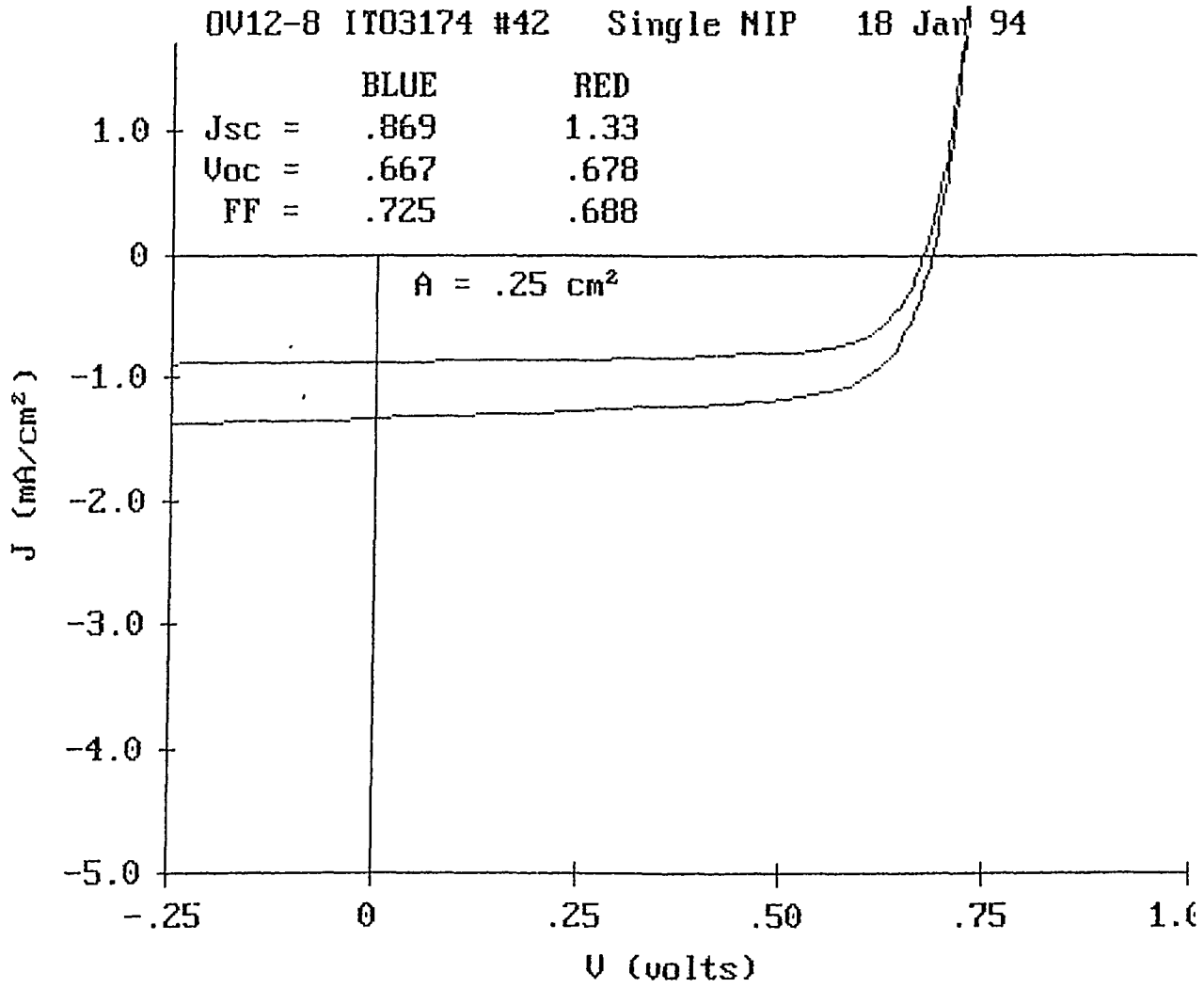

Figure 17(b): J-V curves of the a-SiGe solar cell to be used as the middle cell under blue and red illumination.

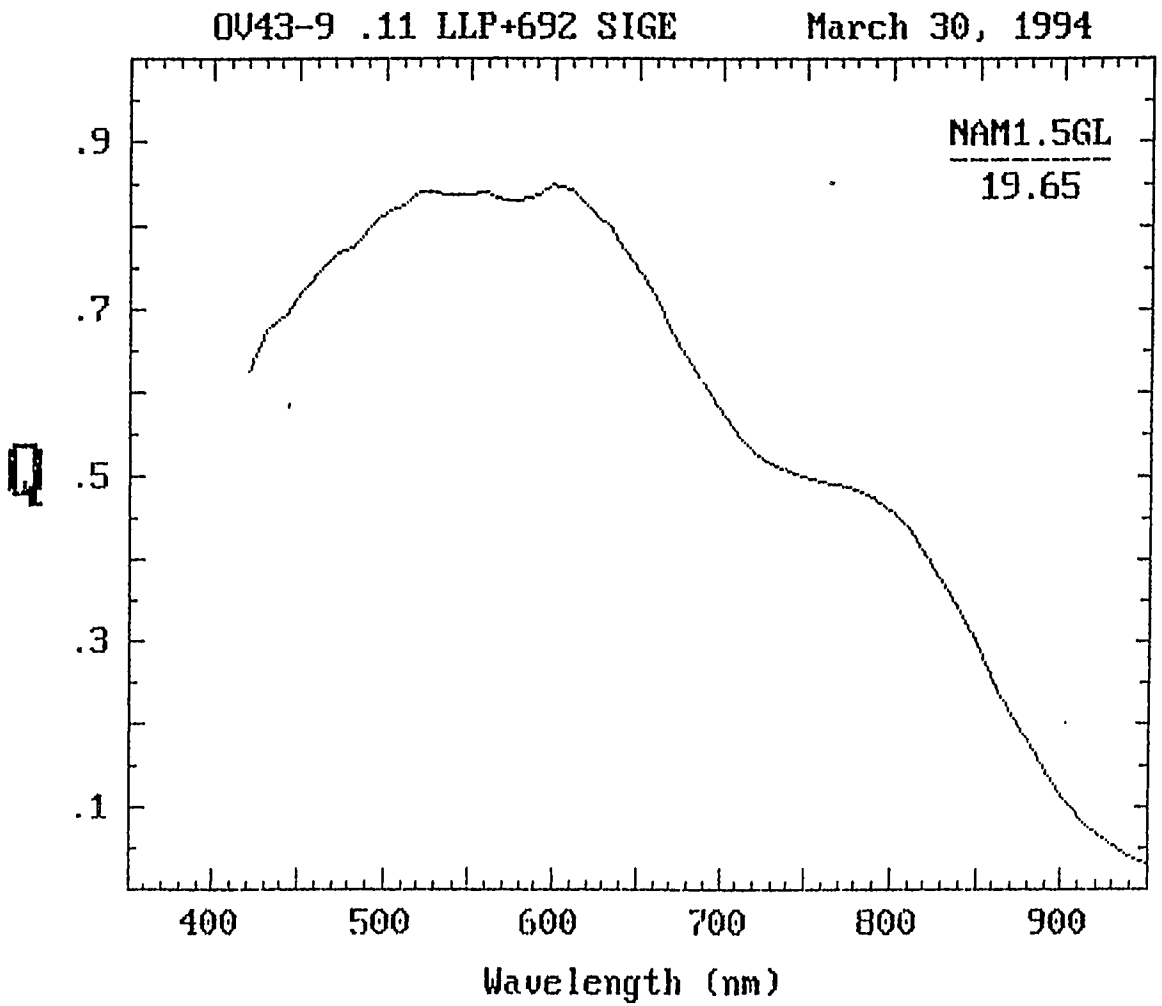

Figure 18: QE curve of a narrow band-gap a-Si-Ge solar cell showing QE=45% at 800 nm.

Task 8: Optimization of the Stable Efficiency of Photovoltaic Modules

Up-to-Date Progress Made in the Module Stable Efficiency Improvement under PVMaT 2A Program

During Phase I of the ongoing PV MaT 2A Program, we carried out the PV manufacturing technology development using ECD's 2 MW continuous roll-to-roll manufacturing line, designed and constructed by ECD.

In the following, we briefly describe the up-to-date achievement we have made using the 2 MW manufacturing line. We have optimized the deposition of triple-junction solar cells in the production machine at a speed of 1 ft/min. The optimization was focused on improving:

- the intrinsic layer quality
- the p layer
- the interfaces between p-i
- tunnel junction between p-n
- the current matching

After process optimization, we have achieved a-Si/a-Si/a-SiGe triple-junction two band-gap solar cells with 11.1% initial efficiency. Figure 19 shows the J-V curve of an 11.1% solar cell produced in a 700 m long production run. Figure 20 is the QE curve of this solar cell.

Besides high solar cell efficiency, another important aspect for a manufacturing process is the production yield. We evaluate the production yield using a standard QA/QC process. Figure 21 is a three dimensional plot of 1176 QA/QC test cells made on 42 samples evenly taken out of a 700 m production run. The uniformity, both along the web and across the web, are excellent. Out of 1176 cells, three are shunted or shorted. Therefore, the subcell yield is 99.7% for this production run.

Using these high efficiency solar cells, we assembled 4 ft^2 PV modules using ECD's module assembly process described earlier. Figure 22 is the I-V curve of a 4 ft^2 triple-junction a-Si alloy PV module produced in ECD's continuous roll-to-roll manufacturing line, measured by NREL using a Spire 240A simulator. The 9.5% initial module efficiency is the highest for any large-size (4 ft^2) a-Si alloy PV module produced in a production line.

We have light soaked these 4 ft^2 modules under NREL specified standard light soaking conditions. After 600 hours of one sun light soaking at approximately 50°C under load, the efficiency of these 4 ft^2 modules have stabilized to 8%. Figure 23 is the I-V curve of a 4 ft^2 module after 600 hours of light soaking.

We have further light soaked these modules to test the long term stability. Figure 24 shows the I-V curve of a module after 2380 hours of light soaking. No further degradation, within measurement accuracy, is found for these modules after prolonged light soaking.

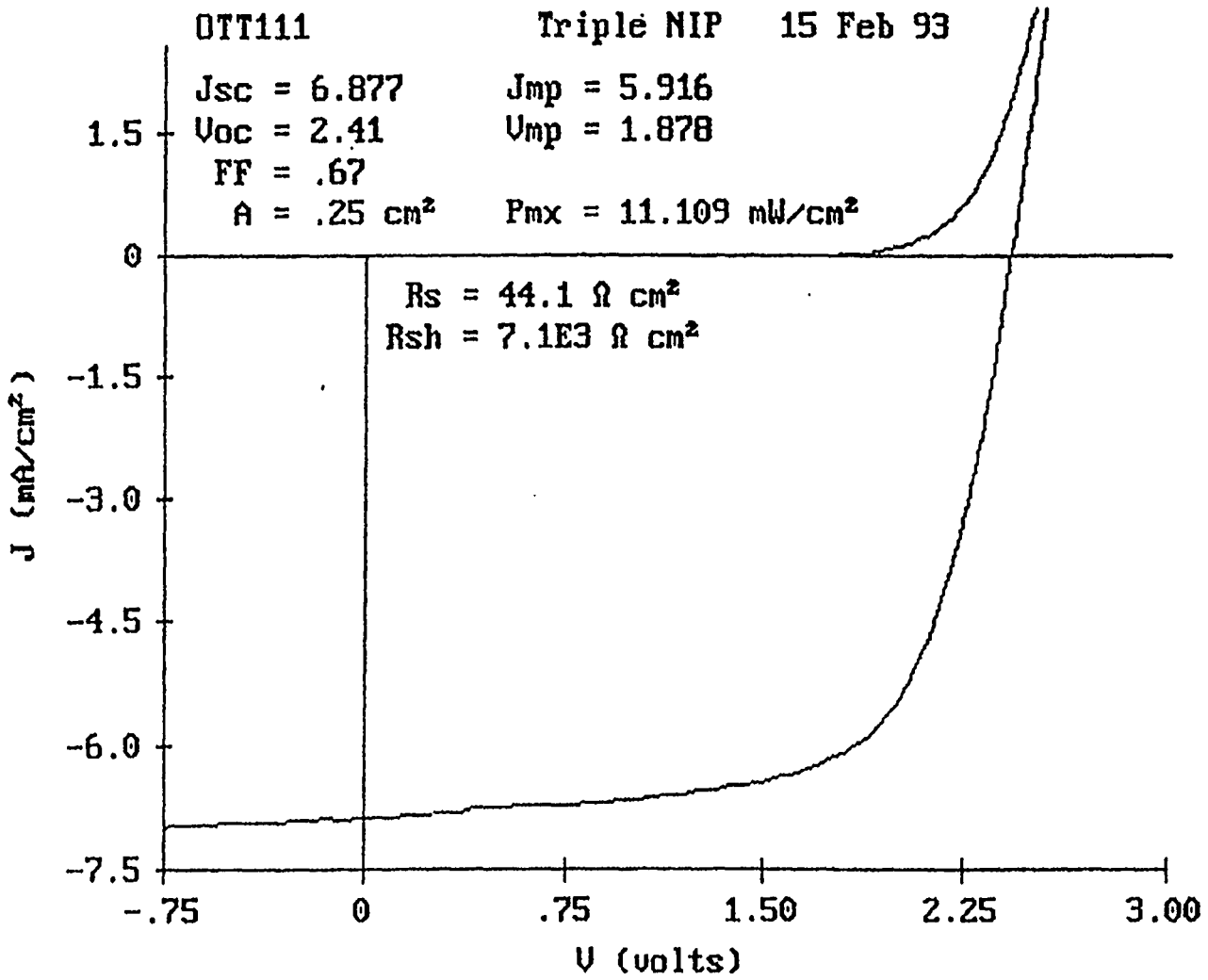

Figure 19: J-V curve of a 0.25cm^2 triple-junction cell showing 11.1% efficiency.

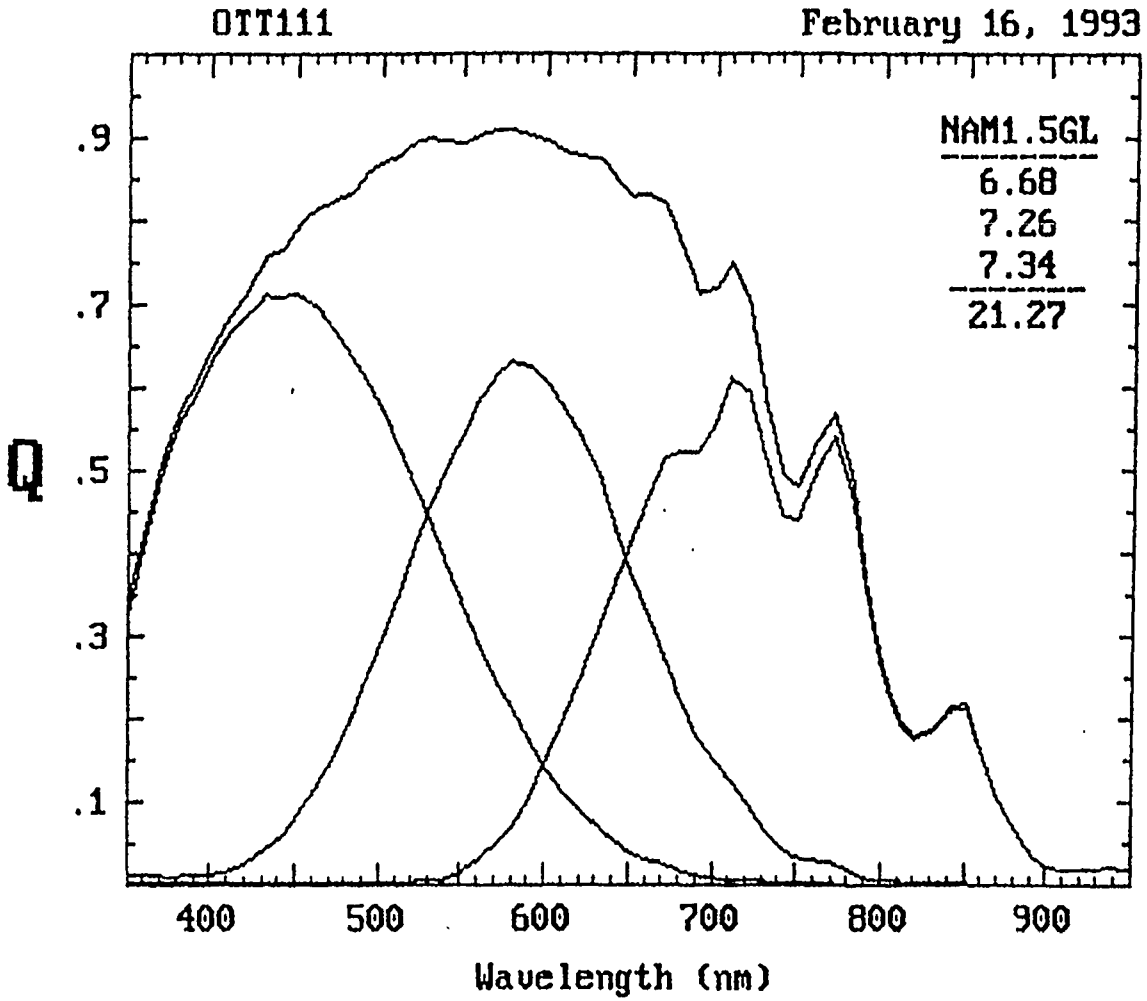

Figure 20: QE curve for the 0.25cm^2 triple-junction cell showing 11.1% efficiency.

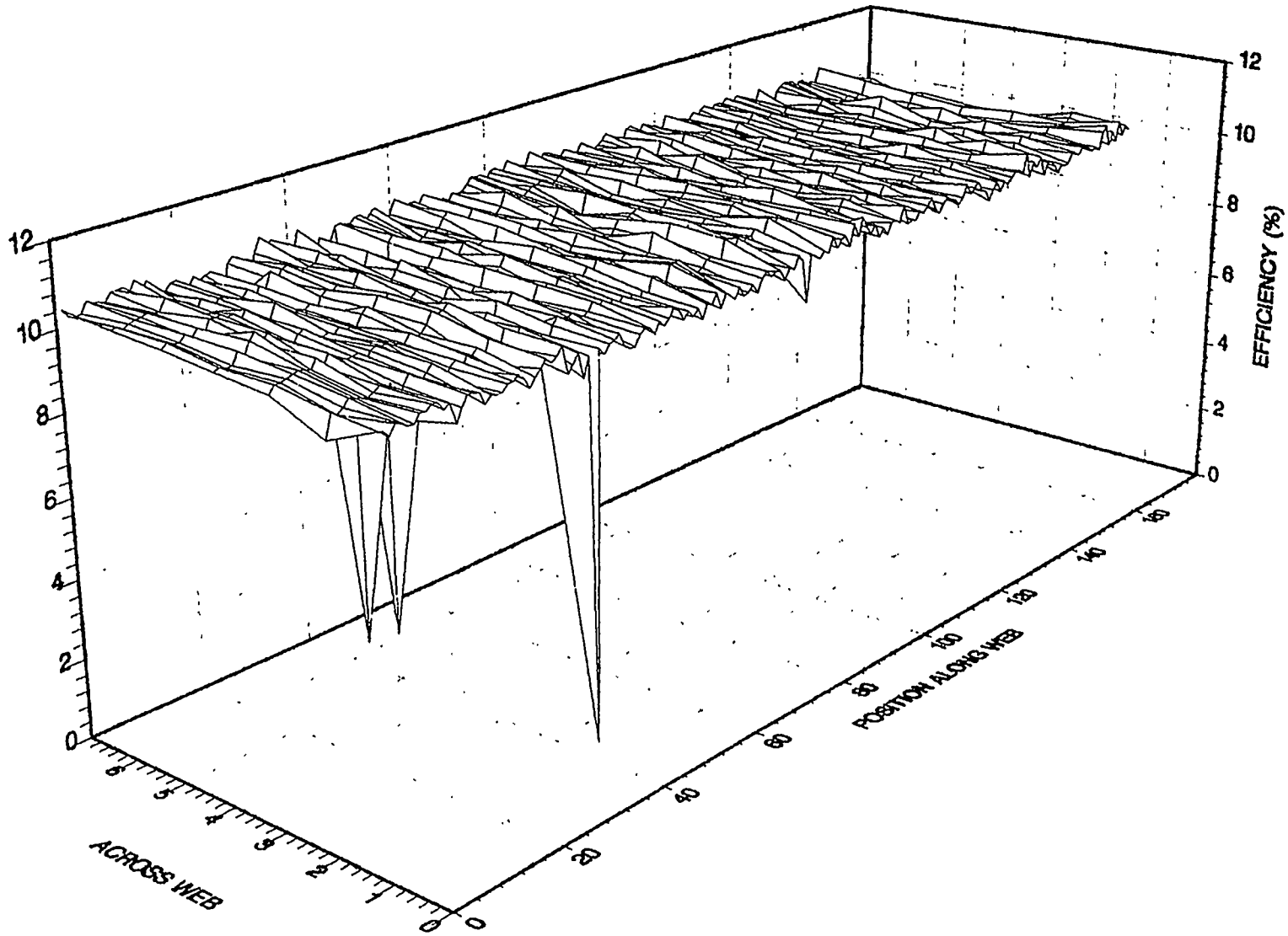

Figure 21: Cell efficiency of a 600 m production run.

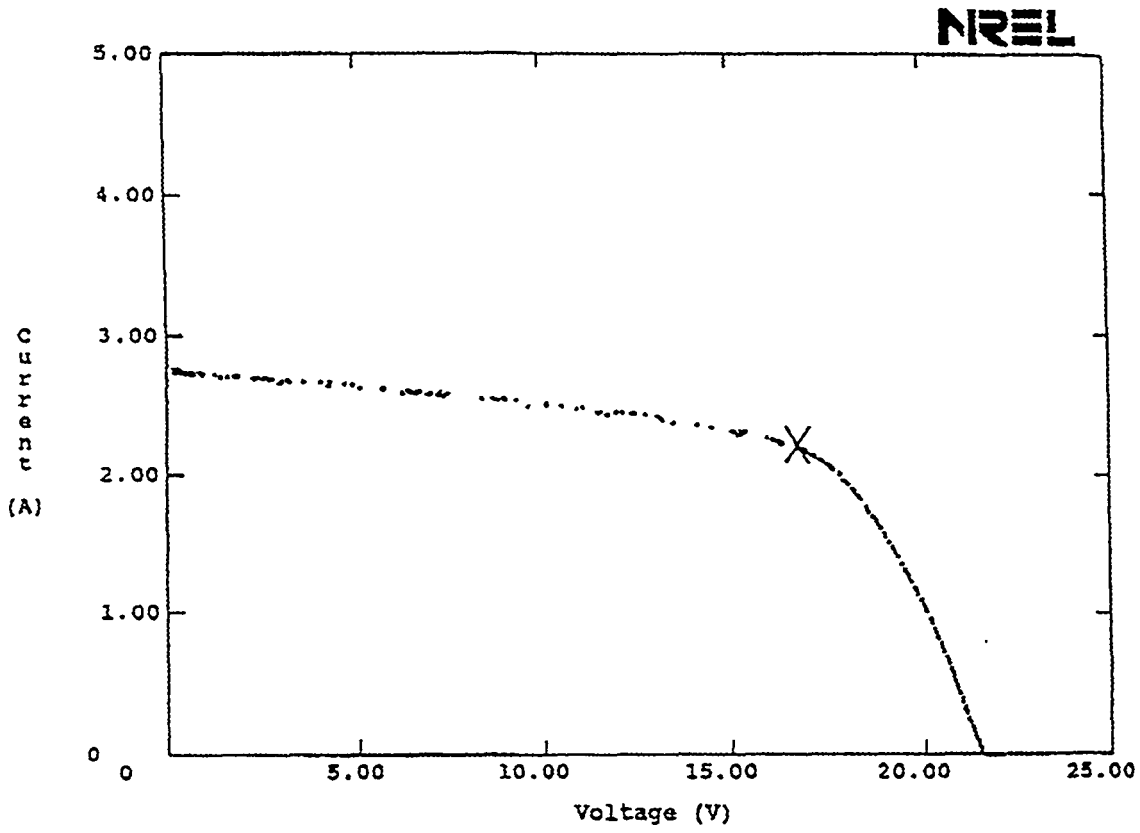

Manufacturer: ECD
Sample Type : a-Si/a-Si/a-Si module
Sample # : 030

Test Date : April 29, 1993
Test Time : 5:51 PM
Spectrum : ASTM E892 Global
File Name : C:\IV\data\IV4162.xy
NREL Spire 240A solar simulator (peak)
Estimated total uncertainty in efficiency is ± 5 %

Total irradiance = 1000 W/m^2
Temperature = 25 °C
Aperature Area = 3906 cm^2

Voc	= 21.51 V
Isc	= 2.743 A
Pmax	= 37.01 W
V at Pmax	= 16.72 V
I at Pmax	= 2.214 A
Fill Factor	= 62.7 %
Efficiency	= 9.47 %

Figure 22: I-V curve of a 4 ft^2 triple-junction a-Si alloy PV module, measured by NREL, showing 9.5% initial module efficiency.

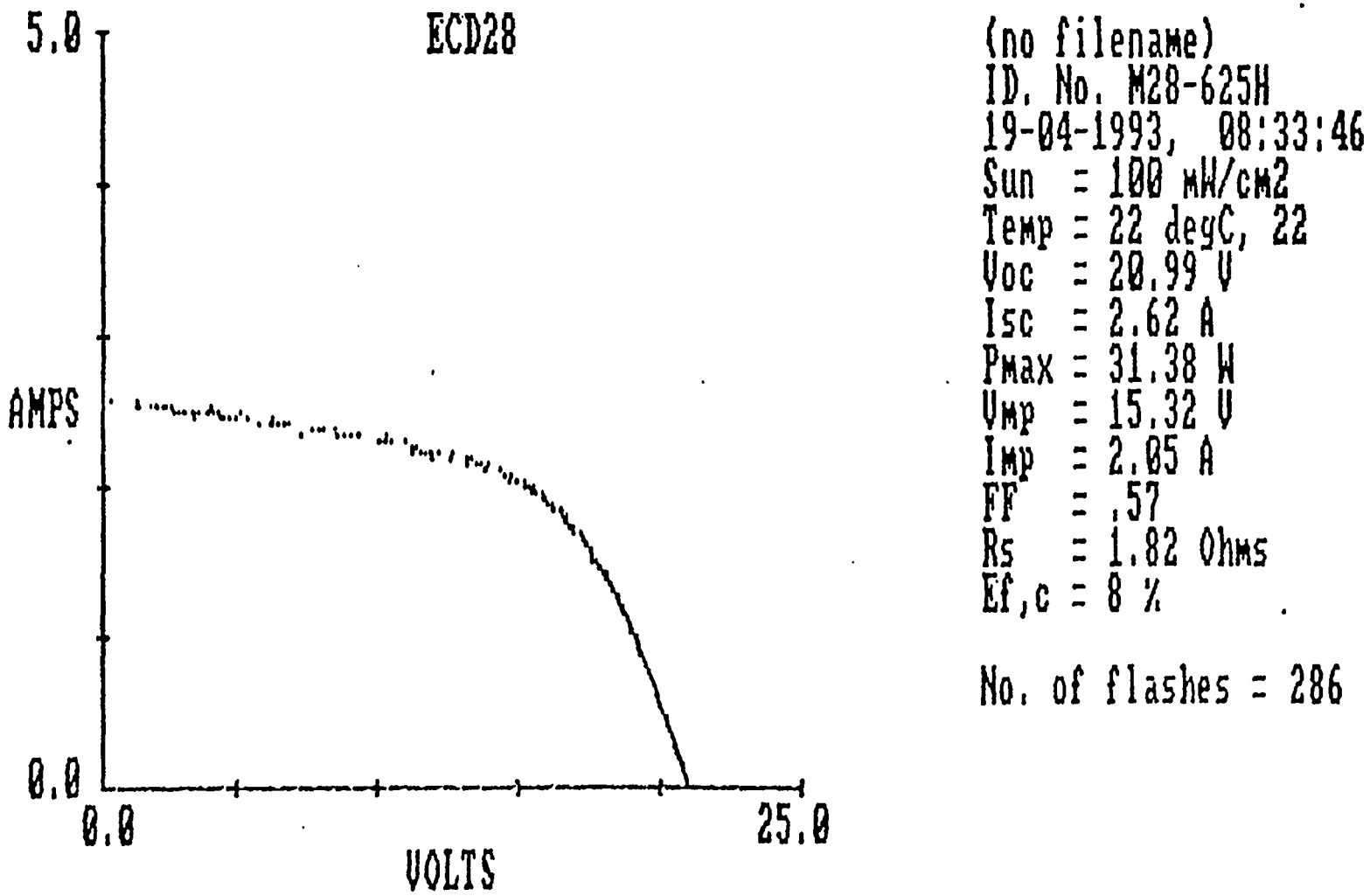

Figure 23: I-V curve of a 4 ft^2 a-Si alloy PV module showing 8% stable module efficiency.

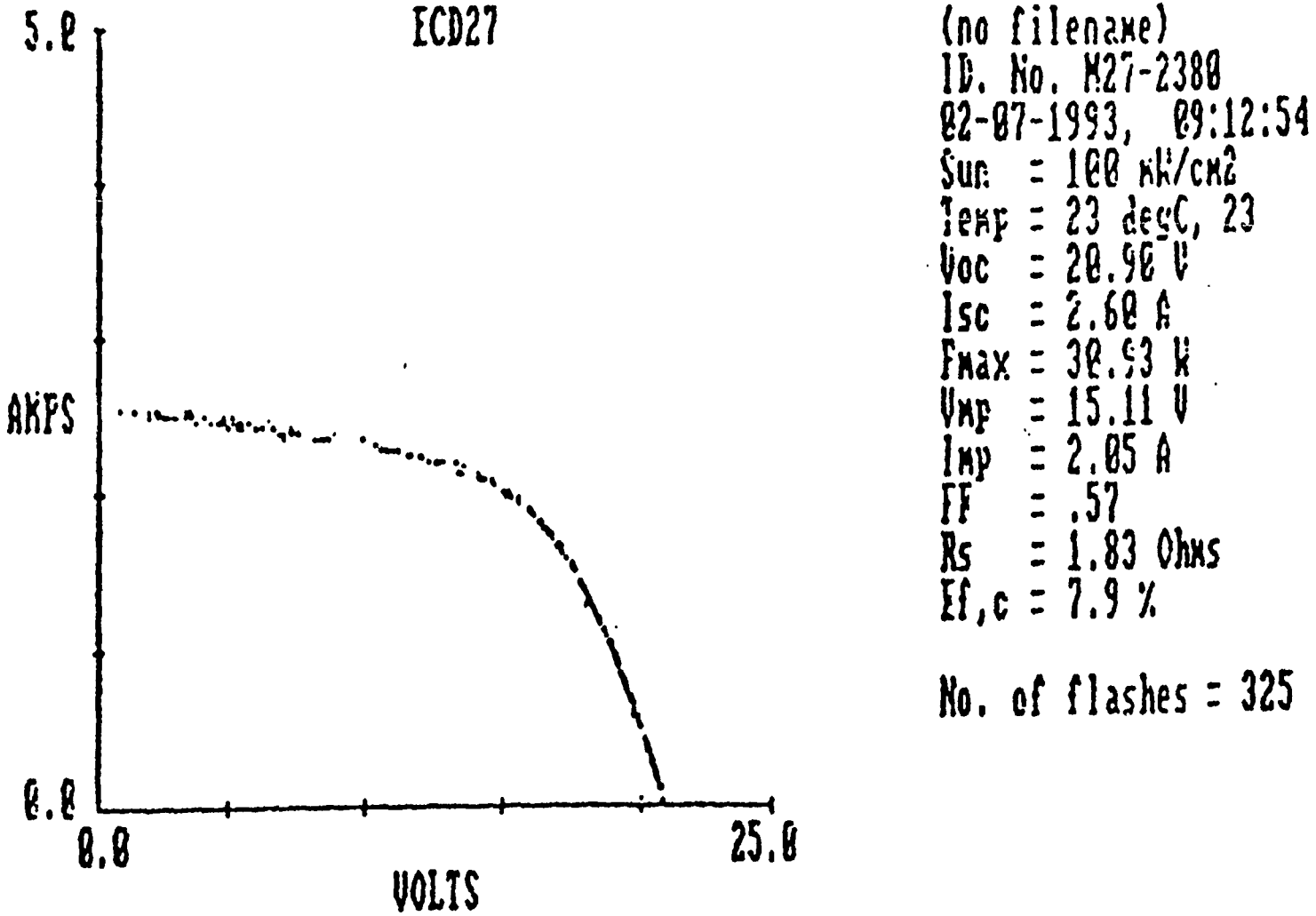

Figure 24 I-V curve of ECD's 4 ft² a-Si alloy PV module after 2380 hours of light soaking.

In Table 12, we list the performance of ECD's 4 ft^2 modules produced under this PVMaT 2A program, measured at ECD and NREL. The measurement is consistent between the two labs. In Figure 25, we illustrate progress in module efficiency with time.

Current Research Effort Toward Further Improving the Stable Module Efficiency

In order to incorporate new R&D advances and to further improve the stable module efficiency, we designed and constructed, at ECD's expense, a new multi-purpose continuous roll-to-roll a-Si alloy solar cell deposition machine having 200 kW per year capacity. This new machine, after being optimized, is expected to produce 10.2% stable PV modules.

As shown in Figure 1 and Figure 2, the new continuous roll-to-roll multi-purpose deposition machine consists of seven chambers:

1) Two chambers at both ends for the web loading and unloading, and for web driving and steering systems which can transport the web in both directions during deposition.

2) N, I, and P RF plasma CVD chambers for the deposition of n, i and p a-Si alloy layers needed for a single-junction solar cell. A triple-junction solar cell is made with web passing through the machine three times.

3) A single loop serpentine web deposition chamber for depositing intrinsic a-Si layer in a serpentine configuration. n and p chambers are also used for the deposition of n-(serpentine i)-p solar cell.

4) A DC magnetron sputtering chamber for the deposition of Ag/ZnO back-reflector layers and top conductor layer.

This multi-purpose deposition machine is capable of producing complete triple-junction solar cells in a sequential continuous roll-to-roll operation.

We have carried out preliminary process optimization of the machine to produce high efficiency a-Si alloy solar cells. Figure 26(a) is the J-V curve of a single-junction a-Si solar cell produced in the new machine on bare stainless steel. Figure 26(b) is the J-V curves of this cell under blue and red light. The V_{oc} and FF's are high, compared to the a-Si solar cell produced in our 2 MW roll-to-roll machine, as shown in Figure 27(a) and Figure 27(b). The improved FF indicates the improved intrinsic material quality. This solar cell, shown in Figure 26(a) is to be used as the top component cell of a-Si/a-SiGe/a-SiGe triple-junction solar cell. The J-V characteristics of the bottom and middle cells were shown previously in Figure 16 and Figure 17.

A set of PV modules produced in ECD's continuous-roll-to-roll manufacturing line is under qualification testing according to NREL's "Interim Qualification Tests and Procedures for Terrestrial Photovoltaic Thin-Film Flat-Plate Modules." Except for some cosmetic microdelamination, these modules have passed the specified 20 humidity-freeze cycling test and 200 thermal cycling tests.

Table 12: Module performance data of ECD's 4 ft^2 modules in the initial and stable states measured at ECD and NREL.

Module Number	Date Produced	Light Soaking Time (hrs)	Voc (V)	Isc (mA/cm^2)	FF	Pmax (W)	Area (cm^2)	Efficiency (%)	Measurement Lab
#01	Jul.92	Initial	21.75	2.51	0.59	32.39	3991	8.12	ECD
		Initial	21.83	2.525	0.596	32.84	3984	8.24	NREL
#12	Sep.92	Initial	21.76	2.59	0.6	33.81	3991	8.47	ECD
		Initial	21.79	2.61	0.602	34.21	3997	8.56	NREL
#16	Nov.92	Initial	21.27	2.57	0.62	33.93	3945	8.6	ECD
		Initial	21.49	2.72	0.592	34.61	3949	8.76	NREL
#23	Mar.93	Initial	21.62	2.68	0.628	36.39	3907	9.31	ECD
		Initial	21.56	2.72	0.63	36.96	3906	9.46	NREL
#27	Mar.93	Initial	21.6	2.72	0.632	37.18	3923	9.48	ECD
		2380	20.9	2.60	0.57	30.93	3923	7.9	ECD
		2380	21.0	2.56	0.566	30.42	3903	7.8	ECD
		2380	20.87	2.534	0.57	30.17	3903	7.73	NREL
#28	Mar.93	Initial	21.3	2.75	0.634	37.15	3923	9.47	ECD
		625	20.99	2.62	0.57	31.38	3923	8.0	ECD
		625	20.87	2.57	0.571	30.64	3906	7.84	NREL
#30	Mar.93	Initial	21.61	2.68	0.63	36.57	3907	9.36	ECD
		Initial	21.51	2.74	0.627	37.01	3906	9.47	NREL

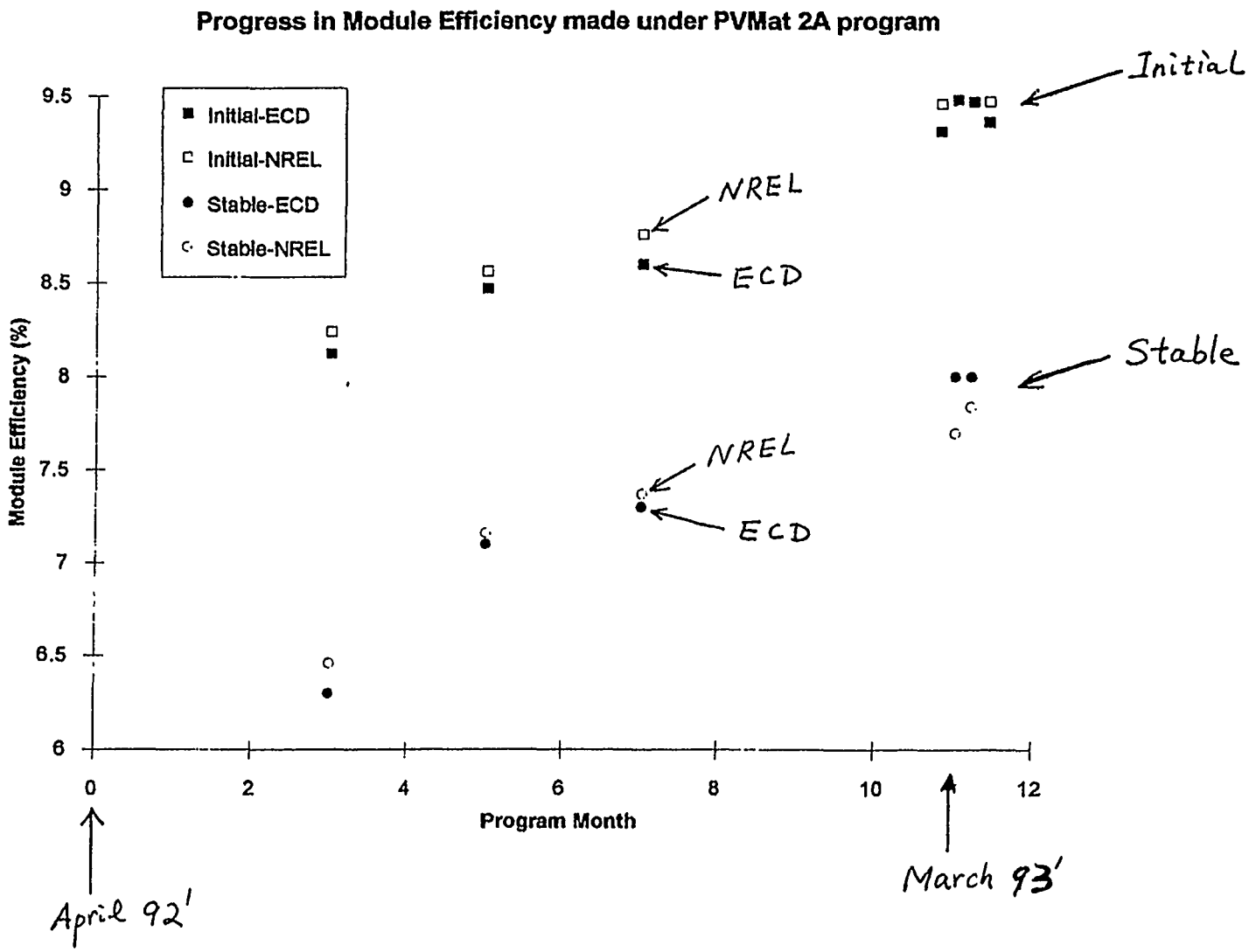

Figure 25 Progress in initial and stable efficiencies for ECD's 4 ft² PV production modules produced under the PV MaT 2A program, measured at ECD and NREL.

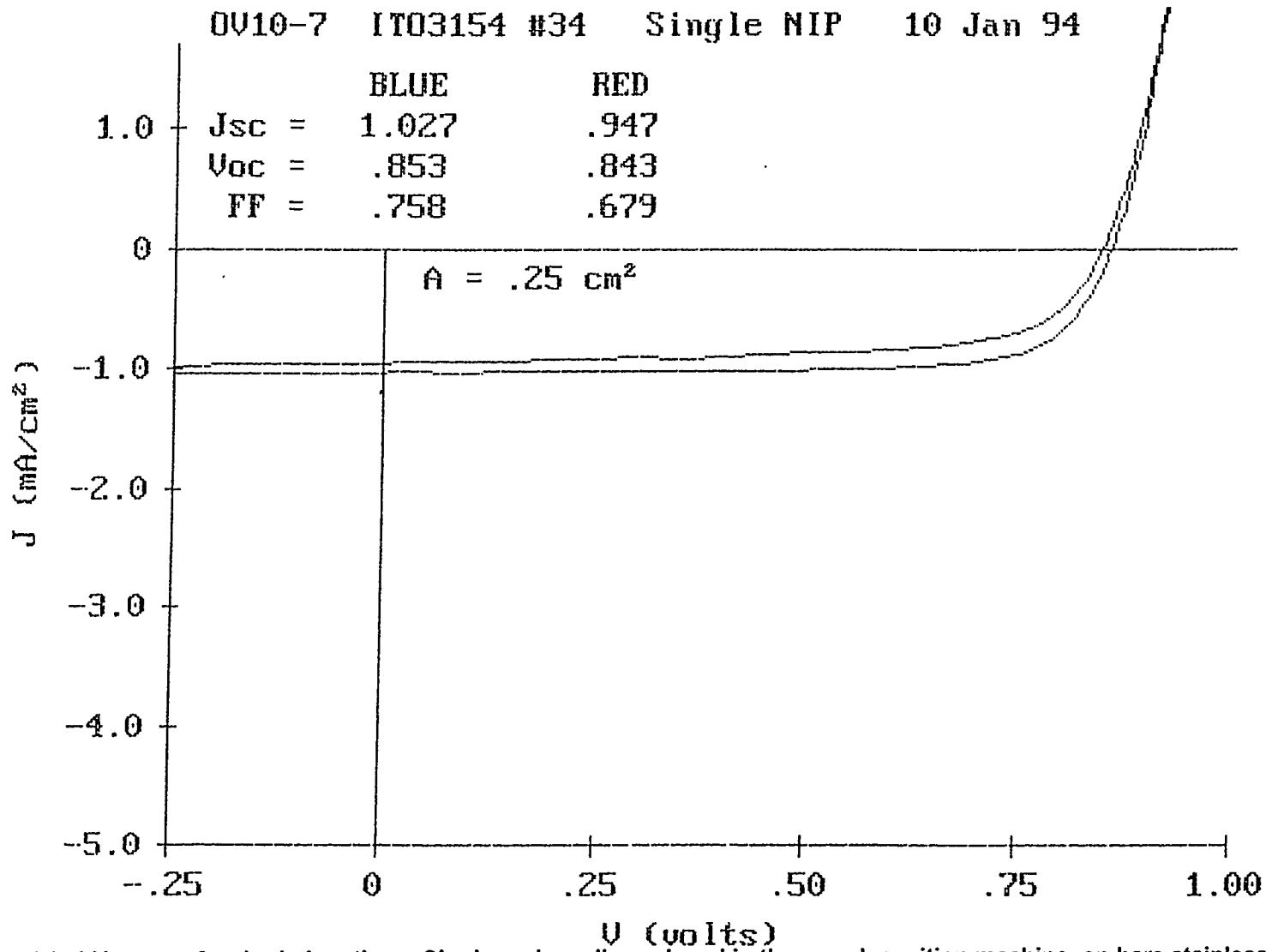

Figure 26(a) J-V curve of a single-junction a-Si n-i-p solar cell, produced in the new deposition machine, on bare stainless steel.

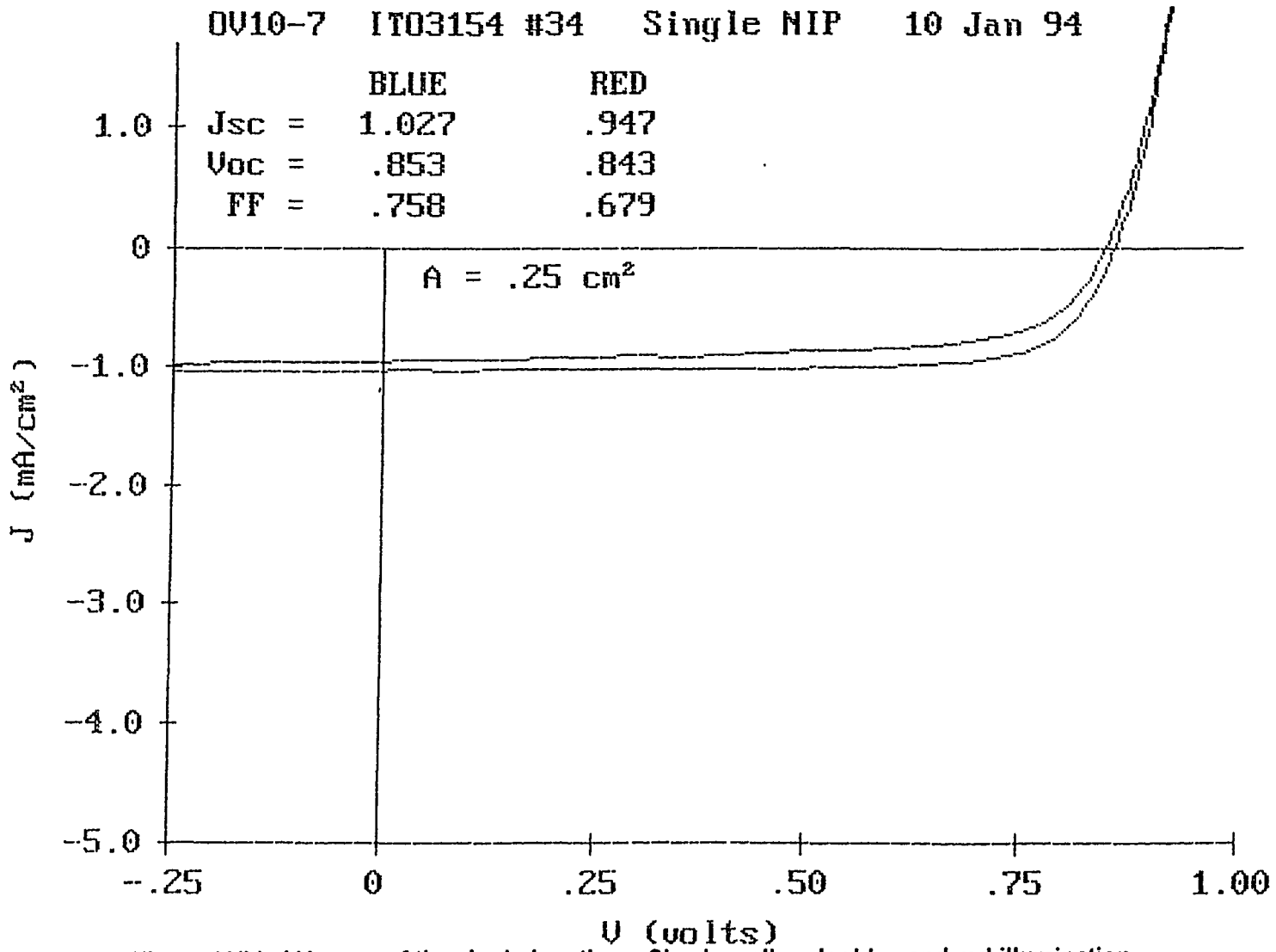

Figure 26(b) J-V curve of the single-junction a-Si solar cell under blue and red illumination.

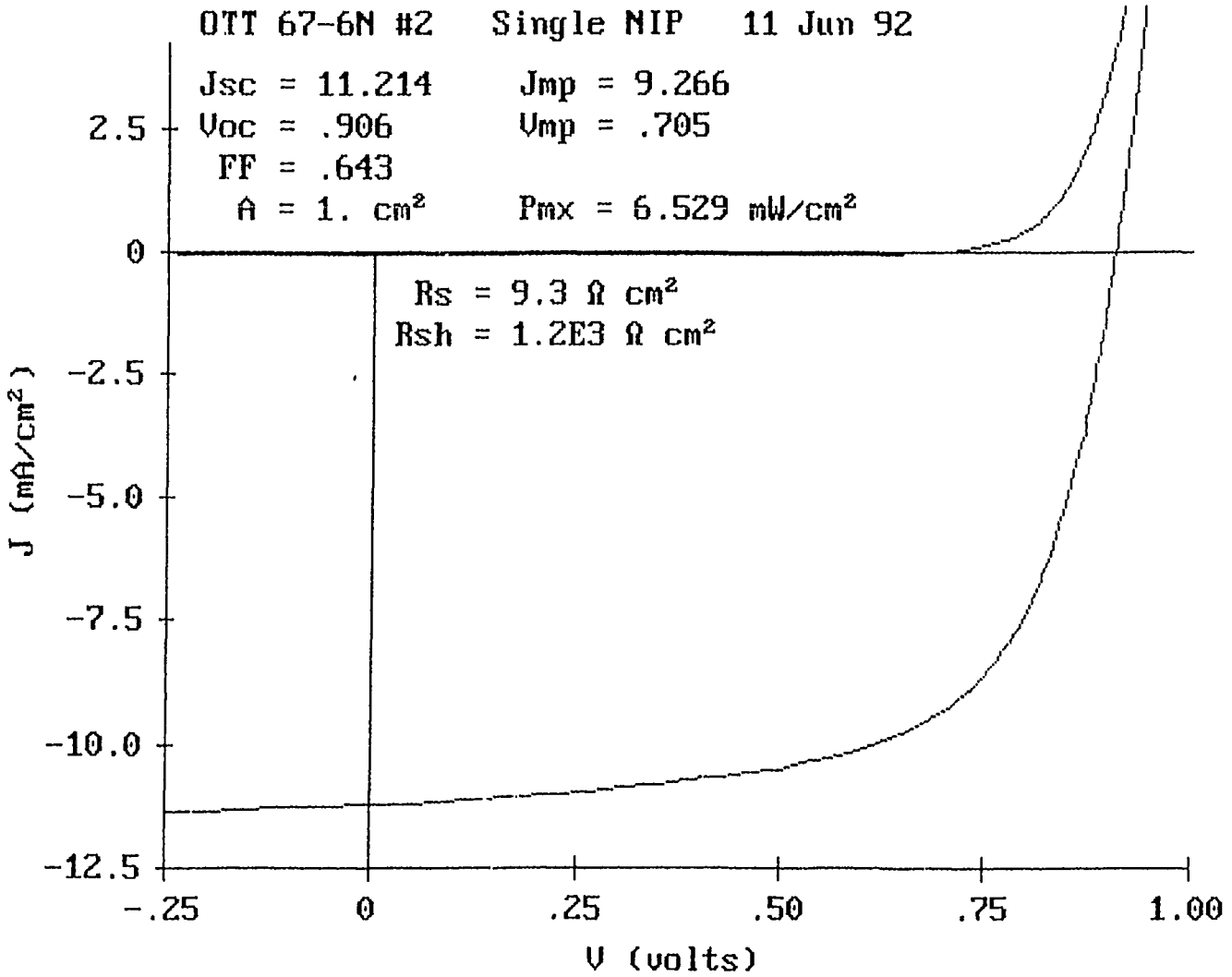

Figure 27(a) J-V curve of an a-Si n-i-p solar cell, produced in the previous 2 MW production machine, on bare stainless steel.

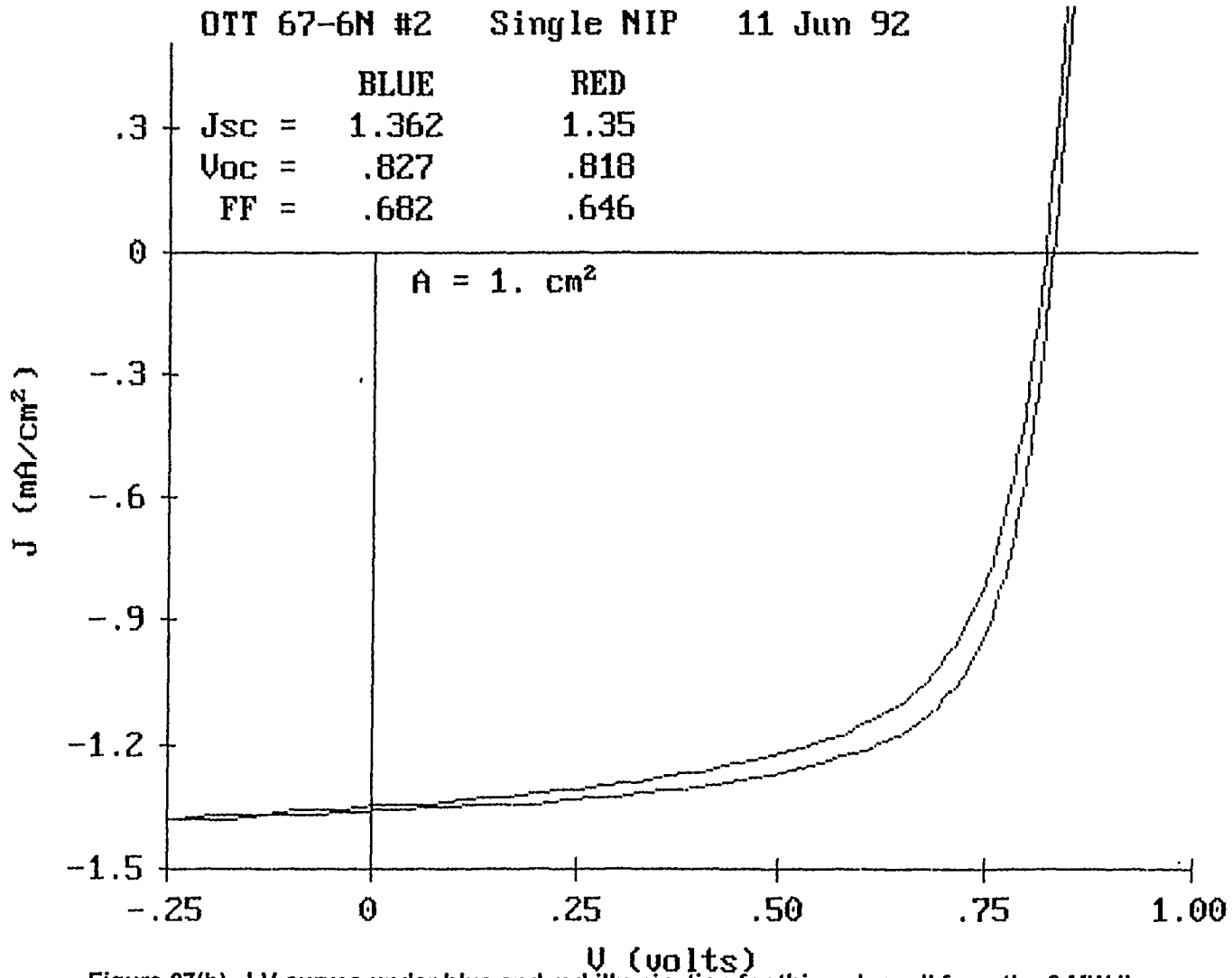

Figure 27(b) J-V curves under blue and red illumination for this solar cell from the 2 MW line.

We have developed a new grid/bus bar technique to reduce the optical loss, utilizing thin copper wires adhered to ITO surface with conductive adhesive. Figure 28 shows the sketches of the existing and new grid designs. The detailed analysis summarized in Table 13 indicates that approximately 3% ~ 4% gain in efficiency is expected for the new design. Figure 29(a) and Figure 29(b) shows the J-V curve for a sub-cell with new wire grids. Compared with the same cell using previous screen printed Ag paste grid lines the fill factor is improved to 0.67 and the series resistance is reduced to 39 Ω cm^2.

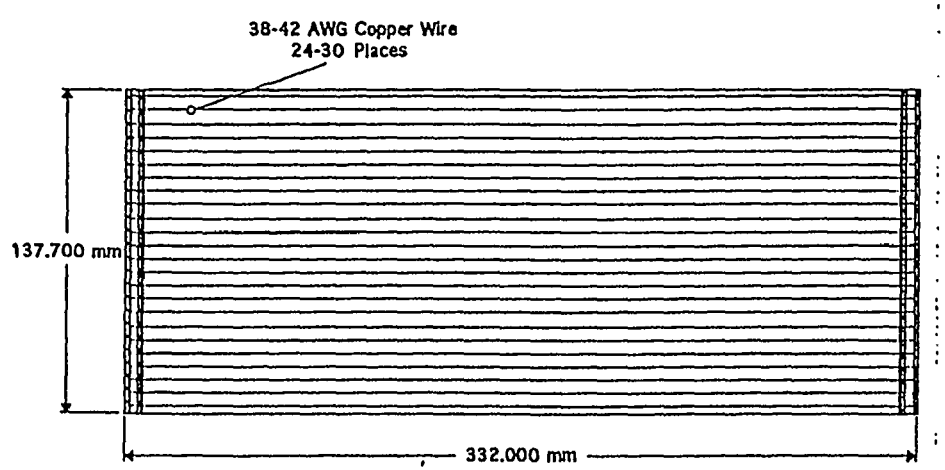

STRIP WITH NEW WIREGRID

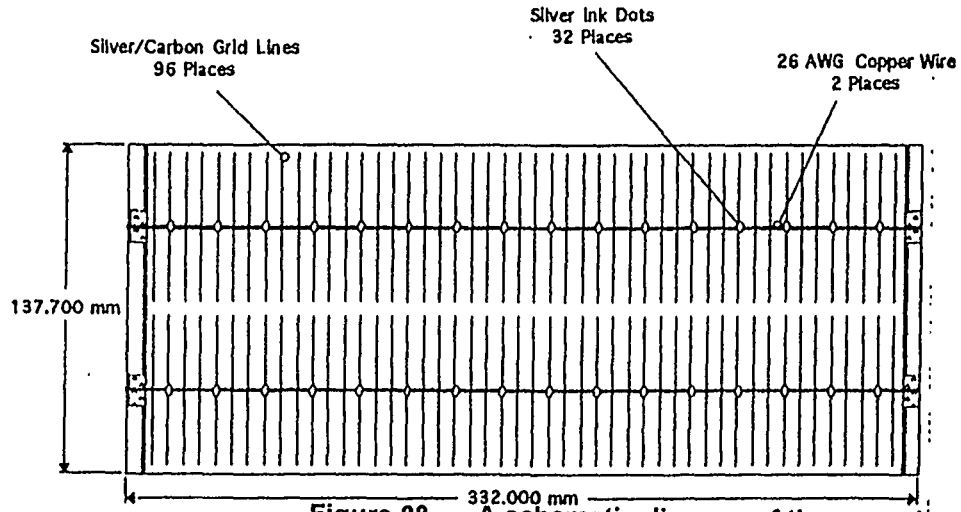

STRIP WITH PRESENT SILVER/CARBON PASTE GRID AND WIRE BUS BARS

Figure 28 A schematic diagram of the new wire grid design.

Table 13: Grid/busbar/encapsulation losses, current vs new.

Current Module Design	New Wire Grid Design
1 Module = 9 strips	1 Module = 9 strips
2 Wire bus bars per strip	36 Grid Wires per strip
Wire Bus Bars are connected on both sides	Grid Wires are connected on both sides

	Current Module Design		New Wire Grid Design
	Theoretical	Real	Theoretical
Grid Width	0.2 mm	0.28 mm	0.076 mm
Bus Bar Width	0.4 mm	0.50 mm	N/A
ITO Width	0.64 mm	0.64 cm	0.31 cm
Length of Grid	3.3 cm	3.1 cm	33.2 cm
Width of Intra-Strip Etch Line	0	0	0
Width of Inter-Strip Etch Line	0.75 mm	0.55 mm	0.75 mm
Estimated Losses			
ITO Electrical Loss	1.0%	1%	0.73%
Grid Electrical Loss	0.59%	2.3%	0.52%
Grid Shadow Loss	2.98%	3.8%	2.00%
Silver & Wire Bus Shadow	0.59%	0.74%	N/A
Etch Loss (Coverage)	0.99%	1%	1%
Protruding Pads	1.0%	0.37%	N/A
Main Bus Bar Electrical	0.19%	0.19%	N/A
Encapsulation	4%	3%	4%
Subcell Mismatch	1%	1%	1%
Total	12.34%	13.4%	9.25%

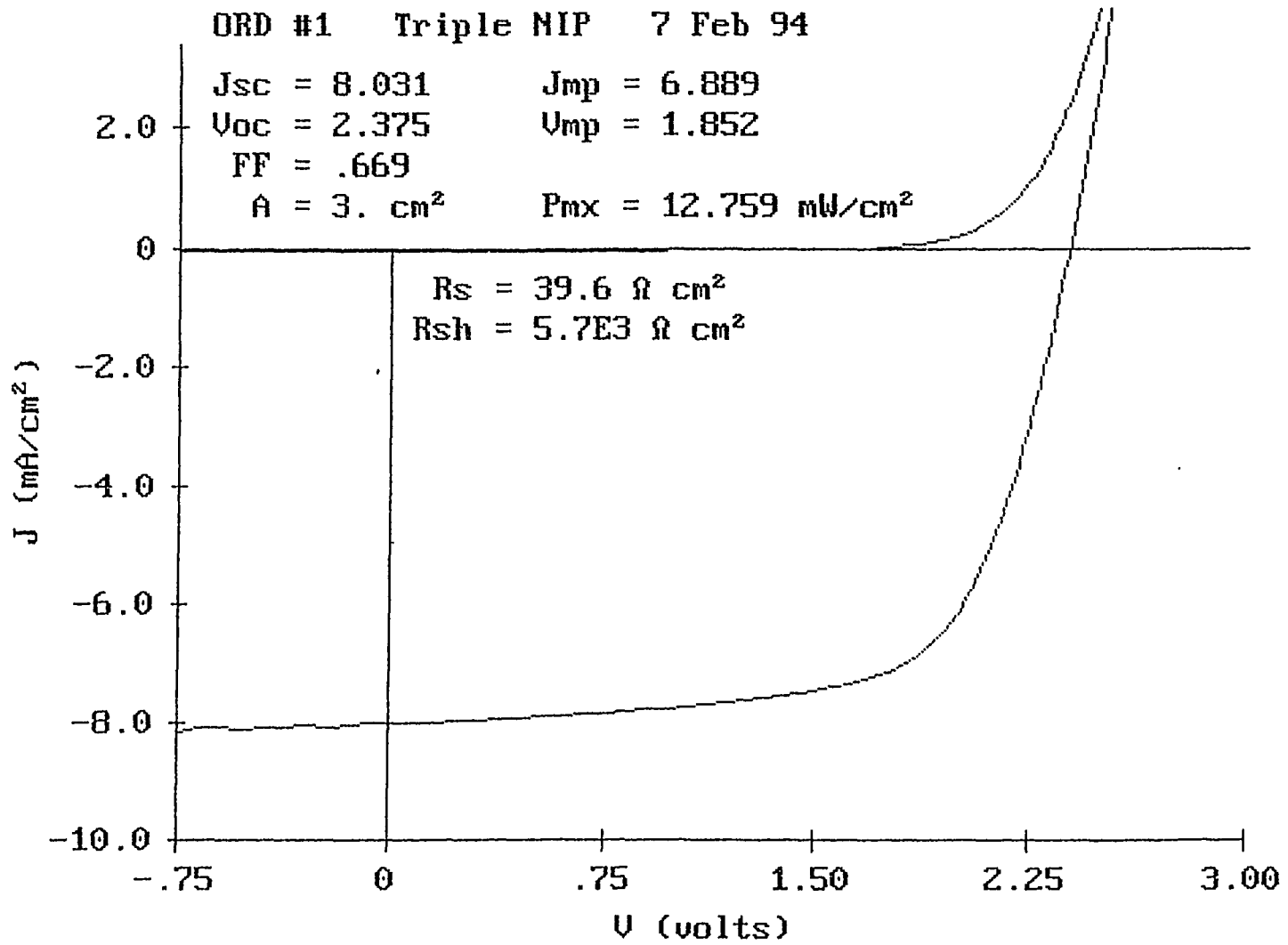

Figure 29(a) J-V curve for a solar cell with new wire grid.

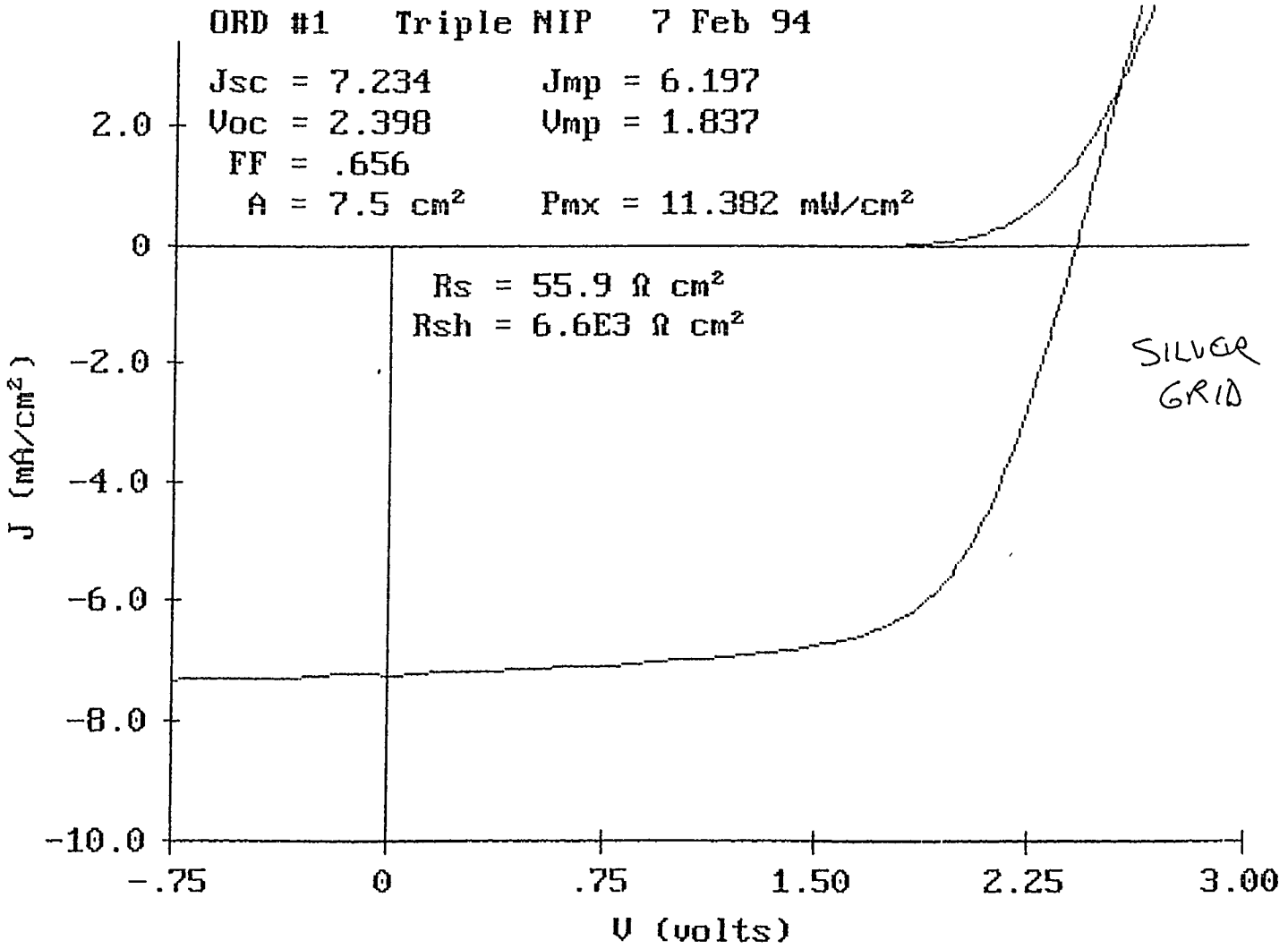

Figure 29(b) J-V curve for a similar solar cell with previous Ag paste grid, as a comparison.

Task 9: Demonstration of Serpentine Web Continuous Roll-to-Roll Deposition Technology

A serpentine web configuration has been extensively used in other film processing industries such as the steel industry and photographic film manufacturing to achieve a high throughput for manufacturing processes which require a long reaction time. We have developed a design concept for a serpentine web continuous roll-to-roll amorphous silicon alloy solar cell deposition process to maximize solar cell throughput while keeping the size of individual deposition chambers small.

A schematic diagram for an RF plasma processor for depositing n-i-p/n-i-p/n-i-p amorphous silicon alloy solar cells utilizing a serpentine web roll-to-roll process is shown in Figure 30.

As can be seen in the diagram, deposition takes place on the substrate as it travels vertically through the deposition chamber. This is to be contrasted to the current process in which the substrate travels horizontally. This vertical, roller-guided travel creates a large deposition area using less floor space. In the deposition chamber, a single RF cathode generates a plasma which will produce film deposition on regions of substrate facing both sides of the cathode. Because of the compactness of the serpentine design, substantial cost savings for the equipment will be achieved. In addition, because of the compact design of the serpentine system, heat loss will be substantially reduced, which will give rise to reduced electric power consumption. Furthermore, by utilizing a perforated cathode or other open cathode configurations in which the surface area is minimized, the gas utilization will be improved as deposition on the cathode is reduced. Cathode heating and dark-space shields are eliminated in the serpentine design which simplifies the internal design.

Due to the slow rate of deposition which can be used without reducing throughput, a-Si alloy intrinsic materials can be deposited with a minimum density of microvoids[23] in the serpentine roll-to-roll process. We expect that the current 15-18% degradation will be reduced to less than 8%.

In summary, we anticipate that with the serpentine web roll-to-roll technology, high efficiency stable PV modules can be produced in a high volume production process. A substantial reduction of manufacturing cost will be the consequence of the cost reduction of capital equipment, facilities, gases, energy and factory space.

The benefits of the serpentine design are summarized below:

- Maximized throughput for a high volume production plant
- Reduced machine cost
- Improved gas utilization
- Reduced power consumption.
- Improved material stability by maintaining low deposition rate

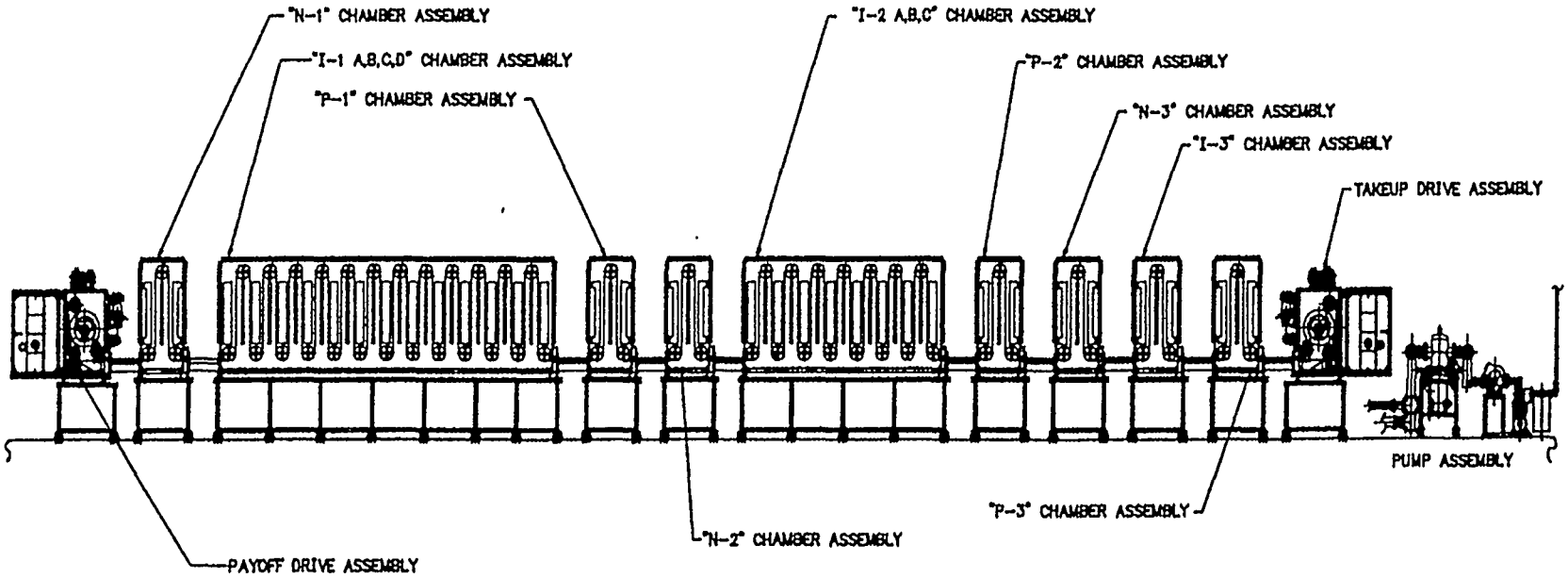

Figure 30: Serpentine web continuous roll-to-roll concept design for triple-junction a-Si solar cell deposition machine.

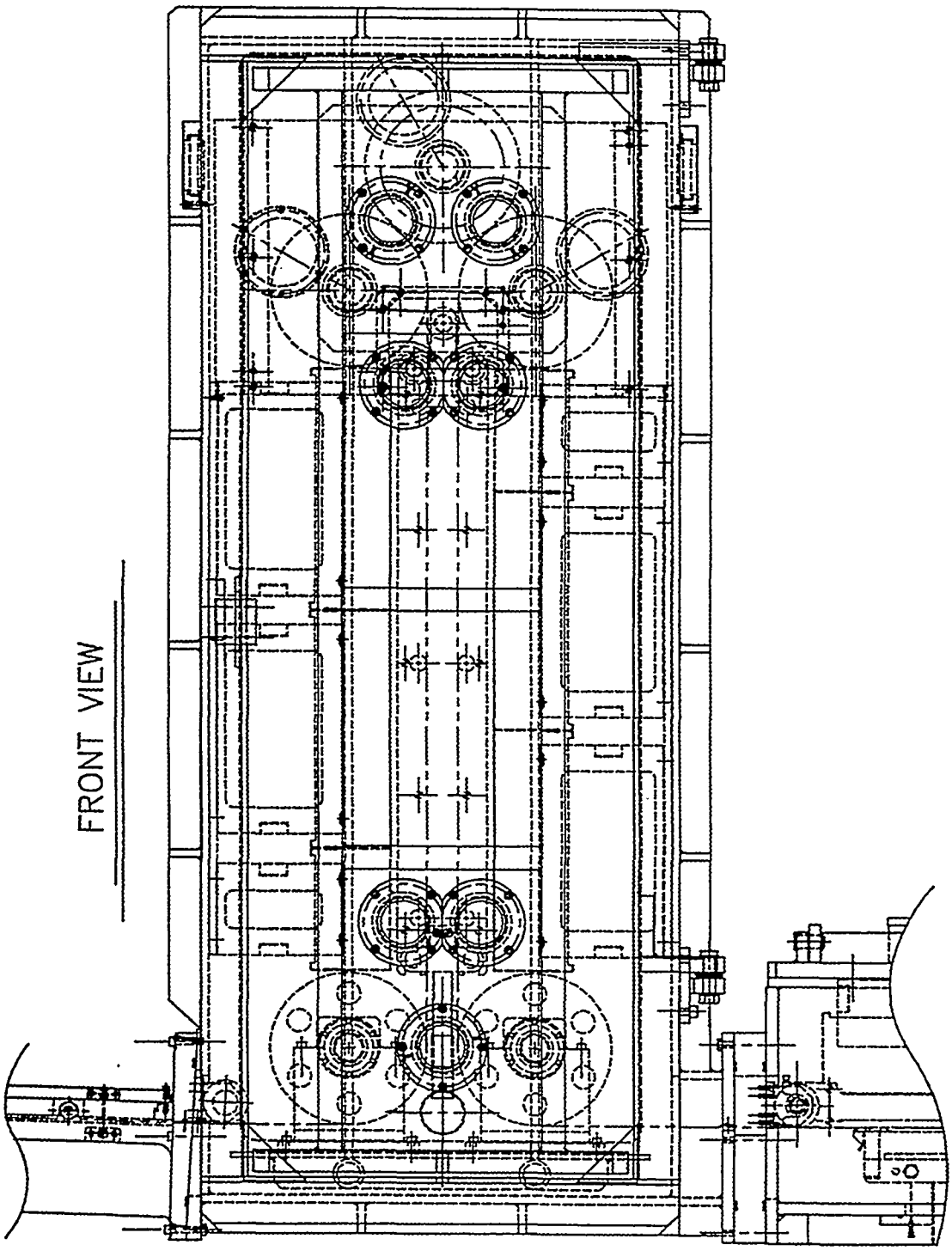

Figure 31: Single loop serpentine web continuous roll-to-roll deposition chamber.

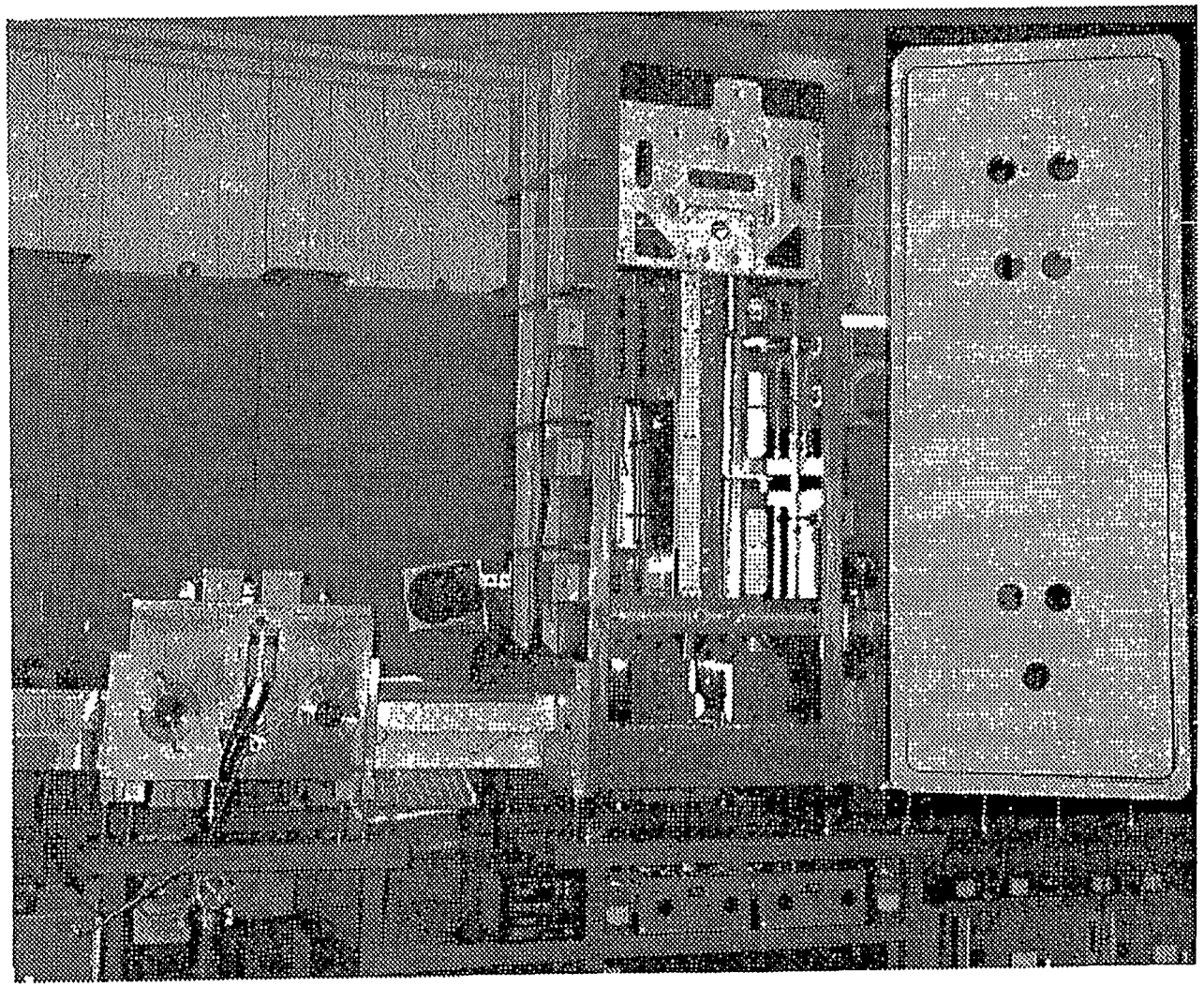

Figure 32: Picture of the serpentine web continuous roll-to-roll deposition chamber.

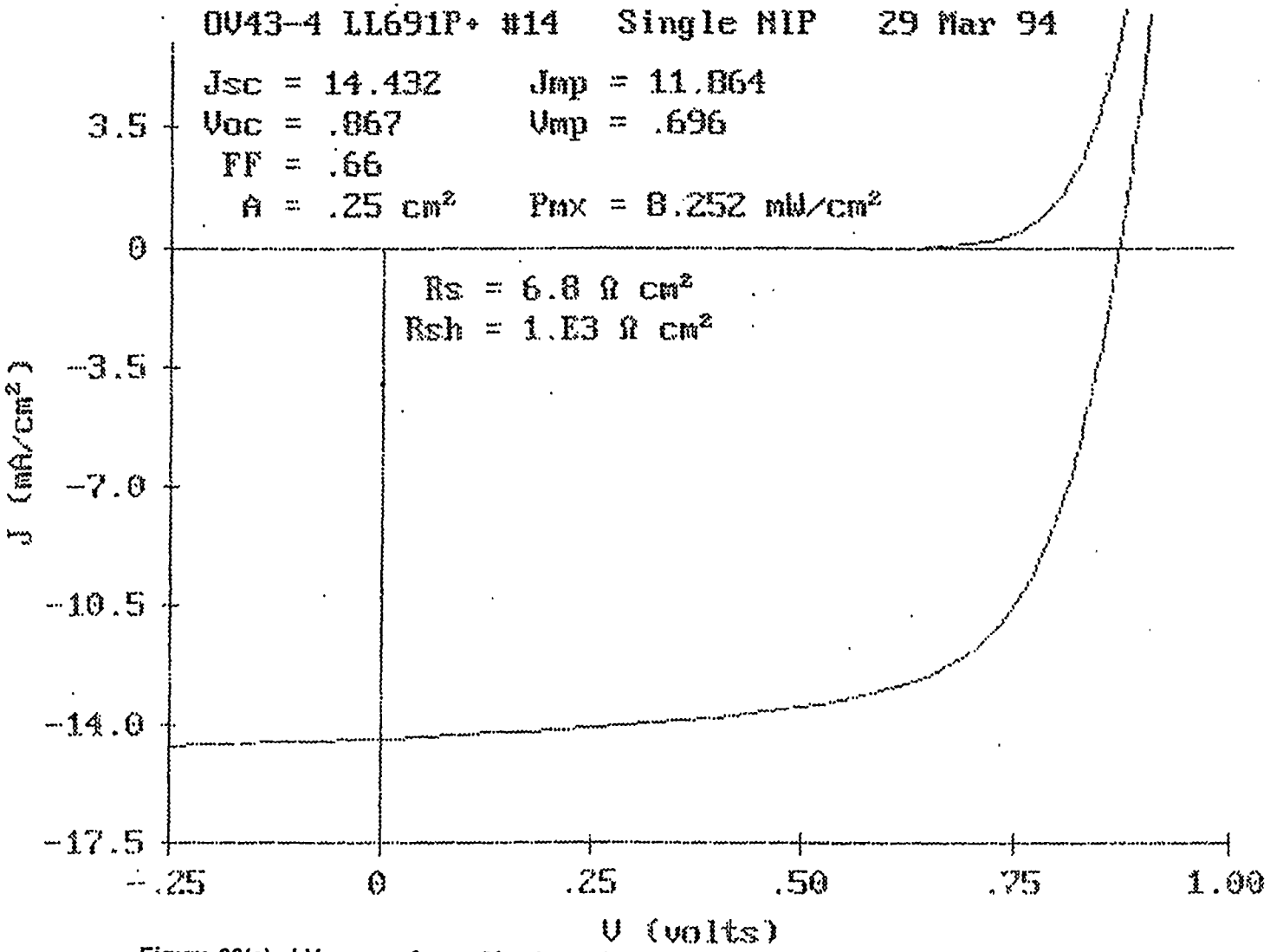

Figure 33(a) J-V curve of an a-Si solar cell with i layer made in the serpentine chamber.

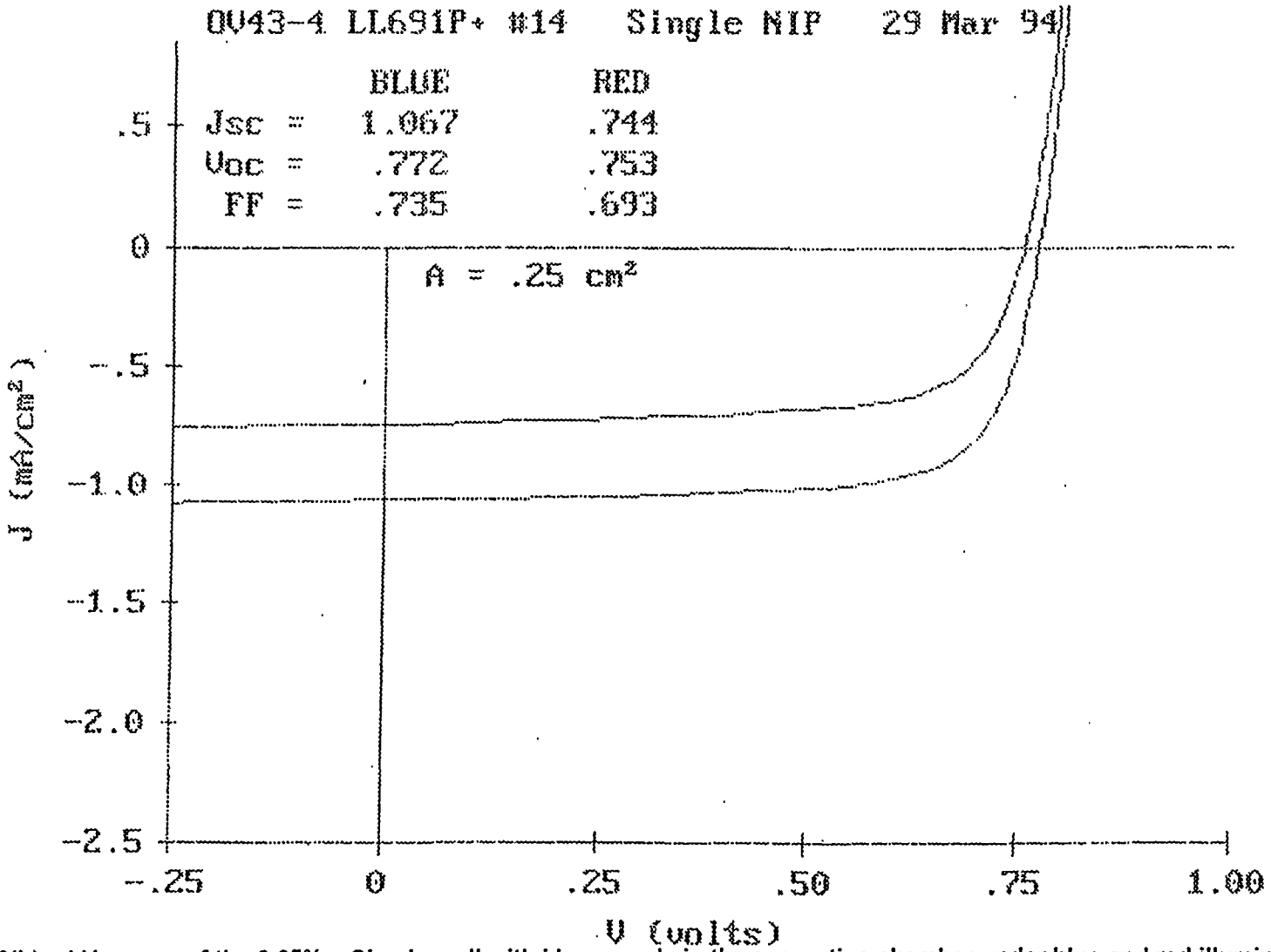

Figure 33(b): J-V curves of the 8.25% a-Si solar cell with i layer made in the serpentine chamber under blue and red illumination.

In this program period, detailed engineering and design of a single-loop serpentine web continuous roll-to-roll deposition chamber have been completed. Figure 31 shows the drawing of the design. Figure 32 is a picture of the serpentine chamber in the deposition machine.

The chamber is 81" high and 35" wide. It allows for a single loop of web 143" long. Two deposition zones, approximately 32" long, have been incorporated. One deposition zone coats the web as it moves vertically upward and one zone coats the web as it moves downward past the same cathode. A gas manifold spanning the 14" wide web is placed at the top of the cathode and gas is pumped through a manifold at the bottom. A preheat zone is located before the upward and downward pass of the web across the cathode to insure proper web temperature during deposition.

This chamber has been incorporated into the continuous roll-to-roll multi-purpose deposition machine. a-Si n-i-p solar cells, with the intrinsic a-Si layer deposited in the serpentine chamber have been produced. Figure 33(a) is the J-V curve of such a test solar cell, showing 8.3% initial efficiency. Figure 33(b) is the J-V curves of this solar cell under blue and red illumination. The 8.3% initial efficiency from a preliminary test solar cell has indicated the effectiveness of the basic serpentine machine design.

We have also studied the uniformity of the film deposited inside the serpentine chamber. From the deposition on stainless steel web while the web was held still inside the chamber during deposition, we concluded that the deposition uniformity is as good as that from the horizontal chambers. Further more, no film peeling or other mechanical failure was observed in the serpentine films from the preliminary deposition runs.

Task 10: Material Cost Reductions

Under Task 10, we continue to focus our efforts in two major high material-cost areas:

1. Reduction of germane and disilane costs

2. Reduction of module assembly material costs

One of the highest cost items in the bill of materials for ECD's triple-junction multiple band-gap a-Si alloy solar cell, which consists of a-Si/a-Si/a-SiGe structure, is germane and disilane. In Phase I, we identified Mitsui Toatsu and Voltaic as the world's largest manufacturers of disilane and germane gases, respectively, and obtained germane and disilane gases at prices which are substantially lower than we previously paid on the world market. We also worked with our Russian joint venture partner, Sovlux, to obtain lower cost gases from Russia. In Phase I, we obtained test quantities of disilane and germane gases produced in Russia. The results of purity analyses of these gases indicated that germane had acceptable purity, whereas disilane had unacceptably high levels of impurities. During this program period, the Russian supplier completed a germane production line and produced 10 kg of germane.

As the result of process optimization to reduce the layer thickness and to improve gas utilization, 77% material cost reduction for germane and 58% reduction for disilane have been achieved during Phase I.

In this program period, we designed a serpentine web continuous roll-to-roll deposition chamber in order to further improve gas utilization and to reduce the cost for gases. It is expected that approximately 40% reduction will be achieved by this approach.

A new, low-cost module design to reduce assembly material cost has been developed in Phase I.

The new design utilized a marine plywood panel to eliminate the aluminum frame and steel backing plate. The resultant cost reduction will be approximately 30%. The marine plywood module has been tested under thermal cycles and humidity/freeze cycles. However, the module exhibited a warping problem due to the warpage of the unframed plywood backing. In order to eliminate the warping problem, a new marine plywood design has been developed. The improved design uses improved wooden frames to eliminate the warping, as is shown in Figure 34.

The new grid/bus-bar design, described previously, reduces the grid/bus-bar material cost by approximately 50% by eliminating costly silver paste.

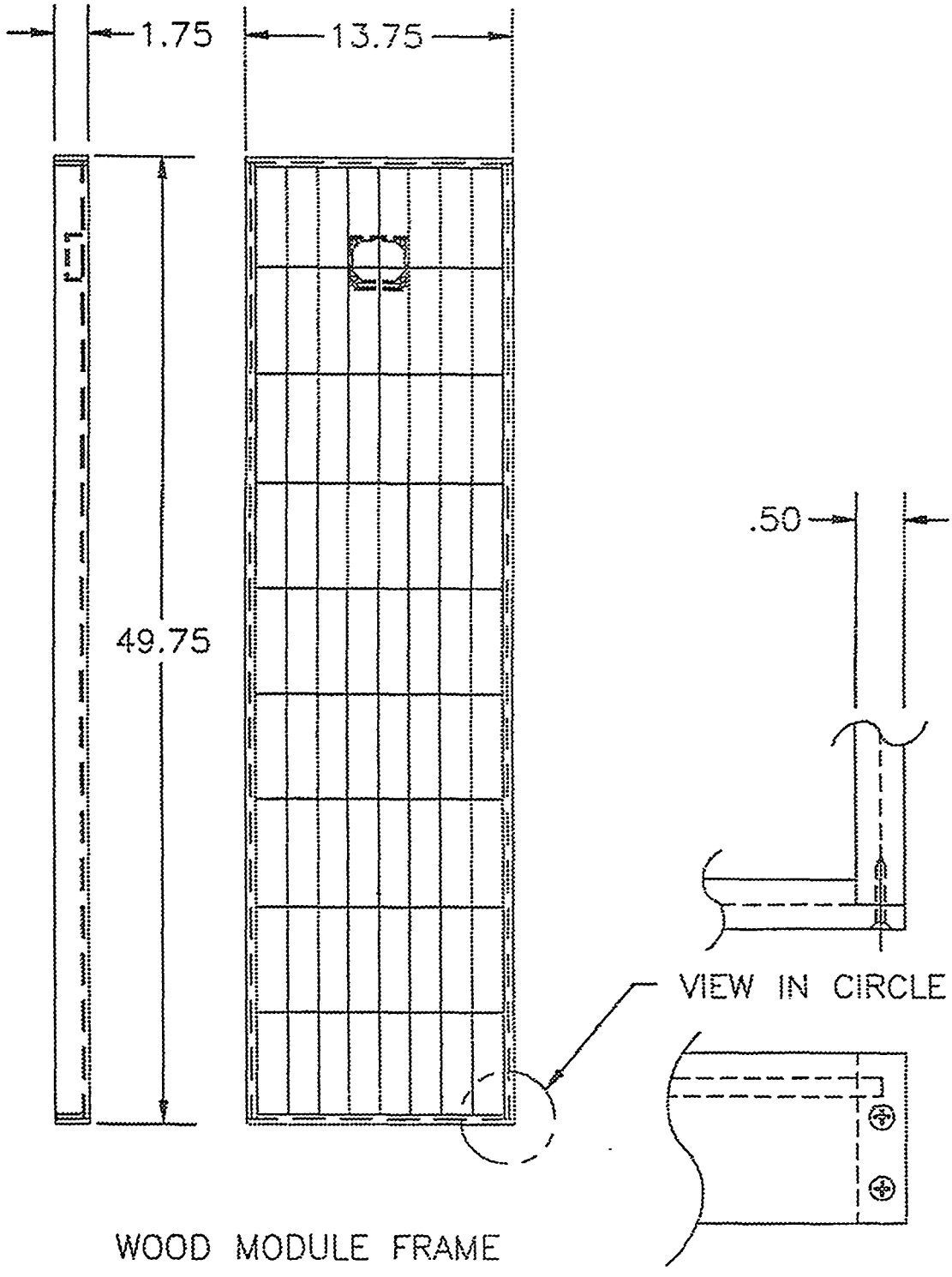

Figure 34: Marine plywood module.

References

1 Production of Tandem Amorphous silicon Alloy Cells in a Continuous Roll-to-Roll Process, M. Izu and S. R. Ovshinsky, SPIE Proc. 407, 42 (1983).

2 Roll-to-Roll Plasma Deposition Machine for the Production of Tandem Amorphous Silicon Alloy Solar Cells, M. Izu and S. R. Ovshinsky, Thin Solid Films 119, 55 (1984).

3 Amorphous Silicon Solar Cells Production in a Roll-to-Roll Plasma CVD Process, H. Morimoto and M. Izu, JARECT 16 (1984); Amorphous Semiconductor Technology & Devices, North Holland Publishing Company, Edited by Y. Hamakawa, 212 (1984).

4 Roll-to-Roll Mass Production Process for Amorphous Silicon Solar Cell Fabrication, S.R. Ovshinsky, Proc. International PVSEC-1, 577 (1988).

5 High Efficiency Multiple-Junction Solar Cells Using Amorphous Silicon and Amorphous Silicon-Germanium Alloys, J. Yang, R. Ross, T. Glatfelter, R. Mohr, G. Hammond, C. Bernotaitis, E. Chen, J. Burdick, M. Hopson and S. Guha, Proc. 20th IEEE P.V. Spec. Conf. 241 (1988).

6 Physics of High Efficiency Multiple-Junction Solar Cells, J. Yang, R. Ross, R. Mohr and J. P. Fournier, Proc. MRS Symp. Vol. 95, 517 (1987).

7 Performance of Large Area Amorphous Silicon Based Single and Multiple-Junction Solar Cells, P. Nath and M. Izu, Proc. of the 18th IEEE Photovoltaic Specialists Conf., Las Vegas, Nevada, 939 (1985).

8 1 MW Amorphous Silicon Thin-Film PV Manufacturing Plant, P. Nath, K. Hoffman, J. Call, C. Vogeli, M. Izu and S. R. Ovshinsky, Proc. of the 3rd International Photovoltaic Science and Engineering Conf., Tokyo, Japan, 395 (1987).

9 Conversion Process for Passivation Current Shunting Paths in Amorphous Silicon Alloy Solar Cells, P. Nath, K. Hoffman, C. Vogeli and S. R. Ovshinsky, Appl. Phys. Lett. 53 (11), 986 (1988).

10 Yield and Performance of Amorphous Silicon Based Solar Cells Using Roll-to-Roll Deposition, P. Nath, K. Hoffman, J. Call, G. Didio, C. Vogeli and S. R. Ovshinsky, Proc. 20th IEEE P.V. Spec. Conf., 293 (1988).

11 A New Inexpensive Thin Film Power Module, P. Nath, K. Hoffman, C. Vogeli, K. Whelan and S. R. Ovshinsky, Proc. 20th IEEE P.V. Spec. Conf., 1315 (1988).

12 Fabrication and Performance of Amorphous Silicon Based Tandem Photovoltaic Devices and Modules, P. Nath, K. Hoffman and S. R. Ovshinsky, 4th International P.V. Science and Engineering Conf., Sydney, Australia, (1989).

13 Advances in High-Efficiency, Multiple-Band-Gap, Multiple-Junction Amorphous Silicon Based Alloy Thin-Film Solar Cells, S. Guha, A Paper Presented at MRS Spring Meeting, San Diego, April (1989).

14 Amorphous Silicon-Germanium Alloy Solar Cells with Profiled Band-Gaps, J. Yang, R. Ross, T. Glatfelter, R. Mohr and S. Guha, MRS Symposium Proc. Vol. 149, 435 (1989).

15 Low-Pressure Microwave PECVD Technology, M. Izu, S. J. Hudgens, J. Doehler and B. Dotter, Proc. 4th International Conf. on Vacuum Web Coating, 129 (1990).

16 High Deposition Rate Amorphous Silicon Alloy Xerographic Photoreceptor, S. J. Hudgens and A. J. Johncock, Proc. MRS Symp. Vol. 49, 403 (1985).

17 Amorphous Semiconductors for Microelectronics, S. J. Hudgens, Proc. SPIE Vol. 617, 95 (1986).

18 Manufacturing of Triple-Junction 4 ft^2 a-Si Alloy PV Modules, M. Izu, X. Deng, A. Krisko, K. Whelan, R. Young, H.C. Ovshinsky, K.L. Narasimhan and S.R. Ovshinsky, proceedings of 23rd IEEE PV Specialist Conference, 919 (1993).

19 Continuous Roll-to-Roll amorphous silicon Photovoltaic Manufacturing Technology, M. Izu, S.R. Ovshinsky, X. Deng, A. Krisko, H.C. Ovshinsky, K.L. Narasimhan, and R. Young, A paper presented at 12th NREL PV Program Review Meeting, October, 1993.

20 Photothermal Deflection Spectroscopy and Detection, W.B. Jackson, N.M. Amer, A.C. Boccara and D. Fournier, Appl. Opt. 20, 1333, (1981).

21 U.S. Department of Energy news release, January 18, 1994.

22 Amorphous Silicon Alloy Photovoltaic Technology--From R&D to Production, S. Guha, J. Yang, A. Banerjee, T. Glatfelter, K. Hoffman, S. R. Ovshinsky, M. Izu, H. C. Ovshinsky and X. Deng, In Amorphous Silicon Technology Proceedings of MRS spring meeting, 1994.

23 Effect of Microvoids on Initial and Light-Degraded Efficiencies of Hydrogenated Amorphous Silicon Alloy Solar Cells, S. Guha, J. Yang, S. J. Jones, Y. Chen, and D. C. Williamson, Appl. Phys. Lett. 61, 1444. (1992)

REPORT DOCUMENTATION PAGE

Form Approved
OMB NO. 0704-0188

1 AGENCY USE ONLY (Leave blank)	2. REPORT DATE	3. REPORT TYPE AND DATES COVERED
	November 1994	Annual Subcontract Report, 8 April 1993-7 April 1994

4. TITLE AND SUBTITLE

Continuous Roll-to-Roll Amorphous-Silicon Photovoltaic Manufacturing Technology

5. FUNDING NUMBERS

C: ZM-2-11040-7

TA: PV550101

6. AUTHOR(S)

M. Izu

7. PERFORMING ORGANIZATION NAME(S) AND ADDRESS(ES)

Energy Conversion Devices, Inc.
1675 West Maple Road
Troy, Michigan 48084

8. PERFORMING ORGANIZATION REPORT NUMBER

9. SPONSORING/MONITORING AGENCY NAME(S) AND ADDRESS(ES)

National Renewable Energy Laboratory
1617 Cole Blvd.
Golden, CO 80401-3393

10. SPONSORING/MONITORING AGENCY REPORT NUMBER

TP-411-7188

DE95000243

11. SUPPLEMENTARY NOTES

NREL Technical Monitor: R. Mitchell

12a. DISTRIBUTION/AVAILABILITY STATEMENT

12b. DISTRIBUTION CODE

UC-1280

13. ABSTRACT *(Maximum 200 words)*

This report describes work done in Phase II of a 3-year project to advance Energy Conversion Devices, Inc. (ECD), roll-to-roll, triple-junction photovoltaic manufacturing technologies, to reduce the module production costs, to increase the stabilized module performance, and to expand the commercial capacity utilizing ECD technology. Major accomplishments in Phase II include: (1) designing, constructing and completing the initial optimization of a 200-kW multi-purpose continuous roll-to-roll amorphous silicon (a-Si) alloy solar cell deposition machine; (2) designing and constructing a serpentine deposition chamber that will be used to demonstrate a compact, low-cost deposition machine design with improved throughput and gas utilization factor; (3) demonstrating $\geq$ 8.3% initial small-area efficiency a-Si-alloy devices with an intrinsic a-Si layer deposited using serpentine technology in the initial start-up experiment; (4) developing a new back-reflector evaluation technique using Photothermal Defection Spectroscopy (PDS) to analyze the optical losses of textured back-reflector; (5) developing an improved textured Ag/ZnO back-reflector system demonstrating a 26% gain in short-circuit current density over the previous textured Al back-reflector system; (6) demonstrating the long-term stability of ECD's 0.3-m x 1.2 m (1 ft x 4 ft) production module; (7) developing a new grid/bus-bar design utilizing thin wire grids to improve the efficiency by approximately 3% to 4% and reduce the grid/bus-bar cost by about 50%; and (8) achieving a cumulative material cost reduction of 56%.

14. SUBJECT TERMS

amorphous silicon ; manufacturing ; photovoltaics ; solar cells

15. NUMBER OF PAGES
92

16. PRICE CODE

17. SECURITY CLASSIFICATION OF REPORT	18. SECURITY CLASSIFICATION OF THIS PAGE	19. SECURITY CLASSIFICATION OF ABSTRACT	20. LIMITATION OF ABSTRACT
Unclassified	Unclassified	Unclassified	UL